UNIVERSIDADE FEDERAL DE SANTA CATARINA
PROGRAMA DE PÓS-GRADUAÇÃO EM
ENGENHARIA MECÂNICA

CONDUTÂNCIA TÉRMICA DE CONTATO A BAIXAS PRESSÕES DE INTERFACE

Tese submetida à

UNIVERSIDADE FEDERAL DE SANTA CATARINA

para a obtenção do grau de

DOUTOR EM ENGENHARIA MECÂNICA

FERNANDO HENRIQUE MILANEZ

Florianópolis, Março de 2003

UNIVERSIDADE FEDERAL DE SANTA CATARINA
PROGRAMA DE PÓS-GRADUAÇÃO EM ENGENHARIA MECÂNICA

CONDUTÂNCIA TÉRMICA DE CONTATO A BAIXAS PRESSÕES DE INTERFACE

FERNANDO HENRIQUE MILANEZ

Esta tese foi julgada adequada para a obtenção do título de

DOUTOR EM ENGENHARIA

ESPECIALIDADE ENGENHARIA MECÂNICA

sendo aprovada em sua forma final.

_____
Marcia B. H. Mantelli - Orientadora

_____
M. Michael Yovanovich – Co-Orientador

_____
José Antonio Bellini da Cunha Neto - Coordenador do Curso

BANCA EXAMINADORA

_____
Júlio C. Passos

_____
Clóvis R. Maliska

_____
Jay M. Ochterbeck

_____
Humberto P. Cardoso

_____
Edson L. Zaparoli

"Em relação a todos os atos de iniciativa e de criação existe uma verdade fundamental cujo desconhecimento mata inúmeras idéias e planos esplêndidos: a de que no momento em que nos comprometemos definitivamente, a providência move-se também. Toda uma corrente de acontecimentos brota da decisão, fazendo surgir a nosso favor toda a sorte de incidentes e encontros e assistência material que nenhum homem sonharia que viesse em sua direção. O que quer que você possa fazer ou sonhe que possa, faça. Coragem contém genialidade, poder e magia. Comece agora."

Johann von Goethe

Dedico este trabalho a todos os que, de uma forma ou de outra,
contribuíram com a sua realização.

AGRADECIMENTOS

À minha Professora Orientadora no Brasil, Marcia Mantelli, por ter me aberto as portas, ao Prof. Julio Passos, por ter me ajudado com as bolsas de estudo e especialmente ao Prof. M. M. Yovanovich, por ter me aceito como um de seus alunos e ter me guiado ao longo deste projeto. Ao Prof. Rick Culham, por ter me dado pleno suporte durante minha estada na Universidade de Waterloo.

Ao Laboratório de Transferência de Calor em Microeletrônica–MHTL e à Universidade de Waterloo, por ceder completa infra-estrutura à realização deste projeto e à Universidade Federal de Santa Catarina e ao Núcleo de Controle Térmico de Satélites/Laboratório de Energia Solar -NCTS/LABSOLAR.

À CAPES ao CNPq por fornecerem bolsas de estudo durante estes quatro últimos anos e ao "Canadian Natural Sciences and Engineering Research Council," por financiar os estudos experimentais e teóricos desenvolvidos no MHTL.

A toda a minha família e amigos no Brasil por terem me dado total apoio quando decidi dar tão grande passo, que foi deixar tudo pra traz e ir em busca do desconhecido, e a todos os novos amigos que encontrei no Canadá, especialmente Pete, Allan, John e à comunidade brasileira de Waterloo–Braswat.

À minha querida Simone, pelo seu apoio incondicional, principalmente nos momentos cruciais que foram os meses finais de elaboração e apresentação desta tese.

E finalmente, mas não menos importante, a Deus.

RESUMO

Este trabalho analisa teórica e experimentalmente a condutância/resistência térmica de contato em baixas pressões de contato. Vários pesquisadores da área apresentam estudos comparativos entre os modelos existentes e dados experimentais nos quais os modelos subestimam os experimentos em baixas pressões de contado. Esses pesquisadores têm proposto explicações qualitativas para este inesperado fenômeno como sendo devido a dilatações térmicas diferenciais das amostras testadas, no entanto nenhum modelo capaz de prever quantitativamente o fenômeno foi proposto.

Neste trabalho, são apresentadas fortes evidências de que o inesperado fenômeno da condutância/resistência de contato a baixas pressões é devido ao truncamento das rugosidades que compõem as superfícies. Os modelos até então disponíveis assumem que as alturas das rugosidades das superfícies reais apresentam distribuição Gaussiana. Este trabalho propõe um novo modelo geométrico para a rugosidade da superfície, no qual a distribuição de alturas das rugosidades é na verdade Gaussiana Truncada. Segundo este modelo, as superfícies reais não apresentam rugosidades mais altas que um determinado valor, chamado de nível de truncamento da distribuição de alturas das rugosidades. Como decorrência de as rugosidades mais altas serem mais curtas que o previsto pela teoria atual, os modelos teóricos disponíveis subestimam a condutância térmica de contato a baixas pressões de contato.

O novo modelo teórico de condutância térmica de contato desenvolvido neste trabalho é então comparado com dados experimentais coletados por outro pesquisador da área, bem como com novos dados experimentais coletados durante este estudo. A comparação entre o novo modelo, chamado Gaussiano Truncado e os dados experimentais é muito boa, com o novo modelo prevendo a condutância de contato muito bem em toda faixa de teste da pressão de contato. O modelo Gaussiano Truncado de condutância térmica de contato necessita de um parâmetro a mais de rugosidade que os outros modelos até então existentes, que é o nível de truncamento da distribuição de alturas. Infelizmente, os atuais padrões e equipamentos disponíveis para medição de rugosidade superficial não são capazes de medir este novo parâmetro com a precisão necessária. A maneira mais rápida e precisa de se obter informação a respeito deste novo aspecto da geometria superficial é por meio de experimentos de condutância térmica de contato em baixas pressões de contato. Neste trabalho, amostras de Aço Inox AISI 304 e Níquel 200 com superfícies planas e jateadas por esferas de vidro e com três níveis de rugosidade para cada metal foram testadas. Os níveis de truncamento para superfícies com essas características são medidos e apresentados. Os resultados mostram que o nível de truncamento em geral diminuiu com o aumento da rugosidade das amostras, e que o Ni 200 apresenta níveis de truncamento maiores que o Aço Inox AISI 304.

THERMAL CONTACT CONDUCTANCE AT LOW CONTACT PRESSURES

Concerning all acts of initiative and creation, there is one elementary truth the ignorance of which kills countless ideas and splendid plans: that the moment one definitely commits oneself, then providence moves too. All sorts of things occur to help one that would never otherwise have occurred. A whole stream of events issues from the decision, raising in one's favor all manner of unforeseen incidents, meetings and material assistance which no man could have dreamed would have come his way. Whatever you can do or dream you can, begin it. Boldness has genius, power and magic in it. Begin it now.

Johann von Goethe

I dedicate this work to everyone who, by any means, has contributed to it.

ACKNOWLEDGEMENTS

To my supervisor in Brazil, Prof. Marcia Mantelli for opening the doors, to Prof. Julio Passos for helping with the necessary scholarship arrangements, and specially to Prof. M. M. Yovanovich for accepting me as one of his students and guiding me throughout this project. To Prof. Rick Culham, for giving me full support during my stay at the University of Waterloo.

To the Microelectronic Heat Transfer Laboratory-MHTL and to the University of Waterloo, for providing the necessary infra-structure and to the Federal University of Santa Catarina and the Satellite Thermal Control Laboratory/Solar Energy Laboratory-NCTS/LABSOLAR.

To the CNPq and the CAPES agencies, for providing me with scholarships during the last four years and to the Canadian Natural Sciences and Engineering Research Council of Canada, for funding the experimental and theoretical studies conducted at the MHTL.

To all my family and friends in Brazil for giving me support when I decided to take such a huge step, which was to leave everything behind me and go after the unknown, and to all the new friends I found in Canada, especially Pete, Allan, John and the Brazilian community of Waterloo.

To my dear Simone, for her endless support during the crucial final moments of writing and presenting this thesis.

And at last, but not least, to God.

CONTENTS

LIST OF FIGURES

LIST OF TABLES

NOMENCLATURE

Latin Alphabet:

A	contact area	[m^2]
a	mean contact spot radius, semi-major elliptic contact spot axis	[m]
b	semi-minor elliptic contact spot axis or elemental flux tube radius	[m]
C_c	dimensionless contact conductance	
c_1	Vickers micro-hardness correlation coefficient	[Pa]
c_2	Vickers micro-hardness correlation coefficient	
CMY	Cooper, Mikic and Yovanovich (1969)	
d	diagonal length	[m]
E	Young's modulus	[Pa]
E'	equivalent Young's modulus, (Eq. 2.39)	[Pa]
f	dimensionless truncation function (Eq. 3.23)	
f_{ep}	dimensionless elastoplastic function (Eq. 2.48)	
H	hardness	[Pa]
h	conductance	[W/m²·K]
k	thermal conductivity	[W/m·K]
k_s	$=2k_A k_B/(k_A+ k_B)$ harmonic mean thermal conductivity	[W/m·K]
M	measurement result (Eq. A2.1)	
m	mean absolute roughness profile slope	
m_0	variance of profile heights	[m^2]
m_2	variance of profile slopes	
m_4	variance of profile curvatures	[m^{-2}]
N	number of contact spots, number of surface heights measurements	
n	density of contact spots	[m^{-2}]
n	dimensionless blending parameter (Eq. 3.30)	
$\bar{n}'$	dimensionless variation of the number of contact spots with λ	
Nb	Niobium	
Ni	Nickel	
P	apparent contact pressure	[Pa]
Q	heat flow intensity	[W]
q	heat flux	[W/m^2]
R	thermal resistance	[W/K]

R_p	profile maximum height	[m]
S_f	elastoplastic parameter (Eq.2.54)	[Pa]
SS	Stainless Steel	
TG	Truncated Gaussian	
ν	$=m_{mn}/m_{mx}$, minimum to maximum mean absolute slope ratio	
X	dimensionless contact spot radii at the maximum contact pressure (Eq. 2.34)	
x	horizontal axis (abscissa)	
Y	mean plane separation	[m]
Y	yield stress	[Pa]
Z	profile height	[m]
Z	limit of X (Eq. 2.35)	
z	dimensionless profile height	
z_{trunc}	surface heights distribution truncation level	
Zr	Zirconium	
w	uncertainty	

Greek Symbols:

α	dimensionless $n \cdot a$ product (Eq. 2.28)	
α	surface bandwidth parameter (Eq. 5.1)	
β	mean asperity tip radius	[m]
Δ	sampling interval	[m]
ΔT	interface temperature drop	[K]
ε	constriction ratio	
ε_c	dimensionless elastoplastic strain	
γ	Mikic (1974) plasticity index (Eq. 2.44)	
Ψ	Greenwood and Williamson (1966) plasticity index (Eq. 2.43)	
ψ	constriction resistance parameter	
Φ	profile height probability density function	[m^{-1}]
ϕ	dimensionless profile height probability density function	
λ	$=Y/\sigma$, normalized mean plane separation	
υ	Poisson's ratio	
ρ	asperity tip radius	[m]
$\overline{\rho}$	dimensionless asperity tip radius	
σ	surface RMS roughness	[m]

Subscripts:

A,B	contacting bodies
a	apparent
c	contact
e	elastic
ep	elastoplastic
eq	equivalent
g	gap
i	summation index
j	joint
mn	minimum
mx	maximum
max	maximum
p	plastic
r	real or radiation
s	harmonic mean
TG	Truncated Gaussian
trunc	truncation level
v	Vickers hardness tests
0	reference

Superscripts:

TG	Truncated Gaussian

ABSTRACT

This work presents theoretical and experimental studies on thermal contact conductance/resistance at low contact pressures. Despite being generally accurate at relatively high contact pressures, the available theoretical models are not accurate when the contact pressure is low. Several researchers of the field have been presenting comparative studies between the available models and experimental data and have shown that the models underpredict experiments at low contact pressure. These researchers have been proposed qualitative explanations for this unexpected phenomenon as due to differential thermal expansion of the test samples. However, no models have being proposed to predict this effect.

In this work, strong evidences are presented that this odd phenomenon of contact conductance is due to truncation of the surface asperities. The models so far available assume that the distribution of surface asperities heights present is Gaussian. This work employs a new surface geometrical model, which asperity height distribution is in fact Truncated Gaussian. According to this model, actual surfaces do not present asperities higher than the surface height distribution truncation level. As a consequence, the higher asperities can be shorter than predicted by the existing theory and the available models under predict thermal contact conductance at low contact pressures.

The new theoretical thermal contact conductance model, denominated Truncated Gaussian-TG, is then compared against experimental data collected by another researcher, as well as the new data collected during the experimental part of this study. The comparison between the new model and the data is very good, with the new model predicting thermal contact conductance very well over the entire range of contact pressures tested. The TG model needs an extra roughness parameter, which is the truncation level of the surface height distribution. Unfortunately, the existing standards and equipments for roughness measurements are not capable of measuring this new parameter with the necessary accuracy. The fastest and most accurate way of extracting information regarding to this new aspect of surface geometry is by means of thermal contact conductance tests at low contact pressures. In this work, bead blasted SS 304 and Ni 200 samples possessing three roughness levels each were tested. In general, the truncation level was found to decrease with increasing surface roughness.

CHAPTER 1
INTRODUCTION

1.1. Introduction

Thermal contact conductance/resistance has many applications in engineering, such as spacecraft thermal control, ball bearing, nuclear fuel and microelectronic cooling. In these applications, conduction heat transfer plays a major role in removing heat dissipated by components that have narrow operational temperature ranges. The thermal path between heat source and heat sink includes interfaces between contacting solids. The resistance at these interfaces may increase considerably the total resistance of the thermal path and, consequently, increase the risk of failure of the components. Therefore, it is crucial to characterize the thermal resistance at the interface between contacting solids.

Thermal contact conductance/resistance has been extensively studied over the last six decades. Several theoretical and experimental studies are available in the open literature. Analytical models and empirical correlations have been proposed and compared with experimental data by several researchers. Good agreement has been reported in some cases. However, the available models are generally accurate for a relatively few types of contacts. Under certain circumstances, the theory does not predict the experiments well. For example, at low contact pressures the available models have been shown to systematically underpredict experimental data. The present work addresses this issue through the analytical and experimental study of thermal contact conductance at low contact pressures.

1.2. Bi-metallic heat switch – Motivation

The Satellite Thermal Control Group-NCTS of the Federal University of Santa Catarina has been working on the development of thermal control devices for spacecraft applications. Milanez and Mantelli (1999) proposed a bi-metallic heat switch for application on cryogenic systems of satellites. The bi-metallic heat switch has been initially developed to attach infrared radiation sensors to the satellite structure. However, other applications are possible.

In order to be effective, infrared radiation sensors must operate at cryogenic temperature levels. They are attached to the satellite structure, which may reach much higher

temperatures. The role of the heat switch is not only to provide mechanical strength during the launching of the satellite but also to minimize the heat transfer between the satellite and the sensor. A schematic drawing of the heat switch is shown in Fig. 1.1. It consists of two nuts, a threaded shaft and a disk. The disk has a shape similar to a thick washer and is placed between the nuts. The shaft and the disk are made of a low and a high thermal expansion coefficient materials, respectively. One nut is fixed to the satellite structure and the other to the cryogenic sensor. During the heat switch assembly, at room temperature, a controlled torque is applied to the shaft. The torque ensures a rigid mechanical coupling between the sensor and the satellite structure, which is necessary during the launching of the satellite (Fig. 1.a). When the satellite achieves its final orbit, the temperature of the sensor drops to cryogenic levels. During the cooling of the sensor, the differential contraction between the shaft and the disk makes the contact pressure between the nuts and the disk to decrease. As a consequence, the thermal contact resistances at the disk/nuts interfaces increase, increasing the overall heat switch thermal resistance. As the contact pressure goes to zero, the total thermal resistance of the heat switch reaches its maximum value. In this situation, the heat switch is decoupled (Fig. 1.b), minimizing the heat load coming from the satellite structure to the cryogenic system.

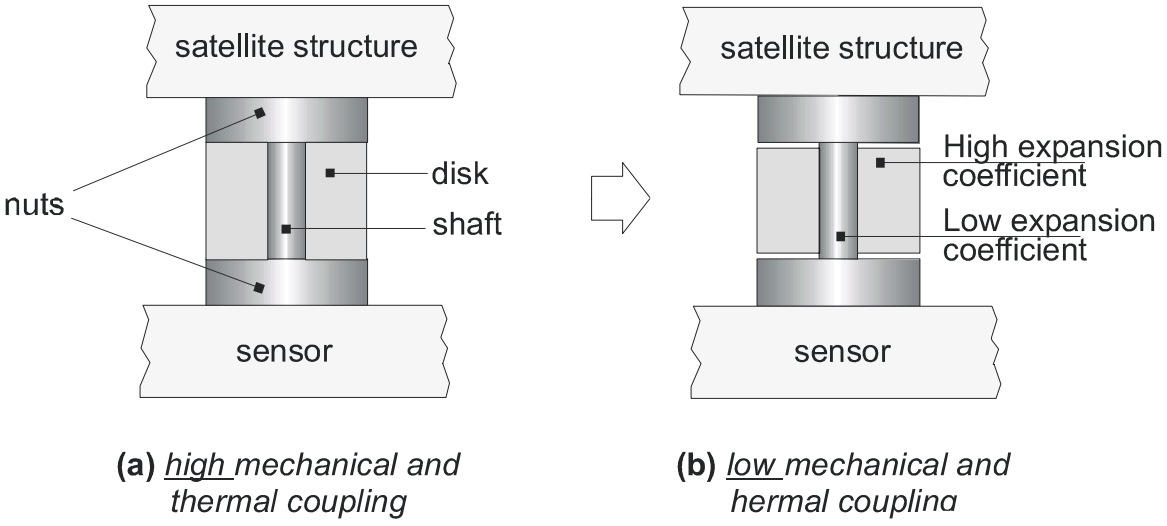

Figure 1.1 – Working principle of the heat switch developed at NCTS

The total thermal resistance of the heat switch is a function of temperature. If the thermal expansion coefficient of the disk is larger than that of the shaft, the thermal resistance increases with decreasing temperature. Otherwise, the thermal resistance decreases with temperature. The heat switch could also be used in other applications, such as to couple radiation sensors to cryogenic refrigerators. In this application, when the radiation sensor is operating, it is necessary a low thermal resistance between the sensor and the refrigerator in order to keep the sensor temperature as low as possible. In this situation, the heat switch provides a good thermal coupling between the radiation sensor and the cryogenic refrigerator. However, sometimes it is convenient to disconnect the sensor from the refrigerator, as for example in redundant refrigeration systems, in order to avoid parasitic heat loads from refrigerators turned off. Under these circumstances, the heat switch must provide high thermal resistance between the sensor and the deactivated refrigerator. In this application, the material of the shaft must possess a higher thermal expansion coefficient than the material of the disk. Other heat switch conceptions were presented in the literature for this type of application (Frank and Nast, 1985, Nast et al., 1982, Naes and Nast, 1985 and Van Oost et al., 1991). Other heat switch applications include thermal management of electronic boxes in spacecrafts. Lankford (2002) presents an extensive review on the state of the art of heat switch technology applied to spacecraft thermal control.

Milanez and Mantelli (2000 and 2001) presented theoretical models to predict the thermal resistance of the heat switch as a function of temperature. They also performed a non-dimensional parametric study of the influence of the parameters that affect the thermal resistance of the heat switch and compared the models with experimental data collected from a prototype of the heat switch. The comparison between theory and experiments was good. The maximum difference between the theory and the experimental data was 64% and the minimum difference was only 0.3%. During the development of the theoretical models, the authors noticed that several works reported an unusual behavior of thermal contact conductance at low contact pressures. Near the decoupling temperature, the heat switch operates in the low contact pressure range. Despite being sufficiently accurate in predicting thermal contact conductance at high contact pressures, the available models fail to predict accurately experimental data at low contact pressures. Several explanations have been proposed to describe this unexpected behavior at low contact pressures, but no analytical models have been proposed.

The work proposed here is the analysis of thermal contact conductance at low contact pressures. As it will be discussed along this work, this study analyzes one of the very basic

assumptions of the existing theory on thermal contact conductance, which is the Gaussian distribution of surface heights. The hypothesis that surface heights present Gaussian distributions has been adopted by hundreds of works in the field. Strong evidences are shown here that the assumption of fully Gaussian distribution is not adequate when the nominal contact pressure is relatively low (generally bellow 1 MPa). It will be shown that the actual distribution of surface heights has the tails shortened and that it affects thermal contact conductance at low contact pressures.

This is primarily a fundamental study in the thermal contact conductance field. It has applications in the bi-metallic heat switch mentioned above, however, other applications are possible. As an example, some microelectronic components that need to be cooled, are attached to the heat sink by means of clamping devices, so that the contact pressure lie in the low contact pressure range. As another example, in nuclear energy, it is useful to know for safety reasons the behavior of thermal contact resistance between the nuclear fuel rod and the nuclear rod sheath when the contact pressure between the two drops bellow expected.

1.3. Objectives of the present work

The main objective of this work is to study the thermal contact conductance at low contact pressures. In order to accomplish this task, the following specific topics were addressed:

- Review the existing theory on thermal contact conductance,
- Identify the weakness of the existing models at low contact pressures and propose new thermal contact conductance models
- Compare the new models and the existing models with existing experimental data,
- Collect new thermal contact conductance experimental data at low contact pressures for distinct metals, for different roughness levels and for two loading/unloading cycles of contact pressure,
- Compare the collected experimental data with the new and the existing models,
- Analyze the truncation level of actual bead blasted surfaces,
- Analyze the deformation mode of the surfaces tested by inspecting the hysteresis effect of thermal contact conductance.

In Chapter 2, the existing theory on thermal contact conductance, with the models based on the pioneer work of Cooper, Mikic and Yovanovich (1969) are reviewed in more

details. In Chapter 3, an analysis of the reasons why these models fail to predict thermal contact conductance at low contact pressures is presented and new models are proposed. Also in Chapter 3, these new models, as well as the existing theoretical models are compared with experimental data collected from other researchers in order to illustrate the effect of surface height truncation on thermal contact conductance at low contact pressures. In Chapter 4, the experimental set-up and the procedure employed to obtain thermal contact conductance data at low contact pressures are described. In Chapter 5, the obtained data is compared with the new and the existing models. In Chapter 6, the summary of this work and the conclusions drawn from this study are presented.

CHAPTER 2
LITERATURE REVIEW

2.1. Introduction

In this chapter, some aspects of the existing theoretical and experimental studies on thermal contact conductance/resistance are reviewed. The chapter starts with the definitions and nomenclature commonly encountered in the thermal contact conductance/resistance field. The pioneer work of Cooper, Mikic and Yovanovich-CMY (1969), which constitutes the basis of several models encountered in the literature as well as the new model which will be proposed here, is then presented. Special attention is given to the CMY model because it has been proven to be one of the most accurate and easiest to manipulate models available. After that, the other models available in the literature that are based on the CMY model are presented. Finally, available correlations of the CMY based models are presented.

2.2. Thermal joint conductance/resistance – Definitions

There is a large number of reviews on thermal joint conductance/resistance available in the literature (Mantelli and Yovanovich, 2002, Lambert and Fletcher, 1997b, among many others). The review made here is directed towards the important aspects from the point of view of development of the new model, presented in the next chapter. In this section, an assessment of the definitions and nomenclature generally used in the literature is presented, although not all researchers adopt exactly the same definitions and nomenclature. For example, the definition of “joint conductance” adopted here is equivalent to the definition of “contact conductance” adopted in other works. In this work, the name “contact conductance” is referred to a specific heat transfer mode that constitute the “joint conductance”, which is also composed by two other heat transfer modes, as it will be seen.

Real surfaces obtained by actual machining processes present deviations from their idealized geometry. When real surfaces are analyzed in a microscopic scale, roughness and waviness can be observed. When two bodies are put into contact, they will touch each other only at their highest asperities. Under contact load, these asperities deform originating small contact spots. The real contact area, associated with the contact spots, is only a very small fraction of the total apparent or nominal contact area (generally less than 1%). In the remaining portion of the apparent contact area, the two surfaces are separated by a small gap. Heat transfer through the interface between two solids can take place by three different

mechanisms: conduction through the contact spots, radiation through the gap between the solids and conduction through the fluid that fills the gap, if there is any. The conduction through the contact spots is generally much more effective than the radiation and the conduction through the fluid filling the gap, especially for metals, because of the higher thermal conductivity of the solids in comparison to fluids and gases. As a consequence, the heat flow through a real interface will constrict towards the contact spots and then spread as it crosses the interface. The constriction and spreading of heat flow originate the called *contact resistance*. Along with the contact resistance, the resistances associated to the radiation and to the conduction through the fluid filling the gap constitute the called *joint resistance*. The joint resistance can be observed macroscopically as a temperature drop across the interface ΔT [K] by extrapolating the temperature distributions of the two contacting solids (Fig. 2.1). The thermal joint resistance R_j [K/W] is then defined as the ratio of the temperature drop across the interface by the heat flowing through the interface Q [W]:

$$R_j = \frac{\Delta T}{Q} \tag{2.1}$$

The thermal joint conductance h_j [W/m^{2}K] is then defined as the inverse of the joint resistance per unit apparent contact area A_a [m^2]:

$$h_j = \frac{1}{R_j \, A_a} \tag{2.2}$$

Although the three heat transfer mechanisms interact with each other, modeling the three at the same time is very difficult. The three mechanisms are commonly analyzed separately from each other, and the thermal *conductance of the joint* is treated as the summation of the three conductances: contact h_c, radiation h_r and gap h_g:

$$h_j = h_c + h_r + h_g \tag{2.3}$$

2.3. Types of joints

As mentioned before, real surfaces present roughness and waviness. Roughness is a small scale or microscopic irregularity, while waviness is an irregularity of larger dimensions. In actual applications, it may be difficult to separate these two types of irregularity. Real surfaces present a continuous superposition of irregularities of different scales. The issue of separating waviness from roughness will be discussed in more details in the section that deals with surface geometry characterization (section 4.7). By now, it is assumed that the irregularities of real surfaces can be separated into these two types of irregularities. As a result, there are three possible combinations of contact:

- *1st.type:* Contact between *conforming rough surfaces*, when the surfaces are nominally flat and rough,
- *2nd.type:* Contact between *non-conforming smooth surfaces*, when the surfaces present waviness but are relatively smooth,
- *3rd.type:* Contact between *non-conforming rough surfaces*, when the surfaces are wavy and rough.

The first case occurs when the dimensions of the asperities that constitute the roughness are much larger than the amplitude of the waviness. That does not mean that the surfaces have to be perfectly flat. A small flatness deviation can be corrected by elastic deformation when the surfaces are pressed against each other. In this type of joint, the contact spots are randomly spread over the apparent contact area. Most of the work on contact conductance is on this type of joint, with several models available in the literature that predict experimental data extremely well for a relatively wide range of metals and surface characteristics. The second type of joint appears when the dimensions of the asperities are much smaller than the amplitude of the waviness. In this case the effect of the roughness can be ignored and the dimensions of the contact are dictated by the macroscopic dimensions of the contacting solids. There are only a few special cases of the contact between non-conforming smooth surfaces that can be modeled, which are the contact between ellipsoids undergoing elastic deformation in contact. The Hertz elastic theory has been successfully employed in this case (Clausing and Chao, 1965, McGee, Schankula and Yovanovich, 1985, among many others). The third type of joints, non-conforming rough surfaces, is the combination of the two previous types. In this case, the contact spots are concentrated in a region, called “contour area”, smaller than the apparent contact area. It is very difficult to model the contact between non-conforming rough surfaces. Various attempts have been made for the special case of the contact between rough ellipsoids. An extensive review of the existing work on this type of contact can be found in Lambert and Fletcher (1997b). The available models are very difficult to manipulate, being generally presented in graphical form or as a computational code. The accuracy is reasonably good in some cases but in general the models do not predict experiments well for a wide range of contact pressures, material properties and geometry. The main difficulty of the problem is to predict the size of the contour area. An accurate closed form model to predict contact conductance between non-conforming rough surfaces is still very much needed.

Ordinary surfaces, encountered in practical applications, generally do not present the necessary features in order for the first type of contact to occur. Ordinary surfaces will in most of the times present the features of the third type contact (non-conforming rough surfaces),

which are very difficult to deal with, as stressed in the last paragraph. If one tries to use the existing theory for conforming rough surface to predict the thermal contact conductance between ordinary surfaces, the error could be easily of one order of magnitude. In order to use the existing theory of conforming rough surfaces, the surfaces must be prepared with very special care, so the surface features are in accordance with the assumptions of the models. Unfortunately, it is not possible at this stage of development of the theory on thermal contact conductance to predict accurately the thermal contact conductance between surfaces that were not prepared according to the assumptions of the model. This work is focused on the first type of joint: contact between conforming rough surfaces. This sort of surfaces can be achieved in practical applications if the surfaces are prepared with special care, especially to warrant that the surfaces are nominally flat (combined flatness deviation less than 1 μm, approximately). During the presentation of the experimental part of this study, the usual preparation method employed to obtain conforming rough surfaces will be described in details. The remaining of this literature review will be focused on the contact between conforming rough surfaces. The reader interested in more details about the two other types of joints is suggested to consult the works mentioned in the previous paragraph or the many other works available on this subject.

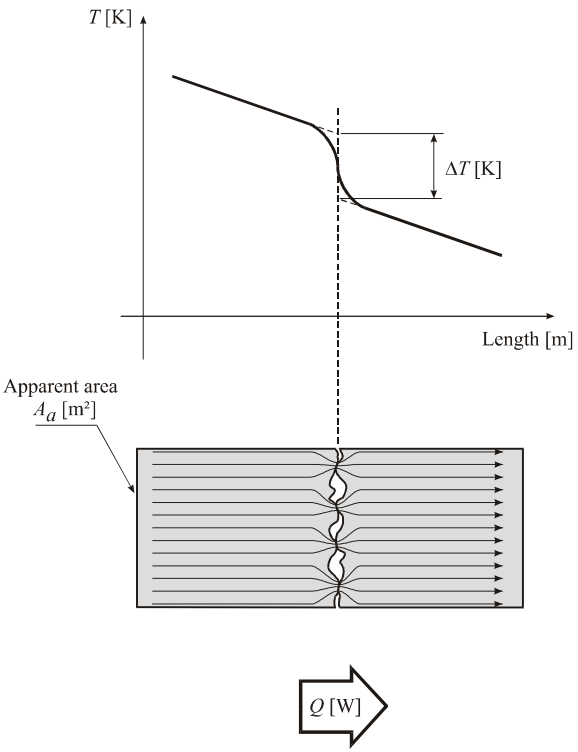

Figure 2.1 – Temperature drop and heat flow constriction across an interface

2.4. Contact between conforming rough surfaces

There are numerous theoretical models available in the literature to predict the three heat transfer mechanisms between conforming rough surfaces. Since the gap and contact conductance are generally more important, they have received more attention. The radiation conductance is effective only in applications at high temperatures. Mc Waid (1990) describes the model generally employed to estimate the radiation conductance: two parallel, gray plates, separated by a small distance so the shape factor is approximately 1. Assuming that the emissivities of the two surfaces is 0.2 (typical values), the author shows that unless the mean temperature of the contact is quite high, the radiation conductance is negligible. This work is focused in applications at room temperature, such as microelectronic cooling and spacecraft thermal control. The experimental portion of this work is also restricted to approximately ambient temperatures. Therefore, contact radiation heat transfer is neglected in this work.

The gap conductance has been modeled in different ways. Song et al. (1993) made a review of most of the gap models available in the literature. The first attempts consisted of modeling the gap conductance as the ratio between the conductivity of the fluid/gas and the mean separation between the surfaces. The mean separation was computed as the sum of the R_a roughness (or center line average - CLA) of the two contacting surfaces. The main weakness of this model is the inability to take into account for the contact pressure, which affects the magnitude of the mean separation gap. This model is also inappropriate for gaps filled with gas due to the rarefaction effect resulting from the small separation between the surfaces. The models that were presented later on proposed the idea of introducing an extra distance, called the gas parameter M, in series with the mean separation gap to take into account for the rarefaction of the gas. The gas parameter M, is a function of the gas pressure and temperature, thermal accommodation coefficient and type of gas. Yovanovich et al. (1982) proposed a statistical gap model, called YIGC, which takes into account for the variation of separation gap along the interface and for the gas rarefaction effect. In this model, the mean separation is computed using an expression first presented by Mikic (1971), which comes from the work of Cooper et al. (1969) and takes into account for the magnitude of the contact pressure. Song et al. (1992) compared their own experimental data with the YIGC and three other models proposed by other researchers and showed that the YIGC model was in better agreement with the experiments. Song et al. (1993) concluded that, at low contact pressures, the expression proposed by Yovanovich et al. (1982) to predict the mean separation gap was not accurate and proposed the use of the height of the highest asperity as a measure of the mean separation gap instead.

If the gap is filled with grease, the models mentioned above are not valid because they were developed primarily for gases. Savija et al. (2002b) proposed a simple model to predict the gap resistance of joints filled with grease: the gap resistance is modeled as the ratio between the mean separation and the conductivity of the grease. The mean separation is computed according to the plastic deformation model of Cooper et al. (1969). The authors compared their model with limited experimental data available in the literature and concluded that the model had a nominal agreement with experimental data, i. e., the model predicts well the trend of joint resistance versus the ratio between the RMS roughness and the conductivity of the grease. According to Savija et al. (2002), other works in this field are restricted to experimental studies. The effect of oil and gas in sphere/flat contact conductance was studied by Yovanovich and Kitscha (1973) for ball bearing applications.

There is still another sub-class of contact between conforming rough surfaces, which is the contact between coated surfaces. Fletcher et al. (1998) present a study of applicability of coatings on contacting surfaces of microelectronic components in order to enhance thermal conductance to avoid failure of these components due to increasing power densities and heat generation of actual electronic systems. They analyzed metallic coatings, such as vapor-deposited aluminum, magnesium, lead and indium, and non-metallic coatings, such as oxide/anodic films, ceramics, and other materials. Marotta and Fletcher (1996) measured thermal contact conductance of aluminum and cooper coated with several refractory ceramic coatings and compared the data with models available in the literature and showed that the available models fail to predict accurately the experiments. The model of Antonetti and Yovanovich (1988) was shown to be the best available because it predicts the trend of contact conductance versus pressure reasonably well, despite the model had been developed for metallic coatings. Savija et al. (2002a) review the existing work on the called thermal interface materials such as metallic foils, polymeric compliant material and coatings.

In this work, only the conductance associated to the conduction through the contact spots of uncoated joints is considered, that is, only contact conductance is considered. As it will be seen later on, the experimental investigation was designed so that radiation and gap conductances can be neglected.

2.5. Contact conductance between uncoated conforming rough surfaces

Most of the thermal contact conductance models available in the literature are composed by three sub-models: thermal, mechanical and geometry models. The thermal model deals with the heat conduction problem; it predicts the thermal contact conductance for

a given set of contact parameters. The contact parameters are: size and shape of the contact spots, and density of contact spots per unit apparent contact area. The contact parameters are obtained by means of a mechanical deformation model for the contacting asperities. In order to estimate the contact parameters, the mechanical model needs the shape and the dimensions of the asperities that constitute the surfaces. Since it is impossible to characterize the geometry of all asperities that constitute a real surface in a deterministic way, statistical models have been employed. These three sub-models are described in more details in the following sub-sections, which are basically a review of the work of Cooper, Mikic and Yovanovich – CMY (1969) and other models that were developed based on the CMY model. The choice for this particular work is not purely arbitrary. The CMY based models have been shown by various researchers to be very accurate and easy to manipulate. The CMY models have been successfully adapted to problems different from the original work, as it will be seen. The new model that will be presented in this work (Chapter 3) is also an adaptation of the CMY model, which was modified in order to deal with the problem of low contact pressures.

2.5.1. Thermal model

Two contacting bodies pressed one against the other have the higher asperities deformed, originating contact spots. The shape and distribution of the contact spots depends on the preparation method of the surfaces. If the machining process originates anisotropic surfaces, i. e., surfaces presenting patterns or lays in determined directions, such as grinding and turning, for example, the contact spots are approximate ellipses (grinding) or stripes (turning). When the surface preparation method originates isotropic surfaces, i. e., surfaces that do no present any pattern in some preferential direction, such as bead blasting and mechanical lapping, for example, the contact spots are approximately circular. The contact spots may be randomly distributed (bead blasting, lapping, grinding) or evenly spaced (turning) over the apparent contact area, provided the surfaces are nominally flat. In the present work, the case of randomly distributed contact spots is analyzed. In order to simplify the presentation of the models, the surfaces are assumed to be isotropic, but the same procedure described here can also be employed for anisotropic surfaces, such as those obtained by grinding.

The thermal model normally employed for isotropic surfaces is sketched in Fig. 2.2. As mentioned, circular contact spots of different sizes are randomly spread over the apparent contact area. Surrounding every contact spot (radius a_i) there is an elemental heat flux tube

(radius b_i). Heat flowing inside the elemental flux tube must constrict towards the contact spot and then spread as it crosses the interface. The resistance associated to the constriction and subsequent spreading of heat flow is called micro-constriction resistance. The summation in parallel of the micro-constrictions all N elemental flux tube resistances $R_{c,i}$ constitute the contact resistance R_c:

$$\frac{1}{R_c} = \sum_{i=1}^{N} \frac{1}{R_{c,i}} \tag{2.4}$$

The constriction resistance to heat flow in a circular tube is given by two parts:

$$R_{c,i} = \frac{\psi(\varepsilon_i)}{4\, k_A\, a_i} + \frac{\psi(\varepsilon_i)}{4\, k_B\, a_i} \tag{2.5}$$

where $\varepsilon_i = a_i / b_i$ is the constriction ratio, $\psi(\varepsilon_i)$ is the constriction resistance parameter and k [W/mK] is the thermal conductivity. The first term in the summation above is the constriction resistance in the "hot" body (A) and the second term is the spreading resistance in the "cold" body (B). As one can see, the constriction parameter $\psi(\varepsilon_i)$ is the same for both the constriction and the spreading resistance, because of the symmetry about the contact plane.

Substituting Eq. (2.5) into Eq. (2.4) and substituting the resulting expression into the definition of contact conductance (Eq. 2.2) one obtains:

$$h_c = 2 \frac{k_s}{A_a} \sum_{i=1}^{N} \frac{a_i}{\psi(\varepsilon_i)} \tag{2.6}$$

where $k_s = 2\, k_A\, k_B / (k_A + k_B)$ is the harmonic mean thermal conductivity. In order to simplify the analysis, the contact spot radii a_i are substituted by their root mean square (RMS) value (Cooper et al., 1969), i. e., $a_i = a$ = RMS(a_i). The constriction factors are also substituted by their mean value ($\varepsilon_i = \varepsilon$). With these simplifications, Eq. (2.6) can be re-written in the following form:

$$h_c = 2 \frac{k_s}{A_a} \frac{N\, a}{\psi(\varepsilon)} = 2\, k_s \frac{n\, a}{\psi(\varepsilon)} \tag{2.7}$$

where $n = N / A_a$ is the density of contact spots per unit apparent contact area. From these simplifications, and knowing that the summation of the areas of all contact spots and the summation of the areas of all elemental flux tubes must be equal to the total real contact area and the total apparent contact, respectively, one obtains a relation for the constriction factor:

$$\varepsilon \equiv \frac{a}{b} = \sqrt{\frac{A_r}{A_a}} \tag{2.8}$$

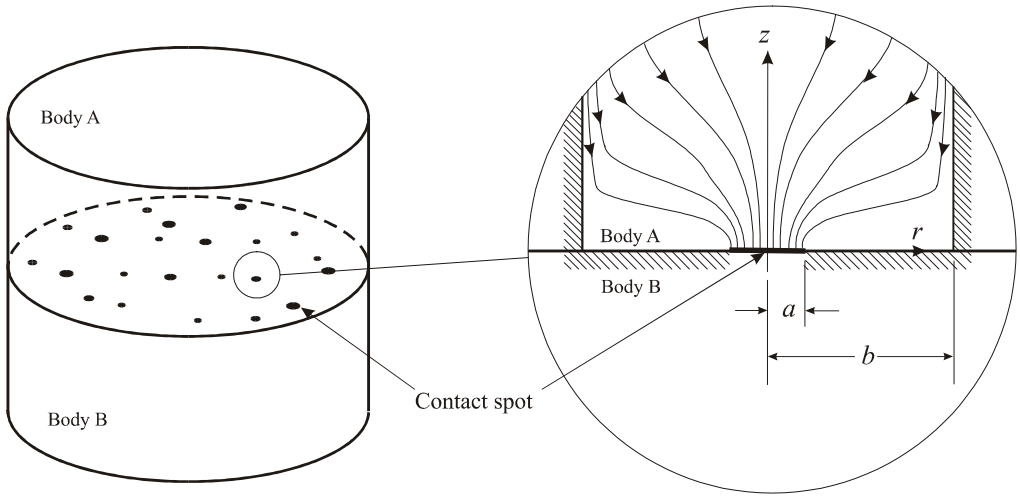

a) contact spots b) elemental flux tube

Figure 2.2 – Thermal model

The expression for the constriction resistance parameter $\psi(\varepsilon)$ was obtained by solving the governing equation for steady state heat conduction with no internal generation (Laplace's Equation) inside the elemental heat flux tube. The contact spot centre and the elemental heat flux tube axis are aligned (Fig. 2.2.b). The dimensions of elemental heat flux tube determine the region of influence of the contact spot; the walls of the elemental flux tube are adiabatic. Far from the interface ($z \rightarrow \infty$), the heat flow lines are parallel, i. e., the heat flux is uniform. In practical applications, however, for $z > 1$ mm the heat flow lines are out of the influence of the contact spot. That means the micro-constriction of heat flow takes place only very close to the interface (less than 1 mm). Whatever happens with the heat flow lines for $z > 1$mm is not important from a contact resistance point of view, even if the heat is entering Body A (of Fig. 2.2) from the lateral walls in the "r" direction, for example. In this case, one should first solve the heat conduction problem (heat entering Body A from the lateral walls and leaving the body through the bottom surface at z=0) and then solve the contact resistance problem. As heat approaches the interface, it must constrict towards the contact spot. At the interface ($z = 0$), the tube is adiabatic outside the contact spot ($a < r < b$) and isothermal inside the contact spots ($r < a$). Therefore, boundary conditions are mixed at $z = 0$. To overcome this problem, the isothermal boundary condition at $r < a$ was substituted by a flux distribution proportional to $[1-(r/a)^2]^{-1/2}$, which generates a nearly uniform temperature distribution at $z = 0$ and $0 \leq r \leq a$. The total resistance of the heat flux tube was then found by solving the

governing equation for the temperature field inside the elemental heat flux tube with this equivalent heat flux distribution inside the contact spot. The constriction parameter was then obtained as an infinite series. Cooper et al. (1969) presented the following approximate relation for the constriction resistance parameter:

$$\psi(\varepsilon) = (1-\varepsilon)^{1.5} \tag{2.9}$$

Substituting Eqs. (2.9) and (2.8) into Eq. (2.7) one obtains the final expression for the thermal part of the thermal contact conductance model:

$$h_c = 2\, k_s \frac{n\, a}{\left(1-\sqrt{A_r/A_a}\right)^{1.5}} \tag{2.10}$$

The density of contact spots n [m^{-2}], the mean contact spot radius a [m] and the real to apparent contact are ratio A_r / A_a are the called contact parameters that must be obtained from the geometry and the mechanical deformation models.

De Vaal (1988) adapted the CMY isotropic plastic model to the contact of ground surfaces. As mentioned before, grinding generates anisotropic surfaces. The mean absolute surface slope (m) of ground surfaces depends on the direction that the profile is taken, and the contacting spots are approximately elliptical instead of circular. De Vaal (1988) developed a new thermal model based on a rectangular elemental flux tube with an elliptical contact spot at the center. The thermal contact conductance of anisotropic surfaces is computed as:

$$h_c = \frac{k_s n \sqrt{\pi a b}}{2\,\psi(\nu,\varepsilon)} \tag{2.11}$$

where $\varepsilon=(A_r/A_a)^{1/2}$, $\nu=b/a$ and a [m] and b [m] are the major and minor semi-axis of the mean elliptical contact spot. De Vaal (1988) presents the expression for the constriction resistance parameter $\psi(\nu,\varepsilon)$.

2.5.2. Surface geometry model

It is well accepted that surfaces obtained by many usual machining processes present nearly Gaussian distribution of heights. Several researchers have shown actual surface height distribution measurements and comparison against the Gaussian distribution (Williamson, Pullen and Hunt, 1969, Greenwood and Williamson, 1969, Kimura, 1970, O'Callaghan and Probert, 1970, among many others). Figure 2.3 presents the distribution of heights from three profiles collected from one bead blasted surface of one of the SS 304 specimens used in this experimental work. The solid line is the Gaussian distribution. As one can see, the Gaussian model agrees very well with the measurements, at least in the range of surface heights between approximately -4.6 and 3.7 times the surface RMS roughness σ. Williamson, Pullen

and Hunt (1969) present a study of the types of the machining processes that produce Gaussian surfaces. According to the authors, cumulative processes, i.e., processes where the final surface topography is the result of the action of a large number of events, produce Gaussian surfaces. A typical example of a cumulative process is bead blasting, in which the surface is bombarded by millions of high speed glass beads. The Gaussian geometry generated is a consequence of the Central Limit Theorem, which roughly states that the distribution of the sum of a large number of independent random variables will be approximately normal. Machining processes involving removal of material like turning do not generally produce Gaussian surfaces. However, some machining processes like grinding and lapping, which involve material removal, may produce nearly Gaussian surfaces provided the surfaces are prepared with special care (De Vaal, 1988, Sayles and Thomas, 1976). The assumption of Gaussian distribution of surface heights is made in many of the available thermal contact conductance models, including the CMY based models described in the remaining of this chapter.

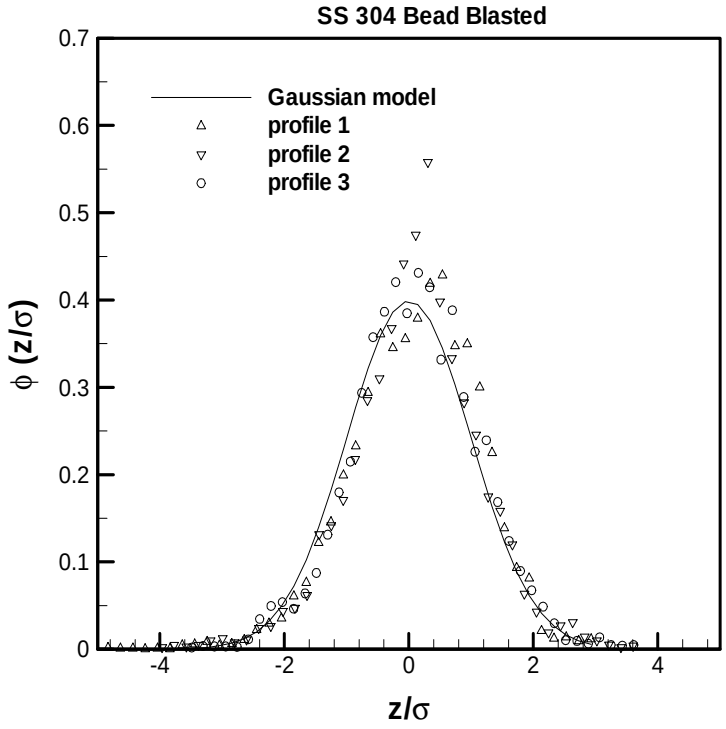

Figure 2.3 - Measured height distributions of a SS 304 bead blasted surface and comparison with the Gaussian model

The surface characterization is generally made by means of profiles measured with a stylus type profilometer (see Fig. 2.4). The equipment generally computes the first two power

spectral moments of the measured profile. The first moment m_0 [μm^2] is the variance of the profile heights, which is equal to the square of the RMS roughness σ [μm]:

$$m_0 = \frac{1}{L}\int_0^L Z^2 dx = \sigma^2 \tag{2.12}$$

The second profile power spectral moment m_2 [dimensionless] is the variance of the profile slope:

$$m_2 = \frac{1}{L}\int_0^L \left(\frac{\partial Z}{\partial x}\right)^2 dx \tag{2.13}$$

The mean absolute slope m is more used in thermal contact conductance model than the variance of the slope m_2. It is defined as:

$$m = \frac{1}{L}\int_0^L \left|\frac{\partial Z}{\partial x}\right| dx \tag{2.14}$$

For Gaussian surfaces, $m = \sqrt{\frac{2m_2}{\pi}}$. The third profile power spectral moment of interest is the variance of the profile curvature m_4 [m^{-2}]:

$$m_4 = \frac{1}{L}\int_0^L \left(\frac{\partial^2 Z}{\partial x^2}\right)^2 dx \tag{2.15}$$

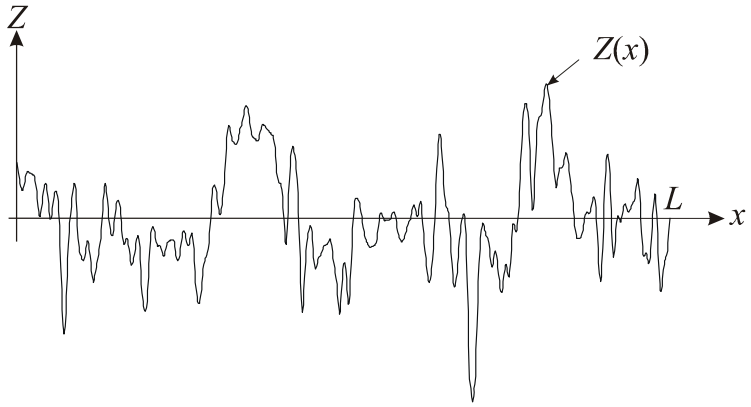

Figure 2.4 – Surface profile (vertical scale exaggerated)

As it will be seen later, the contact between two surfaces is more easily modeled when one of the surfaces is assumed perfectly smooth. The geometry of two rough Gaussian surfaces can be combined as a single equivalent rough surface in contact with a flat surface by means of the convolution theorem (De Vaal, 1999). The power spectral moments of the equivalent surface are computed as the summation of the respective moments of the two contacting surfaces:

$$(m_0)_{eq} = (m_0)_A + (m_0)_B \tag{2.16}$$

$$(m_2)_{eq} = (m_2)_A + (m_2)_B \tag{2.17}$$

$$(m_4)_{eq} = (m_4)_A + (m_4)_B \tag{2.18}$$

2.5.3. Mechanical models

There are basically three surface deformation models: elastic, plastic or elastoplastic. Under plastic deformation, the asperities are permanently deformed during loading and do not recover their original shape after the surfaces are pulled apart. Under elastic deformation, as the surfaces are pulled apart the asperities recover the original shape as before any loading had taken place. For the elastoplastic case, some intermediate behavior between fully plastic and fully elastic deformation takes place. The elastic deformation is reversible, and the elastic models predict exactly the same behavior for thermal contact conductance during both ascending and descending levels of contact pressure. On the other hand, the plastic models were developed for first loading only. For surfaces undergoing plastic deformation during first loading, when the contact pressure is released the contact spots are larger than during first loading for the same contact pressure, which makes contact conductance being larger during unloading than during loading. This phenomenon is known as hysteresis effect of contact conductance.

Cooper, Mikic and Yovanovich (1969) proposed a plastic deformation model for the contacting asperities in which the asperities of the harder of the two contacting surfaces penetrates the softer surface in a way similar to hardness indentation tests, like the Brinell test. In this test, a hard steel ball is pressed against the surface being tested, and the hardness of the surface is defined as the indentation load divided by the contact area between the indenter and the surface being tested. The indentation area is computed by measuring the diameter of the impression left by the indenter. Assuming that the shape of the asperities is approximately spherical near the tips, Cooper, Mikic and Yovanovich (1969) proposed the use of the hardness obtained from Brinell tests as a measure of the supporting contact pressure. By means of a simple force balance, they derived an expression for the real to apparent area ratio, appearing in Eq. (2.10):

$$A_r\, H = A_a\, P \quad \Rightarrow \quad \frac{A_r}{A_a} = \frac{P}{H} \tag{2.19}$$

where H [Pa] is the hardness, obtained from Brinell tests, and P [Pa] is the nominal or apparent contact pressure, defined as the contact load divided by the apparent contact area. Later on, Hegazy (1984) showed that the Brinell hardness is not a good measure of the plastic

contact pressure. It is well known that due to work-hardening during the machining process, the hardness of the surface is generally harder than the bulk of the material. Surface deformation due to the contact between solids is confined to regions very close to the surface (a few micrometers deep), while the Brinell test uses relatively high indentation loads, which makes the indenter penetrate very deep into the sample, where the material is softer than the surface. As a result, the Brinell test underpredicts the hardness of the surface by up to three times. Hegazy (1984) proposed the use of the Vickers micro-hardness as a measure of the plastic supporting pressure for contact mechanics applications. The Vickers micro-hardness test employs a diamond pyramid indenter, with indentation loads as low as 10 grams. The author proposed a procedure to estimate the surface micro-hardness which consisted of measuring the Vickers micro-hardness of the surface for several loads between 10 and 300 grams and then correlate the obtained hardness values H_v [MPa] to the respective diagonal of the square impression left by the indenter d_v [μm] in the following form:

$$H_v = c_1 \left(\frac{d_v}{d_0} \right)^{c_2} \tag{2.20}$$

where d_0 [μm] is a reference value, generally 1 μm for convenience, used to make the term between brackets dimensionless, and c_1 and c_2 are the called Vickers micro-hardness correlation coefficients. Since the diagonal of the indentation impression d_v is proportional to the penetration of the indenter, the c_1 and c_2 coefficients provide information of the hardness variation with depth into the surface. Song and Yovanovich (1988) developed a model to compute the plastic contact hardness H_c [Pa] as a function of the apparent contact pressure, surface roughness and the Vickers micro-hardness coefficients of the softer of the two contacting materials:

$$\frac{P}{H_c} = \left[\frac{P}{c_1 \left(1.62 \frac{\sigma}{m} \right)^{c_2}} \right]^{\frac{1}{1+0.071 c_2}} \tag{2.21}$$

The deformation model described above was developed assuming that the asperities of the rough surface indent the smooth surface. When the two contacting surfaces have similar hardness, mutual deformation takes place. When the hardness of the rough surface is smaller than the hardness of the flat surface, instead of asperities indenting the smooth surface, the soft asperities are flattened out by the hard smooth surface. Even when mutual deformation takes place or when the rough surface is softer than the smooth surface, the indentation tests are a good measure of plastic contact hardness, as demonstrated by Bowden and Tabor

(1964). These authors analyzed a series of indentation tests with conical indenters possessing different semi-angles being pressed against a smooth surface. They analyzed the effect of the relative hardness of the cone in comparison to the hardness of the surface. The results are shown in Fig. 2.5, which is a re-print of a graph found in the original work. As the cone semi-angle increases, the measured hardness divided by the yield stress tend to the same value (≈ 3) for both cases: soft cone/hard surface and hard cone/soft surface. For large cone semi-angles, the supporting contact pressure is practically the same either if the indenter is softer or harder than the surface. As it will be seen in the experimental part of this study, the mean slope of a typical asperity is 6° and the shape of the asperities is approximately spherical near the tips, which imply that the equivalent mean semi-angle near the tips is more than 84°. In this range of cone semi-angle values, it does not matter if the rough surface is harder or softer than the smooth surface because the results are practically the same. If the two surfaces have similar hardness and mutual deformation takes place, it is also expected from the work of Bowden and Tabor (1964) that the behavior of the plastic contact hardness will be the same as if one surface is harder than the other.

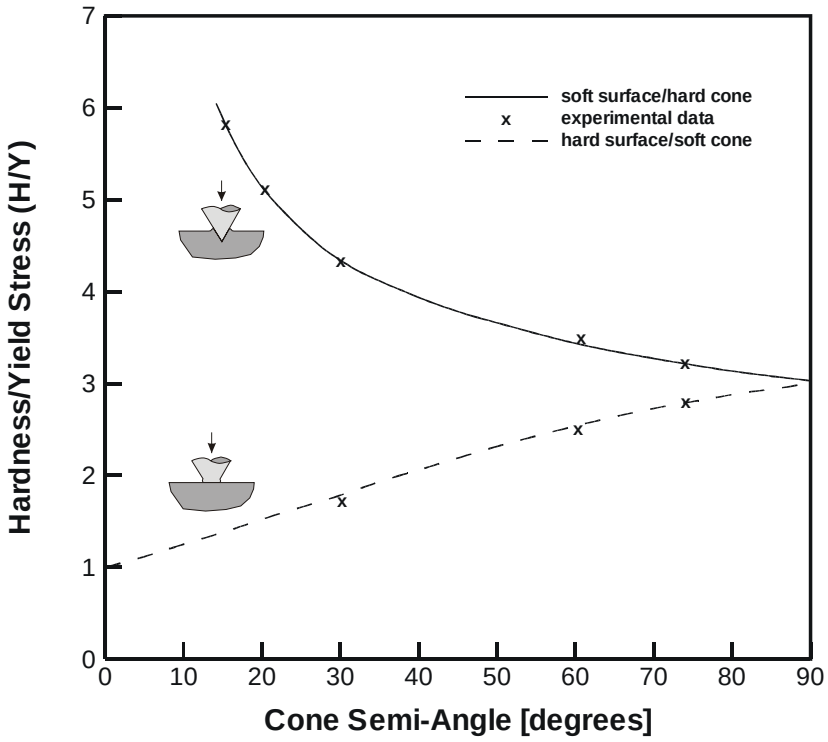

Figure 2.5 – Hardness/yield stress versus cone semi-angle
(reproduced from Bowden and Tabor, 1964, fig. 8, Vol. I, Chapter 1)

Based on the geometrical analysis presented by Cooper, Mikic and Yovanovich (1969), Mikic (1971) and Yovanovich (1982) presented different but equivalent expressions for the contact parameters needed in the thermal model Eq. (2.10). Cooper, Mikic and Yovanovich (1969) assumed that the distribution of surface heights and slopes are Gaussian and independent from each other, and modeled the contact of a perfectly flat and smooth surface against a nominally flat rough surface. For a separation Y between the flat surface and the mean plane of the rough surface (Fig. 2.6), the contact parameters n and a are given by:

$$n = \frac{1}{16}\left(\frac{m}{\sigma}\right)^2 \frac{\exp\left(-\lambda^2\right)}{\operatorname{erfc}\left(\lambda/\sqrt{2}\right)} \tag{2.22}$$

$$a = \sqrt{\frac{8}{\pi}}\frac{\sigma}{m}\exp\left(\lambda^2/2\right)\operatorname{erfc}\left(\lambda/\sqrt{2}\right) \tag{2.23}$$

where:

$$\lambda \equiv \frac{Y}{\sigma} \tag{2.24}$$

is the dimensionless mean separation gap between the contacting surfaces. The mean separation gap is related to the real-to-apparent area ratio according to the following well-known relationship:

$$\frac{A_r}{A_a} = \frac{1}{2}\operatorname{erfc}\left(\frac{\lambda}{\sqrt{2}}\right) \tag{2.25}$$

The expression above is obtained by integrating the Gaussian probability density function between λ and $+\infty$. It represents the probability of surface heights higher than λ, and is equal to the fraction of the total apparent area that is actually in contact with the flat surface (see Fig. 2.6). This fraction of the total apparent area is responsible for supporting the contact load and it is also known as the *bearing area*. The bearing area idea was introduced by the pioneer work of Abbot and Firestone (1935). In other words, if one "cuts" the tips of the asperities at a level λ measured from the mean plane of the surface, the summation of all the areas of the obtained plateaus divided by the total apparent area is equal to the area under the Gaussian probability density function between λ and $+\infty$. The equation above is used to compute the mean separation λ, which must then be substituted into Eqs. (2.22) and (2.23) to compute the remaining contact parameters.

Substituting the contact parameters back into the thermal model (Eq. 2.10) and re-arranging one gets the CMY thermal contact conductance model for asperities undergoing plastic deformation during first loading:

$$C_c \equiv \frac{h_c\,\sigma}{k_s\,m} = \frac{\sqrt{2}}{4\sqrt{\pi}} \frac{\exp\left(-\lambda^2/2\right)}{\left(1-\sqrt{P/H_c}\right)^{3/2}} \tag{2.26}$$

where:

$$\lambda = \sqrt{2}\ \mathrm{erfc}^{-1}\left(\frac{2P}{H_c}\right) \tag{2.27}$$

is the final expression for the mean separation gap, which was derived from Eqs. (2.19) and (2.25).

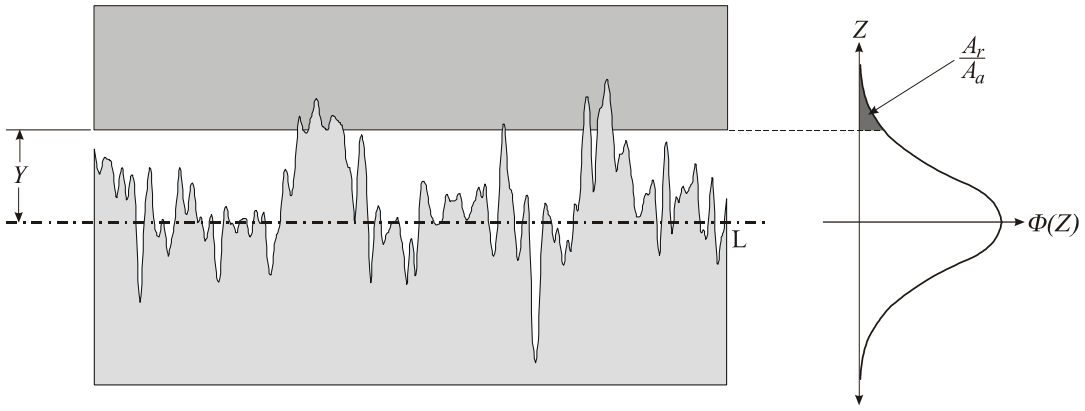

Figure 2.6 – Cooper, Mikic and Yovanovich (1969) model for the contact between a flat and a rough surface

Mikic (1971) proposed a deformation model for the contact parameters during first unloading and subsequent re-loading/unloading of surfaces undergoing plastic deformation during first loading. He assumed that when the contacting surfaces are pressed up to a maximum apparent contact pressure P_{max} [Pa], the asperities deform plastically and the model of Cooper, Mikic and Yovanovich (1969) is valid. When the contact pressure is released to a new value $P < P_{max}$, the deformation is elastic and will remain elastic for further pressure variations provided the surfaces are not pulled apart and provided the new contact pressure do not exceed P_{max}, i. e., for $0 < P < P_{max}$. Assuming that the asperities are approximately spherical near the tips, he used results from the Hertz elastic contact theory (Johnson, 1985) and geometrical considerations to compute the size and the number of contact spots during unloading. The set of equations proposed by Mikic (1971) to compute the contact parameters during unloading and subsequent re-loading/unloadings are:

$$\alpha\Big|_{unloading} \equiv \frac{\sigma}{m} n\, a\Big|_{unloading} = 2\sqrt{2}\int_{Z}^{\infty}\sqrt{\bar{\rho}}\;\bar{n}'\,X^{2}\left(1-\frac{Z}{X}\right)^{1/2}dX \tag{2.28}$$

$$\frac{P}{H_{max}}\Big|_{unloading} = 4\pi\int_{Z}^{\infty}\bar{\rho}\;\bar{n}'\,X^{3}\left(1-\frac{Z}{X}\right)^{3/2}dX \tag{2.29}$$

$$\frac{A_r}{A_a}\Big|_{unloading} = 4\pi\int_{Z}^{\infty}\bar{\rho}\;\bar{n}'\,X^{3}\left(1-\frac{Z}{X}\right)dX \tag{2.30}$$

$$n\Big|_{unloading} = n_{max} - 2\int_{0}^{Z}\bar{n}'\,X\;dX \tag{2.31}$$

where:

$$\bar{\rho} \equiv \rho\frac{m^2}{\sigma} = \frac{\lambda}{(2\pi)^{3/2}}\frac{\exp\left(-\lambda^2/2\right)}{\bar{n}'} \tag{2.32}$$

is the dimensionless radius of curvature of the asperity tips, and:

$$\bar{n}' \equiv -\frac{\sigma^2}{m^2}\frac{d\,n}{d\,\lambda} = \frac{1}{8}\frac{\exp\left(-\lambda^2\right)}{\operatorname{erfc}\left(\lambda/\sqrt{2}\right)}\left[\lambda - \frac{1}{\sqrt{2\pi}}\frac{\exp\left(-\lambda^2/2\right)}{\operatorname{erfc}\left(\lambda/\sqrt{2}\right)}\right] \tag{2.33}$$

is the dimensionless variation of number of contact spots with the mean separation gap λ. The dimensionless parameter X, appearing in the expressions above, represents the contact spot radii at the maximum contact pressure and is defined as:

$$X \equiv \frac{a_{i,max}}{\sqrt{2\rho\sigma}} \tag{2.34}$$

The dimensionless parameter Z represents the maximum value of X and is defined as:

$$Z \equiv \frac{4}{3\pi}\frac{\zeta\,E'}{H_{max}\sqrt{2\rho\sigma}} \tag{2.35}$$

where ζ [m] is the amount that the mean surface planes are displacement during unloading, E' is the equivalent Young's Modulus (defined by Eq. 2.39) and H_{max} is the plastic hardness evaluated at P_{max} from Eq. (2.21). In Eqs. (2.32) and (2.33), λ must be evaluated at $\lambda_{max}+X^2$, where λ_{max} and n_{max} (Eq. 2.31) are the mean separation gap and the number of contact spots, also evaluated at the maximum contact pressure P_{max} from Eqs. (2.25) and (2.22), respectively. This model requires a computational code to evaluate the contact parameters as follows. For a given contact pressure $P < P_{max}$, Eq. (2.29) is solved for Z, which is then substituted into (2.28), (2.30) and (2.31) to compute a, A_r / A_a and n during unloading. With the contact parameters computed, the thermal model (Eq. 2.10) is then employed to compute the thermal contact conductance. The Mikic (1971) model described here was the only

thermal contact conductance model for unloading found in the literature. Mikic (1971) compared his model against a few experimental data points available in the literature and the agreement was fair. No further studies were found in the literature comparing Mikic's (1971) or any other unloading model with experiments.

Mikic (1974) proposed an elastic model to compute the contact parameters for surfaces experiencing fully elastic deformation. He assumed that the asperities have a spherical shape near their tips and employs results from the Hertz elastic contact theory to adapt the CMY plastic model to the case of elastic deformation. The author adapted the CMY plastic model for the case of elastic deformation by employing the following reasoning. When a elastic sphere of radius β is pressed against a flat surface so that the displacement of the center of the sphere is δ, the contact area, computed using the Hertz elastic contact theory, is $A_{elastic} = \pi \delta \beta$. On the other hand, when a plastic sphere is pressed against a flat surface, by means of geometrical considerations one can compute the contact area as $A_{plastic} = 2\pi \delta \beta$. Therefore, for the same displacement, the contact area under elastic deformation is half the contact area under plastic deformation, i. e., $A_{elastic} = (1/2)\, A_{plastic}$ and the contact radius is $a_{elastic} = \left(1/\sqrt{2}\right) a_{plastic}$. With these results, and with the expressions for $a_{plastic}$ and $A_{plastic}$ given by Eqs. (2.23) and (2.25), respectively, the contact parameters under elastic deformation are given by:

$$a\big|_{elastic} = \frac{2}{\sqrt{\pi}} \frac{\sigma}{m} \exp\left(\lambda^2/2\right) \operatorname{erfc}\left(\lambda/\sqrt{2}\right) \tag{2.36}$$

$$\left.\frac{A_r}{A_a}\right|_{elastic} = \frac{1}{4} \operatorname{erfc}\left(\frac{\lambda}{\sqrt{2}}\right) \tag{2.37}$$

The real-to-apparent area ratio under elastic deformation was presented by Mikic (1974):

$$\left.\frac{A_r}{A_a}\right|_{elastic} = \frac{P}{H_e} = \frac{P\sqrt{2}}{E'm} \tag{2.38}$$

where *E'* is the equivalent Young's modulus of the two contacting surfaces, computed as a function of the Young's moduli (E) and the Poisson's ratios (υ) of the two contacting surfaces (A and B) by means of the following expression:

$$E' = \left(\frac{1-\upsilon_A^2}{E_A} - \frac{1-\upsilon_B^2}{E_B} \right)^{-1} \tag{2.39}$$

For the case of anisotropic surfaces, the contact parameters according to De Vaal's (1988) thermal model (Eq. 2.11) are given by:

$$a = \frac{2\sqrt{2}}{\sqrt{\pi}} \frac{\sigma}{m_{mn}} \exp\left(\frac{\lambda^2}{2}\right) \operatorname{erfc}\left(\frac{\lambda}{\sqrt{2}}\right) \tag{2.40}$$

$$b = \frac{2\sqrt{2}}{\sqrt{\pi}} \frac{\sigma}{m_{mx}} \exp\left(\frac{\lambda^2}{2}\right) \operatorname{erfc}\left(\frac{\lambda}{\sqrt{2}}\right) \tag{2.41}$$

where m_{mx} and m_{mn} are the maximum and minimum values of the combined surface mean absolute slope. The minimum absolute slope is measured from a profile parallel to the grooves left by the grinding wheel and the maximum absolute slope is measured perpendicular to the groves. The density of contact spots n for the contact of anisotropic surfaces is the same as for isotropic surfaces (Eq. 2.22). The mean separation gap λ is also computed in the same way as the isotropic surfaces (Eq. 2.25). The dimensionless plastic contact pressure (P/H_c) of ground surfaces is computed using Eq. (2.21) by replacing the mean absolute slope by the geometric mean of the minimum and maximum absolute slope, i. e.:

$$m = \sqrt{m_{mn}\, m_{mx}} \tag{2.42}$$

The application of one of the deformation models (elastic or plastic) requires the knowledge of the type of deformation a priori, which is not an easy task, as discussed by Mikic (1971), (1974) and by Greenwood and Williamson (1966). Both Greenwood and Williamson (1969) and Mikic (1974) developed plasticity indexes to determine the predominant deformation mode. Both works agree that the deformation mode depends very little on the nominal contact pressure but are mostly affected by mechanical properties and asperity geometry. The plasticity index proposed by Greenwood and Williamson (1966) is given by:

$$\Psi \equiv \frac{E'}{H_c} \left(\frac{\sigma}{\beta}\right)^{1/2} \tag{2.43}$$

where β [m] is the mean asperity tip radius. According to the authors, when Ψ is less than 0.6, deformation is predominantly elastic and when Ψ is more than 1, plastic deformation should appear even for the lightest contact pressure. For $0.6 < \Psi < 1$, some intermediate behavior, called elastoplastic, takes place.

The plasticity index proposed by Mikic (1974) is defined as:

$$\gamma \equiv \frac{H_c}{m\, E'} \tag{2.44}$$

The deformation is predominantly plastic when $\gamma \leq 0.33$, elastic when $\gamma \geq 3$, and elastoplastic when $0.33 < \gamma < 3$.

Sridhar and Yovanovich (1996) proposed an elastoplastic deformation model. They employed a technique to compute the contact parameters by blending the fully-elastic model of Mikic (1974) (Eqs. 2.22 and 2.34 to 2.37) and the fully-plastic CMY model (Eqs. 2.19 and 2.22 to 2.25). The contact parameters are given by the following expressions:

$$a\big|_{ep} = \sqrt{f_{ep}}\sqrt{\frac{8}{\pi}}\frac{\sigma}{m}\exp\left(\lambda^2/2\right)\operatorname{erfc}\left(\lambda/\sqrt{2}\right) \tag{2.45}$$

$$\left.\frac{A_r}{A_a}\right|_{ep} = \frac{f_{ep}}{2}\operatorname{erfc}\left(\frac{\lambda}{\sqrt{2}}\right) \tag{2.46}$$

The density of contact spots n is the same as the elastic and plastic models (Eq. 2.22). In the expressions above, f_{ep} is a function that takes into account for the amount of elastoplastic deformation and assumes values between 0.5 and 1. For f_{ep}= 0.5, the expressions above give the same results as the elastic model of Mikic (1974) (Eqs. 2.34 and 2.35), and for f_{ep}= 1, the CMY plastic model is obtained (Eqs. 2.23 and 2.25). The elastoplastic contact pressure H_{ep} [Pa] and the elastoplastic function f_{ep} are computed by solving simultaneously the following two equations:

$$\frac{P}{H_{ep}} = \left[\frac{0.9272\,P}{c_1\left(1.62\frac{\sigma}{m}f_{ep}^{0.429}\right)^{c_2}}\right]^{\frac{1}{1+0.071c_2}} \tag{2.47}$$

$$f_{ep} = \left[1+\left(6.5\Big/4.61\sqrt{\left(\frac{E'm}{H_{ep}}\right)^2-2}\right)^2\right]^{\frac{1}{2}} \Bigg/ \left[1+\left(13\Big/4.61\sqrt{\left(\frac{E'm}{H_{ep}}\right)^2-2}\right)^{1.2}\right]^{\frac{1}{1.2}} \tag{2.48}$$

2.5.4 Correlations for the CMY based models

In order to simplify the manipulation of the models presented in the previous subsections, correlations were proposed by the respective authors. Yovanovich (1982) developed the following correlation for the CMY plastic model for isotropic surfaces (Eqs. 2.26 and 2.27):

$$C_c \equiv \frac{h_c}{k_s}\frac{\sigma}{m} = 1.25\left(\frac{P}{H_c}\right)^{0.95} \tag{2.49}$$

According to the author, the maximum difference between the exact solution and the correlation above is 1.5%. Mikic (1974) proposed the following correlation for his isotropic elastic model:

$$C_c \equiv \frac{h_c}{k_s}\frac{\sigma}{m} = 1.55\left(\frac{P\sqrt{2}}{E'm}\right)^{0.94} \tag{2.50}$$

De Vaal (1988) also presented a correlation for the anisotropic plastic model:

$$\frac{h_c}{k_s}\frac{\sigma}{\left(\sqrt{m_{2mx}m_{2mn}}\right)^{\frac{1}{2}}} = \left(0.986 - \frac{0.0075}{\nu}\right)\left(\frac{P}{H_c}\right)^{\left(0.95-\frac{0.004}{\nu}\right)} \tag{2.51}$$

Sridhar and Yovanovich (1996) presented the following correlation for their elastoplastic model:

$$\frac{h_c}{k_s}\frac{\sigma}{m} = \begin{cases} 1.54\left(\dfrac{P}{H_{ep}}\right)^{0.94} & 0 < \varepsilon_c < 5 \quad \text{(Mikic, 1974)} \\ 1.245\left(1+\dfrac{46690.2}{\varepsilon_c^{2.48}}\right)^{\frac{1}{30}}\left(\dfrac{P}{H_{ep}}\right)^{0.948\left(\frac{1}{1+\frac{2086.9}{\varepsilon_c^{1.842}}}\right)^{\frac{1}{600}}} & 5 < \varepsilon_c < 400 \\ 1.25\left(\dfrac{P}{H_{ep}}\right)^{0.95} & 400 < \varepsilon_c < \infty \quad \text{(Yovanovich, 1982)} \end{cases} \tag{2.52}$$

with:

$$\varepsilon_c = 1.67\frac{E'}{S_f}m \tag{2.53}$$

$$S_f = \frac{1}{2.76\sqrt{\dfrac{1}{H_{ep}^2} - \dfrac{1}{H_e^2}}} \tag{2.54}$$

2.6. Summary

This chapter presented a review of part of the existing theory on thermal contact conductance. The three sub-models that constitute a typical thermal contact conductance model were presented in details. Special focus was placed on the models based on the work of Cooper et al. (1969), which form the basis of the Truncated Gaussian model, developed in the next Chapter.

CHAPTER 3
THEORETICAL ANALYSIS

3.1. Introduction

In this chapter, new thermal contact conductance models, called Truncated Gaussian-TG are presented for first loading and unloading. The TG thermal contact conductance models are based on the TG surface geometry model, first proposed by Song (1988), and on the CMY based thermal contact conductance model, reviewed in the previous chapter. Modifications are also incorporated into the model of Song and Yovanovich (1988) for the plastic contact hardness (Eq. 2.21) according to the TG geometry model.

3.2. Height distribution of real surfaces

According to the fully Gaussian geometry model, employed in practically all the theoretical models available in the literature, surfaces should possess infinitely high asperities. The surfaces should also present valleys infinitely deep, because the Gaussian probability function is never zero. Obviously, infinitely high asperities and infinitely deep valleys are impossible to occur in real life. Therefore, the real distribution of surface heights has both tails shortened or truncated. The question that now arises is how much the truncation of the surface height distribution affect thermal contact conductance. This subject will be analyzed now as a motivation for the introduction of the TG thermal contact conductance model.

The assumption of Gaussian height distribution was first analyzed in more details by Greenwood and Williamson (1966). They measured surface roughness profiles of bead blasted aluminum surfaces and concluded that the Gaussian distribution is a good approximation at least in the range of surface heights between $\pm 2\,\sigma$. They suggest that for surface heights out of this range the assumption of fully Gaussian distribution of surface heights is not straightforward. Several other researchers (De Vaal, 1988, Song, 1988, Nho, 1990, among many others) also measured profile height distributions of actual machined surfaces and concluded that the Gaussian model is a good approximation. They presented actual surface profile height measurements that were truncated between *3* and 4σ, but most of them did not notice the truncation. Only Song (1988) identified the consequences of the truncation of surface height distribution on the contact conductance problem. He was studying the gap conductance problem and proposed a modified expression to compute the mean separation gap between the contacting surfaces based on the TG geometry model.

As mentioned before, Figure 2.3 shows measured surface height distributions obtained from three different profiles of a typical bead blasted SS 304 surface used in the experimental work presented here. The Gaussian model is also plotted in this graph and it is in good agreement with the measurements for surface heights, especially in the range of $1.5 \leq z/\sigma \leq 3.7$. In typical engineering applications, the mean separation between the contacting surfaces lies in this range. However, if this surface is brought into contact with a flat lapped surface, for instance, under a contact pressure of $P/H_c=10^{-6}$, which is a very light contact pressure, one can use the Gaussian geometry model (Eqs. 2.19, 2.21 and 2.25) to calculate a mean separation gap of $Y \cong 4.7\sigma$. However, the measured profile height distributions do not show height measurements beyond 3.7σ. The profile height distributions follow the Gaussian distribution up to $z \cong 3.7\sigma$, where they are truncated. Provided that $z \cong 3.7\sigma$ the height of the highest asperity, it is expected that the maximum mean plane separation under the lightest contact load should be less than 3.7σ. Therefore, the Gaussian geometry model seems to over predict the mean plane separation under these circumstances. A brief analysis of Eqs. (2.10) and (2.22) to (2.25) shows that thermal contact conductance increases as the mean separation gap decreases. Therefore, as the actual mean separation is smaller than predicted by the Gaussian model, the actual thermal contact conductance will be larger than predicted by the existing theory.

Sridhar and Yovanovich (1994) reviewed several thermal contact conductance models available in the literature and compared the models against thermal contact conductance data from Hegazy (1985), Antonetti (1983) and Mc Waid (1990), for various metals and roughness levels. They concluded that the CMY plastic model and the Mikic (1974) elastic model, reviewed in Chapter 2, are easier to manipulate and need less surface geometry parameters than the other models reviewed. They also concluded that these models were more accurate, especially at high contact pressures. At low contact pressures, the models systematically underpredict the experiments. The same was observed by De Vaal (1988) during his experiments. Hegazy (1985) and De Vaal (1988) tried to explain this unexpected behavior of thermal contact conductance at low contact pressures as a consequence of thermal expansion of the test samples during the warm up of the experiments. Hegazy (1985) tried to propose a semi-empirical correlation for thermal contact conductance at light loads, based on his experimental points. However, the authors stressed that thermal expansion of the samples was not a definitive answer to this phenomenon.

The truncation of the highest asperities explains qualitatively this behavior very well. At light contact pressures the truncation of the few truncated asperities is very important, but

as the pressure increases, more and more asperities that are not truncated come into contact, the effect of the truncated asperities become negligible, and the Gaussian model makes the theory predict the experiments well. Based on this reasoning, a new thermal contact conductance model, the Truncated Gaussian model, was developed and is presented here.

3.3. Truncated Gaussian -TG model

The TG thermal contact conductance model is based on the CMY work and on the TG geometry model. A more complex version of the TG geometry model was suggested by Song (1988) to explain a similar unexpected behavior of the gap conductance at light contact pressures. The version of the TG geometry model used here is simpler and easier to manipulate than the version suggested by Song (1988). According to the Truncated Gaussian model used here, the surface heights probability density function follow the Gaussian distribution for surface heights smaller than or equal z_{trunc}, which is the truncation level of the distribution. The surface does not present asperities higher than z_{trunc}. Figure 3.1 shows the basic difference between the fully Gaussian and the Truncated Gaussian surface geometry models. The fully Gaussian model predicts the existence of asperities heights in the range of $-\infty < z < +\infty$, while the Truncated Gaussian model predicts asperities between $-\infty < z \leq z_{trunc}$. Actually, it is impossible to find valleys infinitely deep, as discussed before. However, from a contact mechanics point of view, it does not matter what happens to the surface heights distribution for $z < 1.5$. As mentioned before, in practical engineering applications, the mean separation is always larger than 1.5σ. So, it is assumed here that the Gaussian is a good representation of the probability density function for surface heights between $1.5 < z \leq z_{trunc}$.

If one integrates the Gaussian curve over an interval smaller than $-\infty < z < +\infty$, the result is smaller than 1. But the integration of any probability density function $\phi(z)$ over the entire range of possibilities of the independent variable z must yield 1. To overcome this problem, it is simply assumed here that in the negative part of the distribution ($z < 0$), the Gaussian curve is multiplied by a factor so that the integration of the new curve is 1. Actually, it is important that the surface heights distribution follow the Gaussian curve only for $1.5 < z \leq z_{trunc}$. This assumption is the basic difference between the TG geometry model used here and the version used by Song (1988). That researcher was concerned about which constant value should multiply the truncated Gaussian curve so that the integration over the entire range of possibilities of z would yield 1. The resulting expression he obtained was then very complex and difficult do manipulate. In the version of the TG model used here, it is assumed that the actual shape of the probability density function yields 1 when integrated

over the entire range of possibilities of z and that the Gaussian curve is obeyed between $1.5 < z \leq z_{trunc}$.

As discussed in the last chapter, the real-to-apparent area ratio A_r / A_a in the contact between a rough surface indenting a flat surface separated by a distance λ is equal to the area under the probability density function of surface heights between $\lambda \leq z < \infty$. This relation is given by Eq. (2.25), rewritten here for convenience:

$$\frac{A_r}{A_a} = \frac{1}{2}\text{erfc}\left(\frac{\lambda}{\sqrt{2}}\right) \tag{2.25}$$

Since according to the TG model the distribution of surface heights is truncated at $z = z_{trunc}$, the relation between the real-to-apparent area ratio A_r / A_a and the mean separation gap λ_{TG} is obtained by integrating the Gaussian curve between $\lambda_{TG} \leq z \leq z_{trunc}$, where λ_{TG} is the mean separation gap according to the TG model:

$$\frac{A_r}{A_a} = \frac{1}{2}\text{erfc}\left(\frac{\lambda_{TG}}{\sqrt{2}}\right) - \frac{1}{2}\text{erfc}\left(\frac{z_{trunc}}{\sqrt{2}}\right) \tag{3.1}$$

The expression above is obtained by integrating the Gaussian probability density function between λ_{TG} and z_{trunc}, that is, it represents the probability of surface heights between the mean separation gap λ_{TG} and the maximum surface height z_{trunc}.

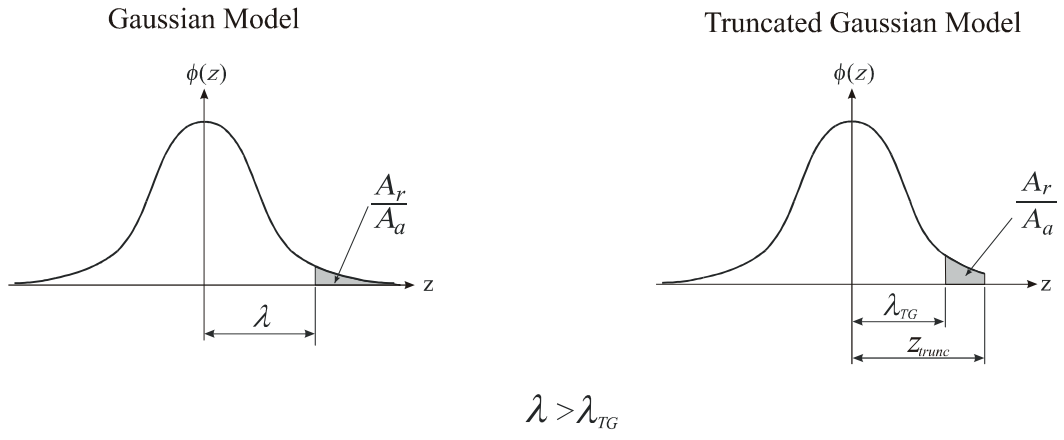

Figure 3.1 – Comparison between the Gaussian and the Truncated Gaussian models

Using the idea of "bearing area" discussed in the previous chapter, the expression above is stating that the real-to-apparent area ratio is equal to the bearing area at the mean separation λ_{TG} minus the bearing area at the truncation level z_{trunc}, which is also equivalent to say that the bearing area of the truncated part of the surface must be subtracted from the total

bearing area. As illustrated in Fig. 3.1, $\lambda_{TG} < \lambda$ and the thermal contact conductance according to the TG model is larger than the conductance according to the fully Gaussian model, as discussed before. The equation above form the basis of the TG thermal contact conductance model for asperities experiencing plastic deformation. The other contact parameters are derived in the following sections. The contact parameters under plastic deformation for both loading and unloading are derived first. Then the contact parameters under elastic deformation according to the Mikic (1974) model are deduced.

3.4. Contact parameters under plastic deformation during first loading

In the Truncated Gaussian model, it is assumed that the higher asperities are shorter than predicted by the fully Gaussian model, but they are not missing. The total number of asperities at a given mean separation λ remains the same as the fully Gaussian model, although the asperities which were supposed to present heights above z_{trunc} are truncated at this level. Based on this model, the expression for the contact spot density n, Eq. (2.22), is still valid. The mean separation gap is obtained by solving Eq. (3.1) for λ_{TG}. The real-to-apparent area ratio is computed in the same way as presented before in Eq. (2.19), because this expression was obtained by a force balance and does not dependent on the geometry model employed. The mean contact spot radius a, is derived from Eq. (3.1) and from the expression for the density of contact spots n (Eq. 2.22) as follows. The number of contact spots per unit area (n) multiplied by the area of each contact spot (πa^2) must be equal to the real-to-apparent area ratio A_r/A_a, i. e.:

$$n \pi a^2 = \frac{A_r}{A_a} \tag{3.2}$$

Substituting Eqs (2.22) and (3.1) into the expression above and rearranging, one gets the expression for the mean contact spot radius according to the TG plastic model:

$$a = \sqrt{\frac{8}{\pi}} \frac{\sigma}{m} \exp\left(\lambda_{TG}^2/2\right) \operatorname{erfc}\left(\lambda_{TG}/\sqrt{2}\right) \sqrt{1 - \frac{\operatorname{erfc}\left(z_{trunc}/\sqrt{2}\right)}{\operatorname{erfc}\left(\lambda_{TG}/\sqrt{2}\right)}} \tag{3.3}$$

Substituting the expression for the contact parameters into the thermal model (Eq. 2.10) and rearranging the resulting expression one obtains the TG thermal contact conductance model for surfaces undergoing plastic deformation during first loading:

$$C_c \equiv \frac{h_c \, \sigma}{k_s \, m} = \frac{\sqrt{2}}{4\sqrt{\pi}} \frac{\exp\left(-\lambda_{TG}^2/2\right)}{\left(1 - \sqrt{P/H_c}\right)^{3/2}} \sqrt{1 - \frac{\operatorname{erfc}\left(z_{trunc}/\sqrt{2}\right)}{2P/H_c + \operatorname{erfc}\left(z_{trunc}/\sqrt{2}\right)}} \tag{3.4}$$

where:

$$\lambda_{TG} = \sqrt{2}\ \mathrm{erfc}^{-1}\left[\frac{2P}{H_c} + \mathrm{erfc}\left(\frac{z_{trunc}}{\sqrt{2}}\right)\right] \tag{3.5}$$

The effect of the truncation of surface heights on thermal contact conductance can be observed by analyzing the two expressions above. At high contact pressures, the term $\{P/H_c\}$ is much larger than the term $\{\mathrm{erfc}\left(z_{trunc}/\sqrt{2}\right)\}$, so the truncation is negligible and the TG model is exactly the same as the fully Gaussian CMY model (Eqs. 2.26 and 2.27). At low contact pressures, when $\{P/H_c\}$ and $\{\mathrm{erfc}\left(z_{trunc}/\sqrt{2}\right)\}$ have the same order of magnitude, the truncation effect is important.

Comparing Eq. (3.3) (TG model) with Eq. (2.23) (fully Gaussian model), one can see that the basic difference between the two expressions is the term $\sqrt{1-\mathrm{erfc}(z_{trunc}/\sqrt{2})/\mathrm{erfc}(\lambda_{TG}/\sqrt{2})}$, which is present in the TG model. This term accounts for the truncation effect on the mean contact spot radius. When applying the TG model into the anisotropic model proposed by De Vaal (1988), Eqs. (2.39) and (2.40) must also be multiplied by this term.

3.5. Contact parameters during unloading

The model developed by Mikic (1971), which is the only analytical thermal contact conductance model for unloading found in the literature (Eqs. 2.28 to 2.33), is adapted here according to the TG geometry model. Following the same procedure as adopted to develop Eq. (3.1), the bearing area of the truncated asperities $[(1/2)\,\mathrm{erfc}\left(z_{trunc}/\sqrt{2}\right)]$ must be subtracted from the total bearing area (A_r/A_a) (Eq. 2.30), i. e.:

$$\left.\frac{A_r}{A_a}\right|_{unloading}^{TG} = 4\pi \int_Z^{\infty} \bar{\rho}\ \bar{n}'\ X^3 \left(1 - \frac{Z}{X}\right) dX - \frac{1}{2}\mathrm{erfc}\left(\frac{z_{trunc}}{\sqrt{2}}\right) \tag{3.6}$$

In a similar way, the load supported by the area associated to the truncated asperities must be subtracted from the total contact load, i. e.:

$$P\big|_{unloading}^{TG} A_a = P\big|_{unloading} A_a - P_c \frac{1}{2}\mathrm{erfc}\left(\frac{z_{trunc}}{\sqrt{2}}\right) A_a \tag{3.7}$$

where P_c [Pa] is the real contact pressure, supported by the asperities in contact. Dividing the expression above by $A_a H_{max}$, one gets:

$$\left.\frac{P}{H_{max}}\right|_{unloading}^{TG} = \left.\frac{P}{H_{max}}\right|_{unloading} - \frac{P_c}{H_{max}} \frac{1}{2}\mathrm{erfc}\left(\frac{z_{trunc}}{\sqrt{2}}\right) \tag{3.8}$$

By means of a force balance resulting from the apparent and the real pressures, one obtains:

$$P\,A_a = P_c\,A_r\Big|_{unloading}^{TG} \quad \Rightarrow \quad P_c = P\,\frac{A_a}{A_r}\Big|_{unloading}^{TG} \tag{3.9}$$

Substituting Eqs. (3.9), (3.6) and (2.29) into Eq. (3.8) and rearranging, one obtains:

$$\frac{P}{H_{max}}\Big|_{unloading}^{TG} = \frac{4\pi \int_Z^\infty \bar{\rho}\,\bar{n}'\,X^3\left(1-\frac{Z}{X}\right)^{3/2} dX}{\left[1+\frac{(1/2)\,\mathrm{erfc}\left(z_{trunc}/\sqrt{2}\right)}{4\pi \int_Z^\infty \bar{\rho}\,\bar{n}'\,X^3\left(1-\frac{Z}{X}\right) dX - \frac{1}{2}\mathrm{erfc}\left(\frac{z_{trunc}}{\sqrt{2}}\right)}\right]} \tag{3.10}$$

where $\bar{\rho}$ and $\bar{n}'$ are given by Eqs. (2.32) and (2.33), respectively. In the TG model, the density of contact spots is the same as the fully Gaussian model, as already mentioned. Therefore, Eq. (2.31) is used to compute n. The last contact parameter, the mean contact spot radius a, is computed from Eq. (3.2), which rearranged gives:

$$a\Big|_{unloading}^{TG} = \sqrt{\frac{1}{n\,\pi}\frac{A_r}{A_a}\Big|_{unloading}^{TG}} \tag{3.11}$$

In Eqs. (3.6) and (3.10), λ must be evaluated at $\lambda_{max}+X^2$. The parameters λ_{max}, H_{max}, and n_{max}, are valuated at the maximum contact pressure P_{max}. Similarly to the original model of Mikic (1971), the unloading TG model requires a numerical procedure to compute the contact parameters. For a given contact pressure $P<P_{max}$, Eq. (3.11) is solved for Z, which is then substituted in Eqs. (3.6), (2.31) and (3.11) to compute A_r/A_a, n and a, respectively.

3.6. Contact parameters under elastic deformation

For the case of elastic deformation, the Mikic (1974) model is adapted using the same procedure as described to deduce Eqs. (2.34) and (2.35): the elastic contact area is half the plastic contact area, for the same mean separation gap (as discussed in the last chapter). Dividing Eq. (3.1) by two, the real-to-apparent area ratio under elastic deformation is:

$$\frac{A_r}{A_a}\Big|_{elastic} = \frac{1}{4}\mathrm{erfc}\left(\frac{\lambda_{TG}}{\sqrt{2}}\right) - \frac{1}{4}\mathrm{erfc}\left(\frac{z_{trunc}}{\sqrt{2}}\right) \tag{3.12}$$

The mean contact spot radius is $a_{elastic} = \left(1/\sqrt{2}\right) a_{plastic}$, i. e.:

$$a_{elastic} = \frac{2}{\sqrt{\pi}} \frac{\sigma}{m} \exp\left(\lambda_{TG}^2 / 2\right) \operatorname{erfc}\left(\lambda_{TG} / \sqrt{2}\right) \sqrt{1 - \frac{\operatorname{erfc}\left(z_{trunc} / \sqrt{2}\right)}{\operatorname{erfc}\left(\lambda_{TG} / \sqrt{2}\right)}} \tag{3.14}$$

The expressions to compute the real-to-apparent contact area under elastic deformation from the elastic properties of the metals, given by Eqs. (2.36) and (2.37), are still valid in the TG model because they were developed based on force balances and do not depend on the type of surface geometry model employed.

3.7. Plastic contact pressure

The model proposed by Song and Yovanovich (1988) to compute the plastic contact pressure as a function of roughness parameters and surface micro-hardness, presented here as Eq. (2.21), was developed assuming fully Gaussian distribution of surface heights. This model will now be adapted according to the Truncated Gaussian geometry model. The development to be presented here will follow the same steps as the original model.

It is convenient to remember that the objective of this model is to compute the appropriate micro-hardness near the surface. Under contact pressure, the asperities deform in a similar way to the Vickers micro-hardness test, according to the discussion presented in Section 2.5.4. The relationship between the radius of a circular contact spot a and the diagonal d_v of a square indentation of a Vickers micro-hardness test, both having the same area, is given by:

$$d_v = \sqrt{2\pi}\, a \tag{3.14}$$

Adopting arbitrarily a reference diagonal of $d_0 = 1$ μm in Eq. (2.20) and assuming that the plastic contact hardness H_c can be represented by the Vickers micro-hardness H_v, Eq. (3.14) is substituted into Eq. (2.20) and after multiplying both sides by P and rearranging the resulting expression one obtains:

$$\frac{P}{H_c} = \frac{P}{c_1} \left(\sqrt{2\pi}\, a\right)^{-c_2} \tag{3.15}$$

Substituting the expression for a (Eq. 3.3) into the expression above, and introducing Eqs. (3.1) and (2.19) into the final expression and rearranging one gets:

$$\frac{P}{H_c} = \frac{P}{c_1} \left\{ 4 \frac{\sigma}{m} \exp\left(\frac{\lambda_{TG}^2}{2}\right) \sqrt{2 \frac{P}{H_c} \left[2 \frac{P}{H_c} + \operatorname{erfc}\left(\frac{z_{trunc}}{\sqrt{2}}\right) \right]} \right\}^{-c_2} \tag{3.16}$$

The natural logarithm of the expression above, with λ_{TG} given by Eq. (3.5), can be written as:

$$\ln\left(\frac{P}{H_c}\right)=\ln\left\{\frac{P}{c_1}\left[4\frac{\sigma}{m}\sqrt{2\frac{P}{H_c}\left[2\frac{P}{H_c}+\operatorname{erfc}\left(\frac{z_{trunc}}{\sqrt{2}}\right)\right]}\right]^{-c_2}\right\}-c_2\left\{\operatorname{erfc}^{-1}\left[2\frac{P}{H_c}+\operatorname{erfc}\left(\frac{z_{trunc}}{\sqrt{2}}\right)\right]\right\}^2 \tag{3.17}$$

The inverse of the complementary error function is approximated by the following correlation (Yovanovich, 2001):

$$\operatorname{erfc}^{-1}(x)\cong 0.9638\left[-\ln(2.7945x)\right]^{1/2} \tag{3.18}$$

Substituting the correlation above into Eq. (3.17) and finding the anti-logarithm of the final expression, one obtains:

$$\frac{P}{H_c}=\frac{P}{c_1}\left[4\frac{\sigma}{m}\sqrt{2\frac{P}{H_c}\left[2\frac{P}{H_c}+\operatorname{erfc}\left(\frac{z_{trunc}}{\sqrt{2}}\right)\right]}\right]^{-c_2}\left\{2.7945\left[2\frac{P}{H_c}+\operatorname{erfc}\left(\frac{z_{trunc}}{\sqrt{2}}\right)\right]\right\}^{0.9289\,c_2} \tag{3.19}$$

The expression above is the implicit model to compute the plastic contact hardness as a function of the surface roughness parameters σ, m and z_{trunc}, the Vickers micro-hardness correlation coefficients c_1 and c_2 and the apparent contact pressure P. A numerical procedure could be employed in order to compute H_c from the expression above. However, a correlation for this model is developed in the next section in order to make the manipulation of the model easier.

3.8. Correlations

In order to facilitate the manipulation of the TG thermal contact conductance models, approximate correlations were developed and are presented here. The following correlation, presented by Yovanovich (2001), is adopted for the complementary error function:

$$\operatorname{erfc}(x)\cong\left[\sqrt{\pi}\;x\exp\left(x^2\right)\right]^{-1} \tag{3.20}$$

Dividing the TG (Eq. 3.4) by the fully Gaussian (Eq. 2.26) thermal contact conductance plastic models, one obtains:

$$\frac{(C_c)_{TG}}{(C_c)_{Gaussian}}=\frac{\exp\left(-\lambda_{TG}^2/2\right)}{\exp\left(-\lambda^2/2\right)}\sqrt{1-\frac{\operatorname{erfc}\left(z_{trunc}/\sqrt{2}\right)}{2P/H_c+\operatorname{erfc}\left(z_{trunc}/\sqrt{2}\right)}} \tag{3.21}$$

with λ and λ_{TG} given by Eqs. (2.27) and (3.5), respectively. Introducing Eqs. (2.27) and (3.5) as well as the correlations given by Eqs. (3.18) and (3.20) into the expression above yields:

$$\frac{(C_c)_{TG}}{(C_c)_{Gaussian}} = \left(1+\frac{1}{f}\right)^{0.9289}\sqrt{1-\frac{1}{f+1}} \tag{3.22}$$

Where:

$$f \equiv \frac{P}{H_c}\sqrt{2\pi}\, z_{trunc} \exp\left(\frac{z_{trunc}^2}{2}\right) \tag{3.23}$$

For $f > 40$, the difference between the fully Gaussian and the truncated Gaussian thermal contact conductance models is less than 1%. Under this circumstance, the truncation effect can be considered negligible and the original CMY model gives practically the same result as the TG model. As one can see, f increases with both the truncation level z_{trunc} and the dimensionless contact pressure P/H_c. The larger are z_{trunc} (smaller truncation) and P/H_c (higher contact pressure in relation to the contact hardness), the smaller is the effect of the truncation of the surface height distribution on thermal contact conductance.

Substituting the correlation developed by Yovanovich (1982) for $(C_c)_{Gaussian}$ (Eq. 2.49) into Eq. (3.22), one obtains the correlation for the TG thermal contact conductance model for surfaces undergoing plastic deformation:

$$(C_c)_{TG} \equiv \frac{h_c \sigma}{k_s m} = 1.25\left(\frac{P}{H_c}\right)^{0.95}\left(1+\frac{1}{f}\right)^{0.9289}\sqrt{1-\frac{1}{f+1}} \tag{3.24}$$

The maximum difference between the correlation above and the exact solution (Eq. 3.4) is 5% for $P/H_c = 2\cdot10^{-6}$, which is an extremely low contact pressure and not easily encountered in practical applications.

For surfaces undergoing elastic deformation, a similar procedure can be employed to derive a correlation for the TG model from Eqs. (2.10), (2.36), (3.12), (3.13) and from the correlation developed by (Mikic, 1974) (Eq. 2.48) for his fully Gaussian elastic mode. The TG elastic thermal contact conductance correlation is:

$$(C_c)_{TG} \equiv \frac{h_c \sigma}{k_s m} = 1.55\left(\frac{P\sqrt{2}}{E' m}\right)^{0.94}\left(1+\frac{1}{f}\right)^{0.9289}\sqrt{1-\frac{1}{f+1}} \tag{3.25}$$

In the expression above, f is computed using Eq. (3.23) with H_c substituted by H_e. In order to facilitate the manipulation of the plastic contact hardness model (Eq. 3.19), a correlation is developed here. The correlation is obtained by "blending" the asymptotic solutions of Eq. (3.19). This blending technique was successfully used by Sridhar and Yovanovich (1996) to develop the elastoplastic thermal contact conductance model (Eqs. 2.43 and 2.44) from the fully elastic (Mikic, 1974) and the fully plastic (CMY, 1969) models. The first step to apply the technique is to identify the two asymptotic solutions. The first asymptote is the fully

Gaussian solution, i. e., when $z_{trunc} \to \infty$. In this case, $\text{erfc}(z_{trunc}) \to 0$ and Eq. (3.19) reduces to the original Sridhar and Yovanovich (1996) model (Eq. 2.21):

$$\left.\frac{P}{H_c}\right|_{Gaussian} = \left[\frac{P}{c_1\left(1.62\frac{\sigma}{m}\right)^{c_2}}\right]^{\frac{1}{1+0.071c_2}} \tag{3.26}$$

The second asymptote is the case when the truncated area is much larger than the area resulting from the contact pressure, i. e., $\text{erfc}(z_{trunc}) >> P/H_c$. In this case, Eq. (3.19) reduces to:

$$\frac{P}{H_c} = \frac{P}{c_1}\left[4\frac{\sigma}{m}\sqrt{2\frac{P}{H_c}\text{erfc}\left(\frac{z_{trunc}}{\sqrt{2}}\right)}\right]^{-c_2}\left\{2.7945\,\text{erfc}\left(\frac{z_{trunc}}{\sqrt{2}}\right)\right\}^{0.9289\,c_2} \tag{3.27}$$

Substituting the correlation for the complementary error function (Eq. 3.20) in the expression above and solving it for P/H_c, one obtains the second asymptotic solution:

$$\left.\frac{P}{H_c}\right|_{TG} = \left\{\frac{P}{c_1\left(2.4\frac{\sigma}{m}\right)^{c_2}}\left[z_{trunc}\exp\left(\frac{z_{trunc}^2}{2}\right)\right]^{-0.4289c_2}\right\}^{\frac{1}{1+0.5c_2}} \tag{3.28}$$

The blended solution is then computed as:

$$\frac{P}{H_c} = \left[\left(\left.\frac{P}{H_c}\right|_{Gaussian}\right)^{-n} + \left(\left.\frac{P}{H_c}\right|_{TG}\right)^{-n}\right]^{-\frac{1}{n}} \tag{3.29}$$

where n is the blending parameter, which dictates how smooth is the transition between the two asymptotic solutions. It must be obtained by fitting the correlation to the exact solution. The procedure employed to find n consisted of comparing the correlation (Eq. 3.29) to the exact solution (Eq. 3.19) for values of n between 1 and 50 by increments of 1. The parameters that appear in the model (P/c_1, σ/m, z_{trunc} and c_2) were varied in the following ranges:

- $10^{-7} < P/c_1 < 10^{-1}$
- $5 < \sigma/m < 60$
- $3 < z_{trunc} < 4.5$
- $-0.6 < c_2 < 0$

These are the ranges of values that can be encountered in practical applications. A small routine was written using the Maple® algebraic manipulation software. The routine tested the values of n that promoted the minimum difference between the correlation and the exact

solution. It was found that n is affected significantly only by c_2. The values of n were then correlated to the respective values of c_2 and the result is the following:

$$n = 3.9 + 52 \exp(10 c_2) \tag{3.30}$$

The maximum difference between the correlation (Eq. 3.29) with n given by the correlation above and the exact solution (Eq. 3.19) is only ± 3 %.

3.9. Summary

In this Chapter, new thermal contact conductance models, called Truncated Gaussian (TG) models, are presented. These new models are modifications incorporated to existing thermal contact conductance models in order to take into account for the truncated Gaussian surface geometry model. A new plastic contact hardness model was also developed according to the TG surface geometry model.

CHAPTER 4
EXPERIMENTAL STUDY

4.1. Introduction

In this chapter, the procedure employed to obtain experimental data in order to validate the models developed in the previous chapter is presented. The experimental study consisted basically of thermal contact conductance measurements between conforming rough surfaces under vacuum environment. The contact between lapped and bead blasted samples possessing various roughness levels and two distinct metals, SS 304 and Ni 200, is studied. The experimental procedures employed to characterize the surface topography, surface micro-hardness and thermal conductivity of the test samples, which are input parameters for the theoretical models presented previously are also described. A detailed experimental uncertainty analysis is also presented. The experimental data obtained from this study will be compared against the new TG and the existing fully Gaussian thermal contact conductance models.

4.2. Experimental set-up

The experimental set-up used to measure thermal contact conductance is shown in Fig. 4.1. It consists of a cold plate, test column, load cell, electrical heater and loading mechanism. The cold plate is a hollow copper cylinder maintained at a constant temperature by a controlled glycol thermal bath. The temperature of the cold plate is set so that the temperature of the interface between the test samples is maintained approximately at room temperature (20-30°*C*). The test column, consisting of the two test specimens and one ARMCO iron flux-meter, is placed over the cold plate. The specimens and the flux-meters are cylinders of 25 mm in diameter by 45 mm long. The electrical heater is a cylindrical copper block with two cartridge heaters. It is placed on the top of the ARMCO flux-meter and can dissipate up to 60 W. Radiation heat loss from the test column is minimized by evolving it with a polished aluminum tube. The assembly is placed inside a vacuum chamber, which is connected to a mechanical pump and a diffusion pump in series. The vacuum inside the chamber is 10^{-6} Torr.

The contact load is applied to the test column by means of an articulated arm. The loading arm is connected to a shaft and the extremity of the shaft is connected to a nut outside the vacuum chamber as shown in Fig. 4.1. The nut can be rotated by means of a wrench, applying or releasing load to the test column. Between the nut and the chamber base there is a

spring that is designed to absorb thermal expansion of the test column, avoiding contact pressure variations as a function of temperature variation of the test column during transient. The contact load is read by means of a calibrated load cell (make EATON, model 3397) assembled in series with the test column and connected to the data acquisition system.

Six #36 type T thermocouples are attached to each test specimen and to the ARMCO flux-meter. The thermocouples are positioned 5 mm apart from each other and spread along the longitudinal direction. The thermocouple voltages are read by means of a data acquisition system controlled by a personal computer. The thermocouple signals are then converted into temperature values and the load cell signal is converted into load value, using correlations obtained previously. The computational code uses the least square method to find the best linear fit for the temperature distribution inside each test specimen and inside the ARMCO flux-meter. The heat fluxes of each sample are obtained by multiplying the slope of the temperature distributions inside each sample by the respective conductivities.

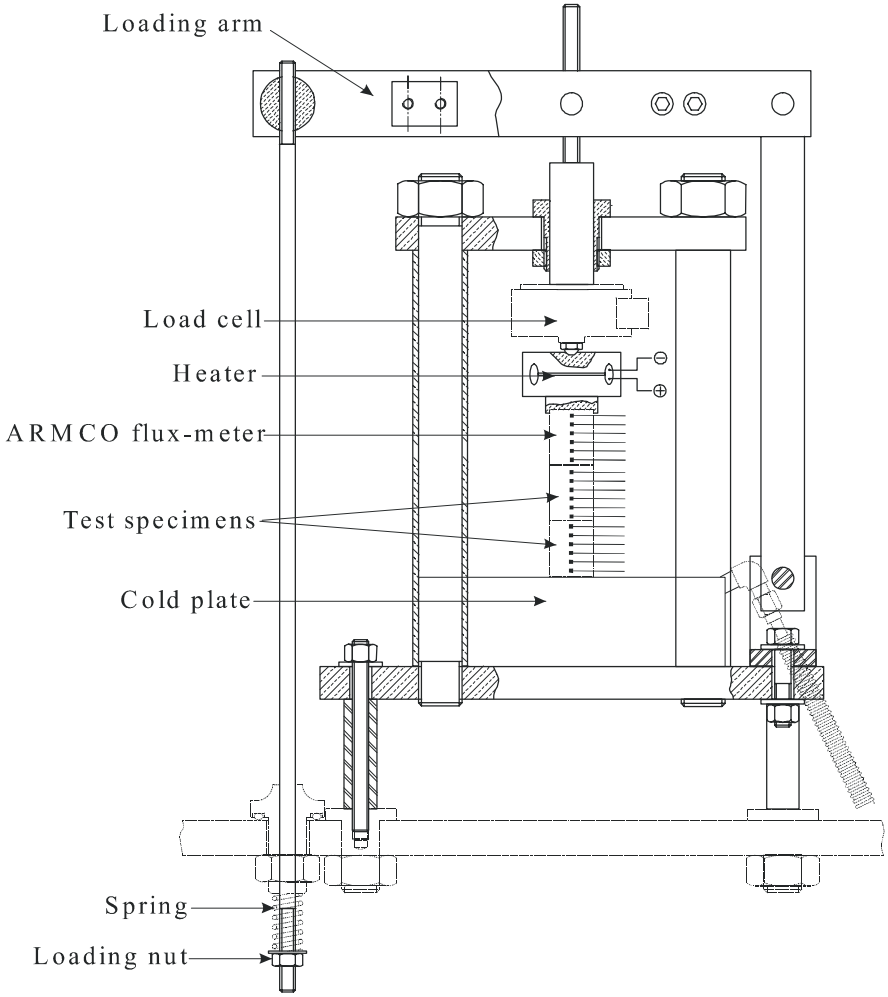

Figure 4.1 - Experimental set-up

4.3. Thermal conductivity measurements

The conductivities of the ARMCO Iron, Ni 200 and SS 304 are estimated using the following correlations:

$$k_{\mathrm{ARMCO}} = 75.0 - 0.070\,T \tag{4.1}$$

$$k_{\mathrm{Ni\,200}} = 90.2 - 0.184\,T \tag{4.2}$$

$$k_{\mathrm{SS\,304}} = 17.7 + 0.028\,T \tag{4.3}$$

The correlations are valid for temperatures T [°C] between 5 and 90°C. The correlation for the ARMCO Iron was obtained using the tabulated values available in Powell (1972). The ARMCO is a high purity iron (99.99% Fe) and has a very well known thermal conductivity ($\pm$ 2 % uncertainty). The correlations for the SS 304 and Ni 200 were obtained from conductivity tests. The conductivity tests employed basically the same experimental set-up described above. One of the SS 304 or the Ni 200 specimens was placed between two ARMCO flux-meters. The conductivity of the SS 304 or Ni 200 sample was computed by dividing the average heat flux of the two ARMCO flux-meters by the temperature distribution slope of the sample. This conductivity value was assigned to the sample mean temperature, which is the average of the six thermocouples. The heat flux through the flux-meters was obtained by multiplying the slope of temperature distribution by the conductivity of the ARMCO, evaluated at the mean temperature of the flux-meter (average of the six temperature readings). The conductivity tests were performed at various temperature levels of the SS 304 and the Ni 200 sample by varying the temperature of the cold plate. The SS 304 and Ni 200 conductivity correlations were then obtained by fitting a linear profile to the data points using the least square method. The RMS differences between the correlations and the actual measured values are 0.9% and 0.5% for SS 304 and Ni 200, respectively.

4.4. Specimen preparation

Six SS 304 and six Ni 200 cylinders of 25 mm diameter by 45 mm long were machined from the same stock bars. Six small holes (0.6 mm dia. by 1.5 mm deep) were drilled on the lateral surface of each specimen to accommodate the thermocouples. The specimen's contact surfaces were then ground flat. After that, the surfaces were lapped by means of a mechanical lapping machine in order to obtain maximum flatness. The mechanical lapping machine consists of a very flat horizontal 1 m dia. ceramic disc rotating at 60 rev/min. Over the ceramic disk is placed a 400 mm dia. steel disk which rotates at a higher speed than the ceramic disk. The steel disk is 40 mm thick and has six holes of approximately 25 mm

dia., which hold the samples being machined in vertical position over the ceramic disk. The axis of the ceramic disk and the axis of the steel disk are displaced. There is a small gap between the samples and the holes of the steel disk, and the gap is filled with lubricant oil so the samples can move loose. As the two disks rotate at different speeds, the samples rotate inside the hole as well and the surfaces of the samples that are in contact with the ceramic disk are ground randomly by the flat ceramic disk. After approximately 15 minutes, the surfaces are approximately isotropic rough and flat. The surfaces were further hand-lapped using 1200 grit sand-paper in order to obtain very smooth surfaces. The sand paper was placed over a very flat stone and the lapped surfaces were dragged manually over the sand paper. Lots of skill was needed during hand-lapping to avoid that the surface become spherical. The lapping process has shown to be a very critical task. In most of the times (5 out of 6 attempts) the surfaces presented flatness deviations beyond the limit admitted, which was approximately 0.5 μm. Surfaces presenting flatness deviations larger than that value were re-machined. The flatness deviations of the lapped surfaces were checked using a Krypton 86 monochromatic light source and an optical flat. The optical flat is placed over the surface and is exposed to a monochromatic light source. Interference fringes separated from each other by a distance which corresponds to 0.3 μm appear over the surface being measured. If the fringes are straight lines, the surface is flat and if the fringes present curvatures, the surface is wavy. By comparing the distance between two consecutive fringes with the deflection of the curved fringes, one can estimate the flatness deviation of the surface.

Three specimens of each metal were then bead blasted to different roughness levels and the other three specimens remained smooth. The desired roughness level of a bead blasted surface is easily obtained by setting an appropriate blasting pressure and/or choosing an appropriate bead size. The bead blasting process alters dramatically the roughness level of the lapped surfaces, but does not affect flatness. Therefore, at the end of the process, one obtains a nominally flat, isotropic rough surface, which is in accordance with the basic assumptions of the theoretical models.

4.5. Test procedure

The test pair, consisting of a flat lapped and a bead blasted specimen, was assembled inside the vacuum chamber with no load applied in the loading arm. Therefore, the first contact pressure level tested (15.8 kPa for SS 304 and 16.2 kPa for Ni 200) is determined by the dead weights of the upper specimen, flux-meter and electrical heater. The chamber was closed and vacuum was drawn. The electrical heater was turned “on” and the system was left

for at least 16 hours to achieve steady state. Every five seconds, the computer received the 18 thermocouple voltages, the load cell signal and the electrical heater voltage. A computer code then converted the thermocouple signals into temperature values and the load cell signal into contact pressure. The heat fluxes inside each specimen and the extrapolated temperature drop across the interface were computed from the temperature values. The thermal contact conductance was then computed by means of the following expression:

$$h_c = \frac{q}{\Delta T} \tag{4.4}$$

where q [W/m²] is the average of the heat fluxes of the two contacting specimens and ΔT [°C] is the temperature drop in the interface (according to Fig. 2.1). The heat flux values were first compared against the heat flux measured by the ARMCO flux-meter. The difference between the heat fluxes in each specimen and the ARMCO flux-meter was approximately 3%, in general. For very small heat fluxes the difference between heat fluxes in each sample could reach approximately 10%. This difference is a consequence of the thermocouple uncertainties rather than heat losses. When the heat flux is small, the temperature gradients inside the specimens are of the same order of magnitude of the thermocouple uncertainty. The heat flux crossing the test column was controlled manually so that the temperature drop at the interface was kept between 7 and 20°C, generally. The higher the heat flux, the larger the temperature drop at the interface between samples. In exceptional cases (very rough surfaces and very light contact pressure), the temperature drop reached 40°C.

The heat flux measured with the ARMCO flux-meter was assessed only in order to check the system; if the differences between the measured heat fluxes were too large, it was an indication that there was some problem in the system. For thermal contact conductance computation (Eq. 4.4), only the average of the heat fluxes of the test specimens was used.

The temperature drop ΔT [°C], appearing in Eq. (4.4), was computed by extrapolating the temperature profiles of each contacting specimen to the interface. For comparison between experiments and theory, the thermal conductivity of the contact is evaluated as the average of the two extrapolated temperatures.

The system was considered to be in steady state when the thermal contact conductance between the specimens did not vary more than 1% per 1 hour. For the lightest contact pressure tested, the steady state was achieved after 12 hours. As the contact pressure level was increased, the time required for the system to achieve steady state became smaller. For the maximum pressure tested, approximately 3000 kPa, the time required to achieve steady state was approximately one hour only.

As the contact pressure was increased between each pressure step, the power level of the electrical heater was also increased in order to maintain a reasonable temperature drop between the samples. This procedure was repeated for each contact pressure level tested. The pressure levels varied from 15.8 kPa (SS 304) or 16.2 kPa (Ni 200), to approximately 3000 kPa in both ascending and descending levels. Two loading/unloading cycles were measured for each pair in order to verify the appearance of the hysteresis loop, which indicates the deformation mode experienced by the contacting asperities. If the thermal contact conductance during the first unloading is larger than during the first loading, the deformation of asperities is plastic during first loading. On the other hand, if the same values are measured during both loading and unloading, it is an indication that elastic deformation took place.

The radiation heat transfer between the contacting samples is neglected, as already mentioned. The radiation conductance was estimated as two gray infinite parallel plates (form factor equal to 1) with emissivities equal to 0.2 and represented in general only 1% of the total conductance measured. Radiation heat losses from the testing column to the radiation shield are also neglected. The difference between the heat fluxes measured in the two contacting specimens was in general only 3%, as already mentioned. Included in this difference are heat losses and the uncertainty of heat flux measurement. This small value is an indication that practically the same amount of heat is crossing the two test samples, and therefore heat losses are small.

4.6. Micro-hardness measurements

The Vickers micro hardness test consists of pressing a square-based right diamond pyramid into a smooth flat metal surface under a static load. The load is kept static by at least 15 seconds. After that the load is released, the diagonals of the square impression left by the indenter are measured by means of a microscope. The Vickers hardness is computed as the load divided by the indentation area. The indentation area is computed using the average of the two measured diagonal lengths.

The procedure employed to characterize the micro-hardness variation near the surface consisted of measuring the Vickers micro-hardness for several different indentation loads, as mentioned before. One lapped specimen of each metal was used to characterize the surface micro-hardness. Indentation loads of 300, 200, 100, 50, 25 and 10 grams were used in this experimental program. The measured micro-hardness values H_v were then correlated to the respective diagonal lengths d_v according to Eq. (2.20). The Vickers micro-hardness correlation coefficients obtained using this procedure were c_1=10.6 GPa and c_2=-0.40 for SS

304 and c_1=4.3 GPa and c_2=-0.079 for Ni 200. Appendix 1 presents the collected micro-hardness data set that was used to compute the micro-hardness correlation coefficients.

As already mentioned, the theoretical models require the micro-hardness of the softer of the two contacting materials in order to predict the thermal contact conductance. Since it is necessary that the surface be smooth in order to measure the micro-hardness, it is not possible to measure accurately the micro-hardness of the bead blasted surfaces. However, it is expected that the lapped surface is the softer of the two, because the bead blasting process is expected to increase the work hardening of the surface. Therefore, the bead blasted surface should to be harder than the lapped surface.

4.7. Surface topography characterization

When predicting accurately thermal contact conductance, the surface topography characterization is perhaps the most critical task. The standards used in the design of equipments and procedures employed to measure surface roughness were developed for machined surface analysis. So, these standards were developed in order to assess primarily the roughness of the surface. In thermal contact conductance applications, the waviness is in most of the cases far more important than the roughness, as discussed by Clausing and Chao (1965) and others.

The standards that dictate the parameters to be used in roughness measurements were not developed based primarily on the problems encountered in thermal contact conductance. In order to extract important and accurate information from the surface topography, good sense and experience is necessary from the operator. The most employed type of equipment used for roughness measurements is the stylus profilometer. Is consists basically of a sharp probe (diamond pick) which traverses the surface to be measured. The vertical displacements of the probe are converted into an electric signal. Modern profilometers are connected to personal computers that analyze the signal and compute the roughness parameters. There are a large number of surface roughness parameters defined by the standards. From a thermal contact conductance point of view, only a few of them are relevant. Thomas (1982) makes an extensive review of the roughness measurement problem, describing equipments, definitions, parameters, problems, source of errors and applications. Only the issues encountered in thermal contact conductance problems will be shortly addressed here.

As the pick traverses the surface at a constant speed, the vertical position of the probe is registered at constant time intervals so that, at the end of the process, a string of surface heights at equidistant horizontal positions is obtained. The horizontal distance between two

consecutive readings is called *sampling interval*. An electric filtering (R-C circuits) is used to eliminate noise in output signal (high frequency waves). The computer (processing unit) receives the string of profile heights and perform a mechanical filtering on the obtained profile, and computes the roughness parameters (defined according to Eqs. 2.11 and 2.12) as:

$$m_0 = \frac{1}{N}\sum_{i=1}^{N} Z_i^{\,2} \tag{4.5}$$

$$m_2 = \frac{1}{N-1}\sum_{i=1}^{N-1}\left(\frac{Z_{i+1} - Z_i}{\Delta}\right)^2 \tag{4.6}$$

where the Z_i [μm] are the height readings measured from the mean line of the profile, N is the total number of profile heights measured, and Δ [μm] is the sampling interval.

The mechanical filter, mentioned above, is usually known as *cut off* length. The objective of this filter is to eliminate waviness from the measured profile. The filtering of profile is the critical process in obtaining the relevant surface roughness features. The unfiltered measured profile is composed by an infinite superposition of waves of different amplitudes and wavelengths. If one plots the amplitudes versus the wavelengths of the signal one obtains a continuous spectrum (Thomas, 1982). It is impossible to define where exactly in the spectrum the roughness and the waviness are confined. Employing different filters, one can eliminate waves above a certain lengths from the signal. However, there are no standards defining clearly which wavelength should be eliminated for thermal contact conductance applications.

The cut off filtering consists of dividing the measured (unfiltered) profile into 5 or 7 regions, depending on the equipment, of the same length. The first and the last cut off lengths are generally discarded by the equipment to eliminate the effect of acceleration and deceleration of the probe. The processing unit then finds the mean lines of each cut off length, which are different from mean line of the unfiltered profile. The computation of the roughness parameters is based on the new mean lines of the cut off lengths. Figure 4.2 shows how the cut off length affect the final profile which is used to compute the roughness parameters. If a too small cut off length is chosen, some waviness that is relevant in the contact mechanics is eliminated. In this case, the computed RMS roughness (σ) is underestimated and, as a consequence, thermal contact conductance will be overestimated. On the other hand, if the chosen cut off length is too large, long wavelength waviness that are not important in contact mechanics are incorporated into the measurement profile. As a consequence, the computed roughness is overestimated, and thermal contact conductance is underestimated.

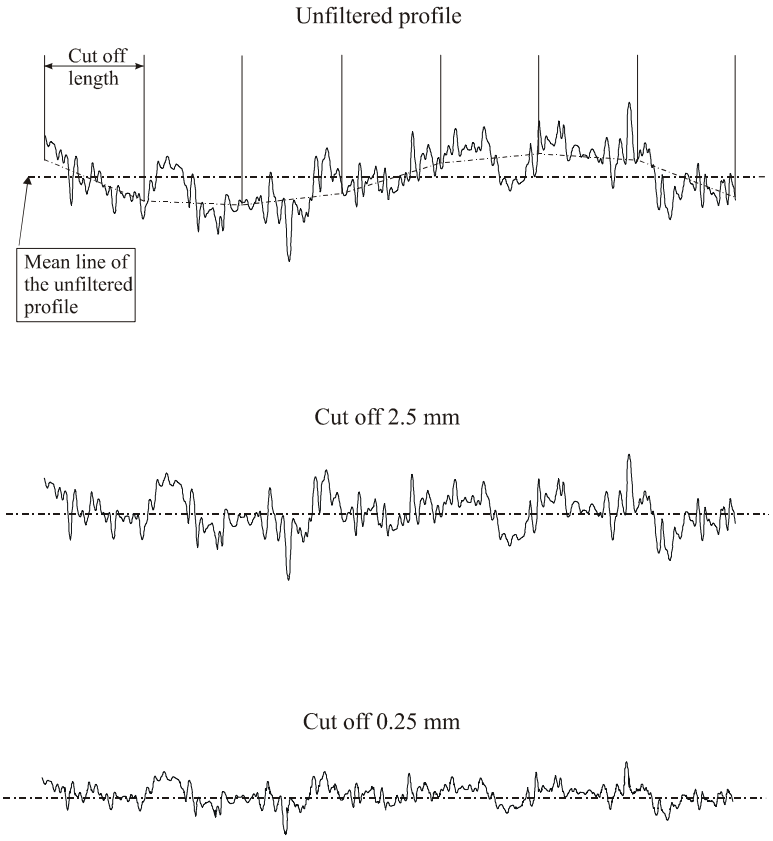

Figure 4.2 – Effect of the cut off length on the measurement profile

The ANSI B46.1 standard specifies the cut off lengths to be used: 0.08, 0.25, 0.8, 2.5 and 8 mm. The specification of a 0.8 mm cut off length is preferred for most applications. However, the standard also mentions that "in some cases such as surfaces in which actual contact area with a mating surface is important, the largest convenient cut off length will be used." On the other hand, the unfiltered profile, which can be interpreted as a cut off length equal to the total length of the measured profile, can not be used either because long wavelength waves are not critical in contact mechanics due to elastic deformation of the mean surface plane under contact load. Based on these considerations, a cut off length of 2.5 mm was used in this work. Furthermore, the difference between the results obtained using the cut off lengths of 2.5 and 8 mm was generally very small, indicating that the amplitude of the wavelengths between 2.5 and 8 mm is very small and also indicating that the samples were sufficiently flat.

Five non-parallel profiles were taken randomly from each bead blasted surface used in the experimental study. The sample roughness was estimated as the average of the five measurements. The lapped surfaces were prepared at the same time and presented practically the same roughness level. Appendix 1 presents the complete roughness data set.

4.8. Uncertainty analysis

The uncertainty in thermal contact conductance measurement varies according to the contact pressure level. At low loads, the uncertainty of thermal contact conductance measurements is larger than at high contact loads because of the uncertainty of heat flux measurement. The uncertainty of heat flux measurement is larger at low loads because the slope of the temperature distribution is small (heat flux is small). Table 4.1 shows a summary of the uncertainties of this experimental study. A detailed experimental uncertainty analysis is presented in Appendix 2.

Table 4.1 – Experimental uncertainty summary

	Uncertainty			
	SS 304		Ni 200	
	Lightest Load	Highest Load	Lightest Load	Highest Load
Thermal Conductivity	5.8 %		8.1 %	
Temperature Drop	0.25 %	1.25 %	0.25 %	1.25 %
Heat Flux	14.7 %	4.1 %	15.3 %	5.7 %
Thermal Contact Conductance	15 %	4 %	16 %	6 %
Contact Load	1 %			

4.9. Summary

This chapter described the experimental study employed to measure thermal contact conductance between nominally flat, rough surfaces. The experimental set-up, preparation method of the test specimens, micro-hardness, surface topography and thermal conductivity measurements as well as the test procedure were described in details.

CHAPTER 5
RESULTS AND DISCUSSION

5.1. Introduction

In this chapter, the TG thermal contact conductance models developed in Chapter 3 and the existing models (fully Gaussian) reviewed in Chapter 2 are compared against experimental data from Hegazy (1985) as well as against the thermal contact conductance data collected during the experimental program described in the previous chapter. A discussion on the truncation level of bead blasted SS 304 and Ni 200 is then made based on the comparison between theory and experiments. The chapter also presents a study of the topography of surfaces generated by bead blasting, in order to analyze the surface height distribution truncation levels. A comparative study between the z_{trunc} values obtained from the thermal tests and the values obtained from the bead blasting study is then presented.

5.2. Comparison between the models and existing experimental data

In order to illustrate the advance of the TG model in relation to the fully Gaussian model, being used until now, these two models are compared against existing thermal contact conductance experimental data obtained from Hegazy (1985). This researcher conducted an extensive experimental program to collect thermal contact conductance data between conforming rough surfaces during the first loading. One of the contacting surfaces was lapped and the other was bead blasted. Four metals were tested: SS 304, Ni 200, Zr-4 and Zr-Nb alloy. At least four different roughness levels of each metal were tested. Figures 5.1 to 5.3 present the experimental data and the comparison with the fully Gaussian and the Truncated Gaussian thermal contact conductance models.

The TG model is plotted in these graphs as a set of curves for different truncation levels z_{trunc}. Since Hegazy (1985) was not aware of the truncation problem, he did not provide information about the surface height distribution truncation level of his test specimens. The lowest curve of each graph (straight line) is for $z_{trunc} \rightarrow +\infty$, which is equivalent to the fully Gaussian model (CMY, 1969). The differences between the TG model and the fully Gaussian model are more evident at low contact pressures (small P/H_c). The smaller the value of z_{trunc}, (i.e., the larger the truncated portion of the surface heights probability density function), the larger is the deviation of the TG model from the fully Gaussian model. For $z_{trunc}>5$, the TG model to coincide with the fully Gaussian model, which means that surfaces presenting

truncation levels above approximately 5 behave as fully Gaussian surfaces, even under the lightest contact pressure. The curves for the TG model for $\lambda_{trunc}<5$ are concave: they lie above the fully Gaussian model at low contact pressures and tend to the fully Gaussian model as the contact pressure increases.

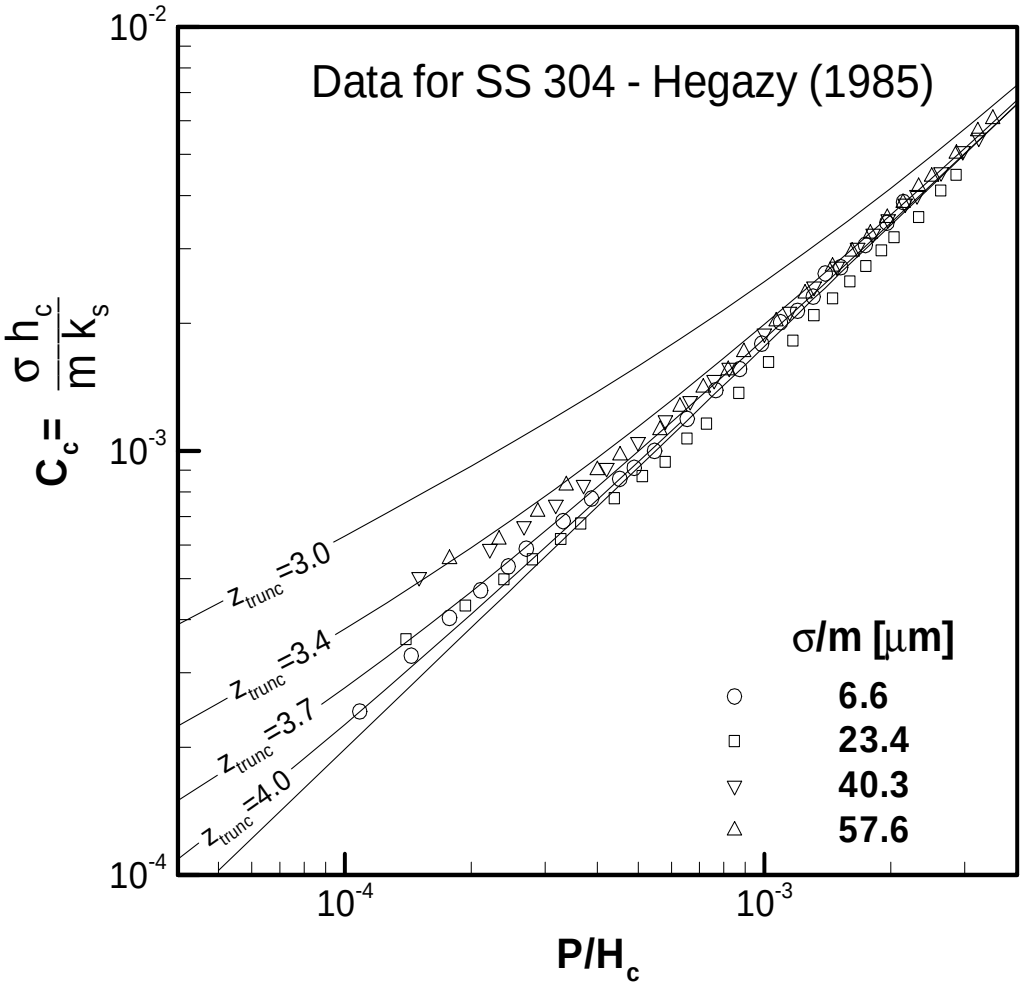

Figure 5.1 – Comparison between the TG model and SS 304 data from Hegazy (1985)

The TG model seems to predict the experimental data trend very well for all metals and all the roughness levels tested by Hegazy (1985). The experimental data lie between the curve of $z_{trunc}=3.4$ and the curve of the fully Gaussian Model ($z_{trunc}=+\infty$). From these graphs, one can notice that the rougher the surfaces (larger σ/m), the more evident is the truncation (smaller z_{trunc}). It is believed that the truncation of the asperity height distribution is due to the inability of the bead blasting process to generate asperities beyond some height level. The comparison between the TG model and the experimental data from Hegazy (1985) suggests

that the rougher the surface, the more difficult is to generate high asperities, i. e., smaller is z_{trunc}.

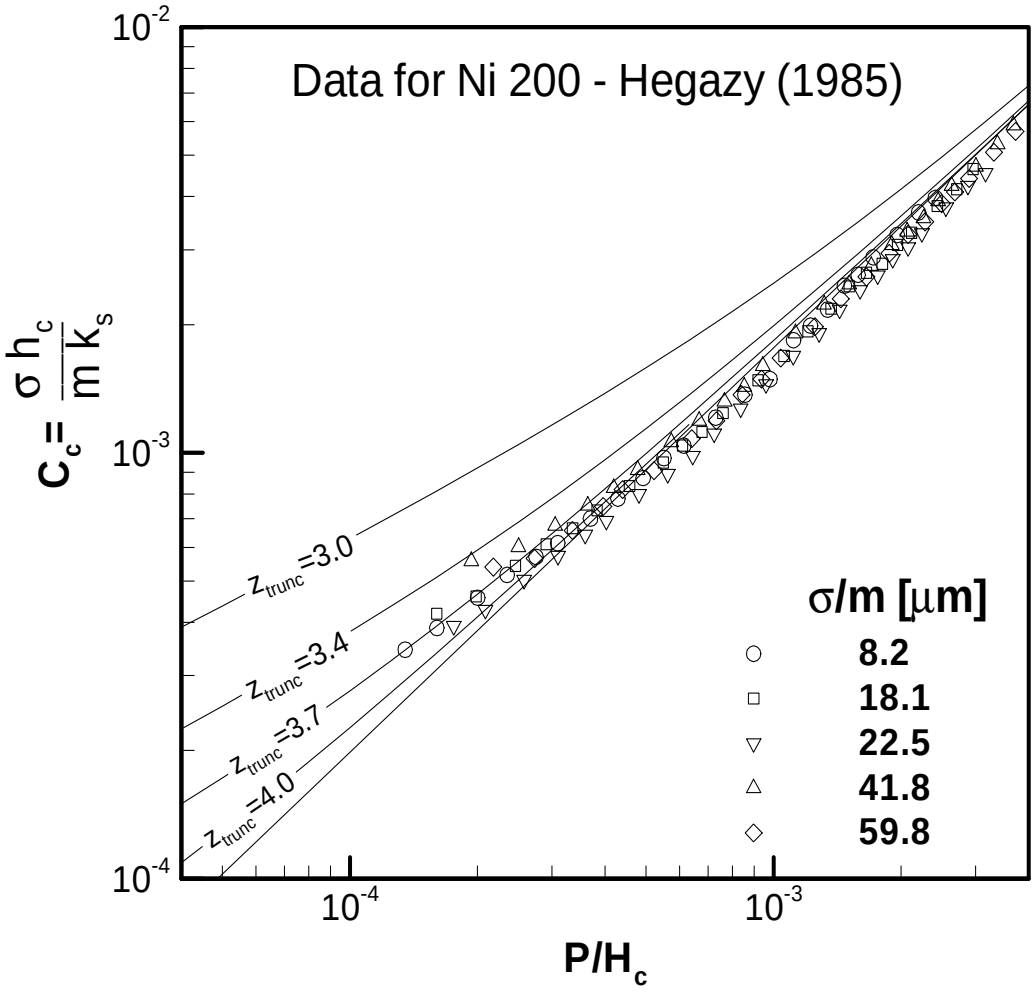

Figure 5.2 – Comparison between the TG model and Ni 200 data from Hegazy (1985)

The comparison between the models and Hegazy's (1985) data show that the TG model predicts the trend of data points very well at low contact pressures. The models are now compared against the thermal contact conductance data collected in the experimental study described in this work. The surface topography of the specimens tested was carefully examined in order to extract information about the truncation of the surface height distribution, which was not done by Hegazy (1985) because he was not focused on the surface topography and did not addressed this problem. He tried to explain the unexpected behavior of thermal contact conductance at low contact pressures as being a consequence of thermal strain and flatness deviations of the test specimens, but did not propose any model to predict

this phenomenon. He also clearly stated that this explanation was not definitive and further work was needed to clarify this issue. This problem seems to be better explained here in the light of the new Truncated Gaussian geometric model.

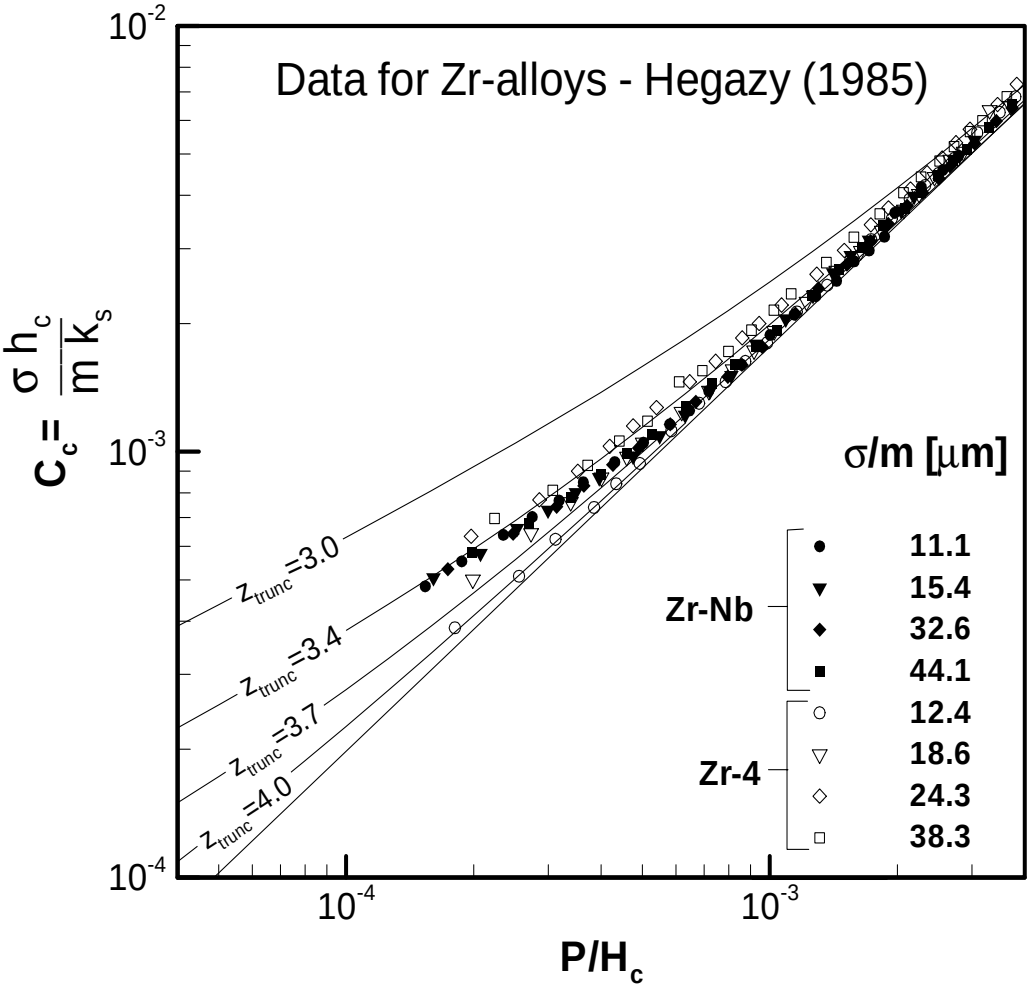

Figure 5.3 – Comparison between the TG model and Zr-alloys data from Hegazy (1985)

5.3. Comparison between the models and the experimental data collected in this work

In order to make the presentation of the test results easier, the tests are named here with a letter followed by a number: S1, S2, S3, N1, N2, and N3. The letter refers to the metal, "S" for SS 304 and "N" for Nickel, and the numbers are related to the roughness of the pair tested: the rougher the pair, the larger the number, i. e., the N3 test specimens have total roughness σ larger than the N2 test and so on. However, that does not mean that the S1 and the N1 tests have the same roughness level. They are only the smoothest pairs of each metal.

5.3.1. SS 304 results

The mechanical and thermal properties and roughness parameters of the test specimens as well as the range of other test parameters for the SS 304 tests are presented in Table 5.1. The σ, m and σ/m values presented in this table are the average of the values obtained from the five profiles taken from each surface. The ratio σ/m is commonly used as a measure of the roughness level of the surface; it is a better representation of the roughness level than σ alone, because σ/m appear explicitly in the theoretical models. The total roughness of the pairs, computed according to Eqs. (2.16) and (2.17), were determined basically by the roughness of the bead blasted surfaces, because the roughness of the lapped surface is very small compared to the bead blasted surfaces. The c_1 and c_2 values presented in Table 5.1 were obtained from five indentations for each load. The average of the ten diagonal lengths (two diagonals for each indentation) and the average of the five hardness values for each indentation were used to obtain the correlation coefficients according to Eq. (2.20). The individual values of the diagonal lengths and hardness values, as well as the roughness measurements are presented in Appendix 1. The range of measured apparent contact pressures P, mean interface temperature T_m, temperature drop ΔT and heat flux at the interface q, as well as the thermal conductivity at the interface k, computed as a function of T_m according to Eq. (4.3), are also presented in Table 5.1. Appendix 3 presents the entire SS 304 thermal contact conductance experimental data set collected during the experimental program. The values of z_{trunc} presented in Table 5.1 were obtained by fitting the correlation of the TG thermal contact conductance model for plastic deformation during the first loading (Eqs. 3.23 and 3.24) to the experimental data points. Figure 5.4 illustrates the procedure employed to obtain z_{trunc}. For the case presented in Fig. 5.4 (test S3), the TG model with a value of z_{trunc}=3.5 gives a line that is parallel to the data points, therefore z_{trunc}=3.5 is adopted as the truncation level in this case. The data points do not have to lie exactly over the best line. Instead, the best line is the one which is parallel to the data points. This aspect is important in order to avoid that a systematic errors, such as roughness or hardness measurement errors, be masked by the process of finding the best z_{trunc}. As discussed extensively by Milanez et al. (2002) and it will be addressed later in this chapter, this is believed to be the most accurate method to estimate z_{trunc}.

Table 5.1 – Mechanical, thermal, geometrical and other parameters of the SS 304 tests

test	S1	S2	S3
σ/m [μm] (total)	17.7	26.2	40.0
σ [μm] (bead blasted)	0.7	1.3	3.9
m (bead blasted)	0.036	0.047	0.098
σ [μm] (lapped)	0.12	0.12	0.12
m (lapped)	0.022	0.022	0.022
total flatness dev. [μm]	0.9	0.8	0.7
c_1 [GPa]	10.67	10.67	10.67
c_2	-0.37	-0.37	-0.37
z_{trunc}	4.1	3.8	3.5
k [W/m·K]	18.4 to 19.5	18.3 to 19.4	18.2 to 19.2
P [kPa]	15.8 to 2,768	15.8 to 2,720	15.8 to 3,450
H_c [GPa]	6.2 to 3.8	6.6 to 3.3	6.5 to 2.7
T_m [°C]	23 to 65	20 to 63	19 to 54
ΔT [°C]	5.5 to 48	7 to 85	9 to 77
q [W/m^2]	290 to 19,000	365 to 12,000	280 to 7,980

Figure 5.5 shows a plot of h_c against P for the data obtained from test S1, where the smoothest of the SS 304 pairs was tested. The experimental data, as well as the theoretical models for first loading (plastic deformation) and unloading are presented. For first-loading, the CMY plastic model with the fully Gaussian geometry model is presented as a dashed line and the CMY plastic model with the TG geometry model is presented as a continuous line. For unloading, the Mikic (1971) fully Gaussian model is presented as a dotted line and the Mikic (1971) model adapted according to the TG geometry model is presented as a dash-dotted line. The black squares are the first-loading experimental data, while the white squares are the first-unloading data. The black circles are the second-loading data and the white circles are the second-unloading data.

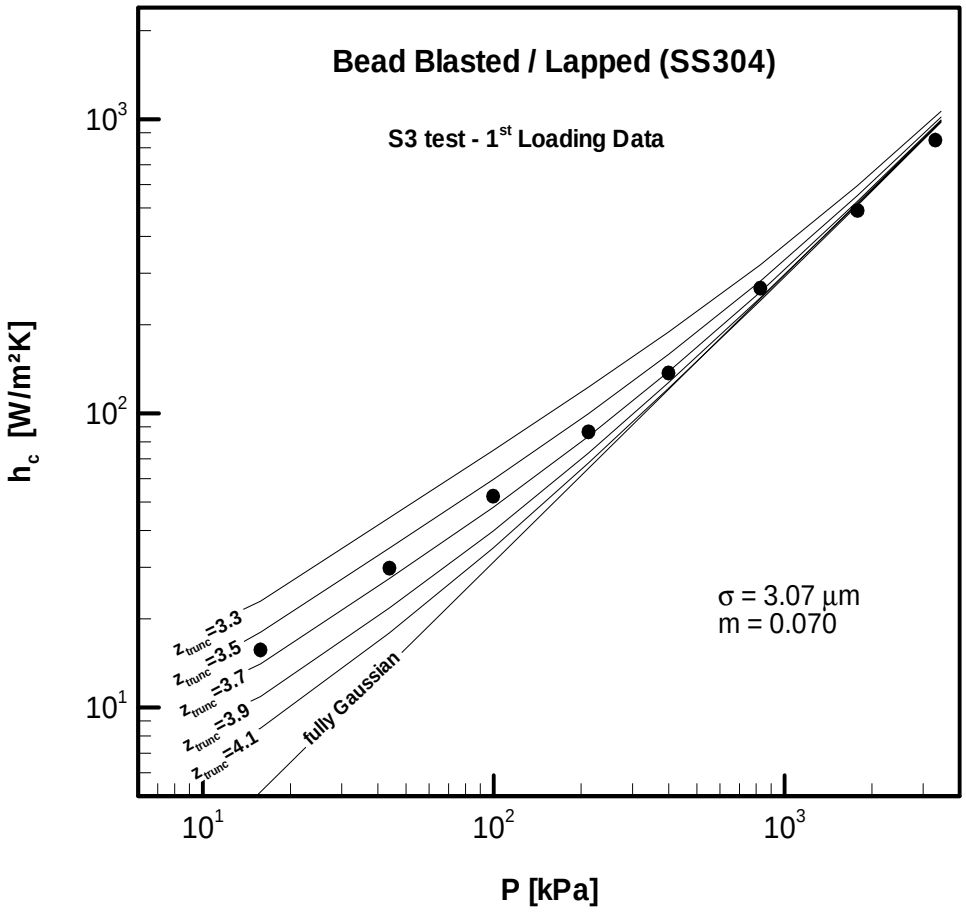

Figure 5.4 – First Loading data from S3 test and comparison with the TG model for various values of z_{trunc}

The first-unloading data points lie above the first-loading data points, which characterizes the hysteresis effect of thermal contact conductance. That is an indication that plastic deformation took place during the first loading. The fully Gaussian model underpredicts the first-loading data at light loads. As the contact pressure increases, the model tends to the measured values, except for the three data points collected at the highest contact pressure levels. The TG model with z_{trunc}= 4.1 predicts the data points over the entire range very well, except the three highest contact pressure points. These three points presented an unexpected behavior in comparison to the trend of the other first-loading data points; they suddenly had an increase in thermal contact conductance. It is believed that this odd behavior was due to the inexperience in preparing the test samples and in conducting the experiments, as it will be discussed now. The S1 was the first pair prepared and tested. The total flatness

deviation of this test pair (0.9 μm) was the largest of all pairs tested, while the roughness was the smallest of all. The ratio between waviness and roughness for the S1 pair was then the largest of all pairs tested. The waviness might have played an important role in this unexpected increase of contact conductance of the last three data points during first loading. Beyond approximately 2000 kPa, the apparent contact pressure might have been sufficiently high to suppress the surface waviness by elastic deformation of the mean plane, increasing the contact conductance. As it will be seen, this problem was no longer detected during the other tests, which employed test pairs with smaller flatness deviations and larger roughness.

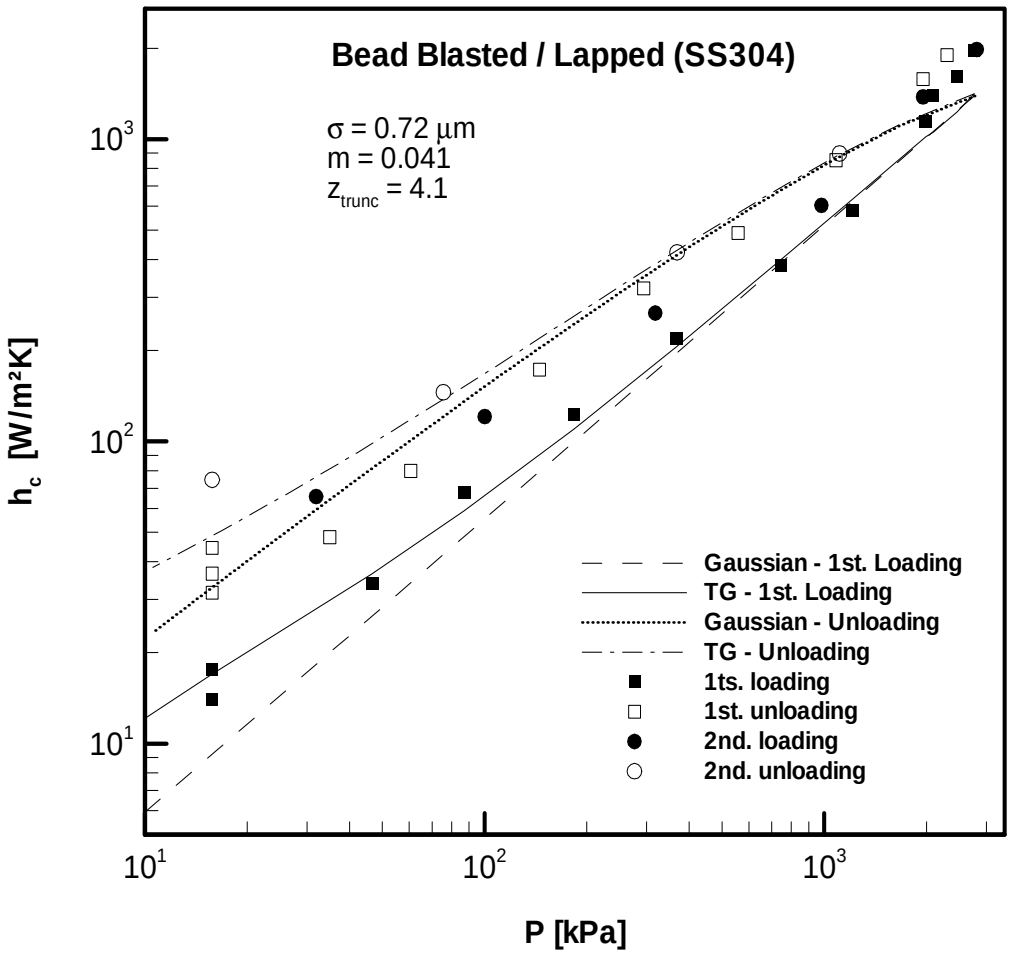

Figure 5.5 – Results from test S1

The first two points of the first loading illustrates how critical it is to measure thermal contact conductance at such low contact pressure levels as tested here. The two points were collected at exactly the same contact pressure. Two values of thermal contact conductance

were obtained: 17.5 and 14.0 W/m^{2}K. The first was obtained with a heat flux of 1268 W/m^2, which generated a temperature drop of 72.2°C, and the second was obtained with a heat flux of 290 W/m^2, which generated a temperature drop of 20.7 °C. The larger the heat flux, the larger the thermal contact conductance for the same contact pressure. This behavior was also detected in the last three points of the first unloading: 31.6 W/m^{2}K, 36.5 W/m^{2}K and 44.4 W/m^{2}K under heat fluxes of 990 W/m^2, 1450 W/m^2 and 2310 W/m^2, respectively. The influence of the heat flux intensity on thermal contact conductance is not predicted by the existing theoretical models. It is believed that the higher the heat flux, the higher are thermal distortions of the contacting surfaces due to higher temperature gradients near the contact spots. These thermal distortions could alter the size of the contact spots, affecting thermal contact conductance. From this observation, it was decided to maintain the interface temperature drop as constant as possible and approximately between 10 and 20°C for the remaining tests, although this was found to be a difficult task as well. When a new contact pressure was set, the power of the electrical heater had to be increased in order to maintain an approximately constant temperature drop across the interface. The temperature of the cold plate had to be lowered in order to maintain the mean temperature level of the interface constant as well (between 20 and 30°C). However, the system could take up to 10 hours to achieve steady state, what means that, as the temperature distribution of the testing column varied with time, the contact pressure, the mean temperature level and the temperature drop varied as well, so it was practically impossible to predict exactly where these parameters would get to when steady state was achieved. Experience is needed to keep these parameters within the desired range of values. The results of test S1 could be discarded and a new test pair could be prepared and tested, which could take considerable time (almost 1 month). Instead, it was decided to keep the test S1 results to show the improvement of the trend of data points from test S1 to S2 and to S3 in order to illustrate the importance of experience in preparing test specimens and conducting thermal contact conductance measurements at such low contact pressure levels as those reached in this experimental study.

Returning to Fig. 5.5, the second-loading data points lie more close to the first-unloading data points than during the first-loading data points, indicating that the deformation of asperities is more elastic than plastic during the second loading. Also the second-unloading data points lie more or less on the same line as the second-loading, except for the last data point collected (second unloading, 15.8 kPa of contact pressure). The hysteresis loop is not as evident during the second-loading/unloading cycle as it was during the first cycle.

Both unloading models (fully Gaussian and TG) predicted the experimental data fairly well in the contact pressure range between 300 and 2000 kPa. For $P < 300$ kPa, the fully Gaussian unloading model predicted the data better than the TG unloading model, although the TG unloading model predicted the trend of data points better than the fully Gaussian unloading model. The larger scattering of data points for $P < 100$ kPa is also believed to be due to the relative inexperience in conducting the S1 test and the difficulty in performing the test at very low contact pressures, as discussed previously.

The results from test S2 are shown in Fig. 5.6. As observed in test S1, the first-unloading data points of test S2 lie above the first-loading data. Once more the appearance of the hysteresis loop indicates the occurrence of plastic deformation during the first loading. The second-unloading data points lie over the same line as the first-unloading data points, indicating that the deformation is completely elastic during this cycle. This is the behavior expected according to the existing theory (Mikic, 1971). The fully Gaussian first-loading model underpredicts the experiments at low contact pressures, similarly to test S1 and also extensively reported in the literature. As the pressure increases, the model predicts the experiments very well. The TG model predicts the first-loading points over the entire range of contact pressure better than the fully Gaussian model, although the curvature of the line formed by the first-loading data points is larger than the curvature of the TG model.

Both the unloading models predicted the unloading/re-loading data points very well for $P > 300$ kPa. At lower contact pressures, the fully Gaussian unloading model predicted the experiments better than the TG unloading model, although the TG unloading model predicted the trend of the data points better. The TG unloading model overpredicts the experiments, while the fully Gaussian unloading model underpredicts the experiments at the lowest contact pressure. Similarly to test S1, different thermal contact conductance values were obtained at the lowest contact pressure for different heat fluxes during Test S2, although the differences in test 2 were smaller than in test 1. Appendix 3 presents the complete thermal contact conductance experimental data of all tests.

Figure 5.7 shows the results of test S3, which had the roughest of the SS 304 pairs and was the last pair tested. In general, the results of the S3 test are similar to the other tests presented previously. The hysteresis loop is evident in the first-loading/unloading cycle, indicating the appearance of plastic deformation. The hysteresis effect is negligible during the first-unloading and second loading/unloading cycle, indicating the appearance of elastic deformation. The fully Gaussian first-loading model underpredicts the experimental data at low contact pressures. As the contact pressure increases, the model agrees with the data

points. The TG model with z_{trunc}=3.5 predicts the experiments well for the entire range of contact pressures for the first loading data.

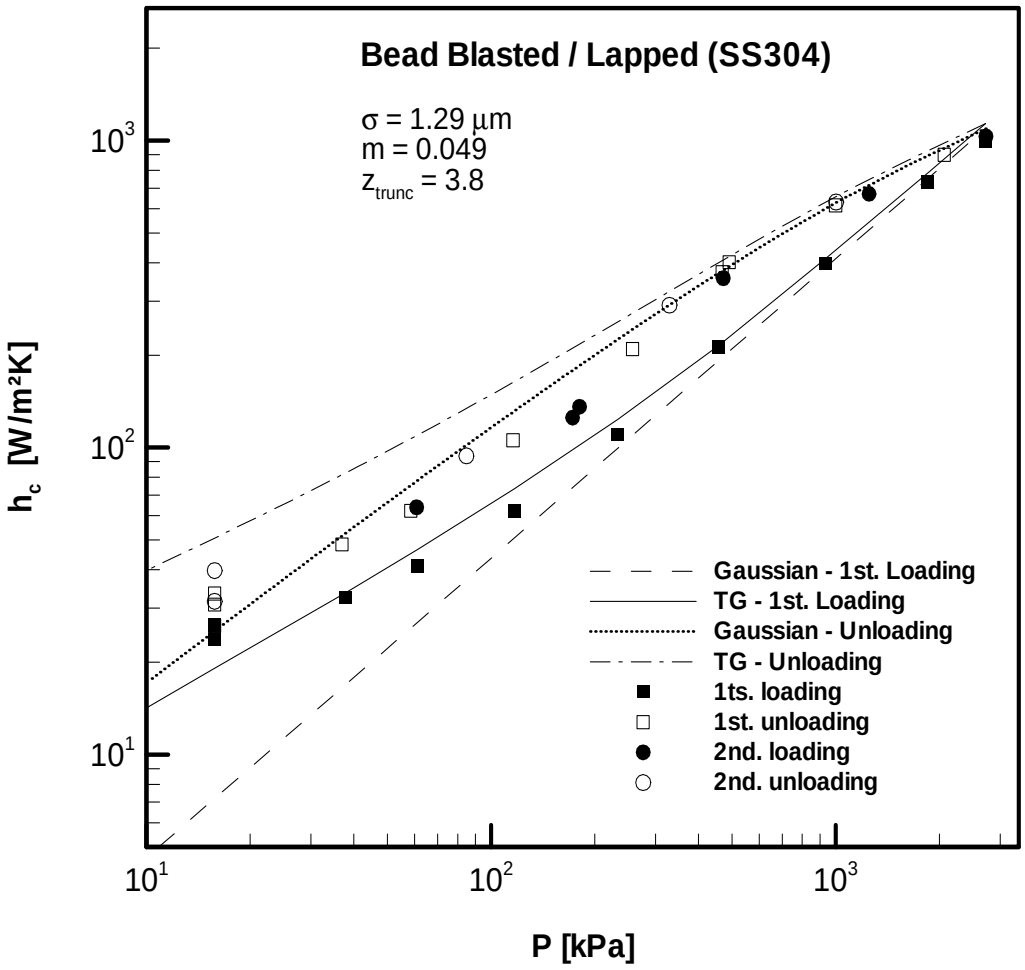

Figure 5.6 – Results from test S2

The TG first-loading model is slightly displaced above the data points in test S3. The difference could be due to the inaccuracy of the roughness measurements. As discussed in the last chapter, the cut off length used in roughness measurement affects the obtained roughness value. Since this is the rougher of the SS 304 pairs tested, the magnitude of the roughness relative to the waviness in test S3 is the smaller of the SS 304 tests. The cut off length used (2.5 mm) could be ideal for smoother surfaces, but for rougher surfaces, this cut off length could be filtering out part of the roughness, making the measured roughness to be underpredicted. As a consequence, the theory slightly overpredicts the experiments.

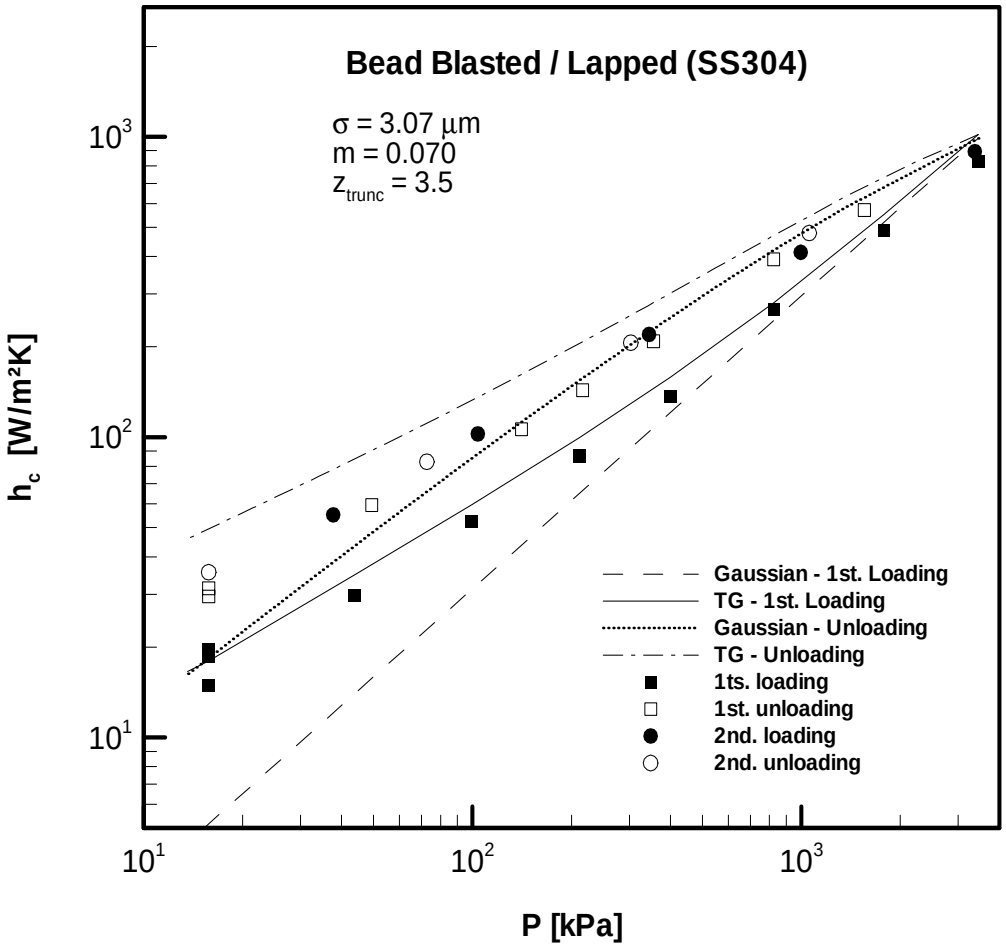

Figure 5.7 – Results from test S3

As noticed in tests S1 and S2, the fully Gaussian unloading model predicted the experiments better than the TG unloading model in test S3. However, the TG model predicts the trend of data points better than the fully Gaussian model. At light contact pressures, the TG unloading model overpredicts the unloading/re-loading data, while the fully Gaussian model underpredicts the data at low contact pressures.

5.3.2 Ni 200 results

The mechanical and thermal properties and roughness parameters of the test specimens as well as the range of other test parameters of the Ni 200 tests are presented in Table 5.2. Similarly to the SS 304 tests, five roughness profiles were taken from each bead blasted

surface tested. The c_1 and c_2 values presented in Table 5.2 were obtained from 5 indentations for each load. Appendix 1 presents the entire hardness and roughness data sets. The values of z_{trunc} presented in Table 5.2 were obtained by fitting the correlation of TG thermal contact conductance model for plastic deformation during the first loading (Eqs. 3.23 and 3.24) to the first-loading data sets. Appendix 3 presents the Ni 200 thermal contact conductance experimental data collected during the experimental study.

Table 5.2 – Mechanical, thermal, geometrical and other parameters of the Ni 200 tests

test	N1	N2	N3
σ/m [μm] (total)	23.0	27.0	48.0
σ [μm] (bead blasted)	1.7	3.0	4.2
m (bead blasted)	0.074	0.11	0.086
σ [μm] (lapped)	0.10	0.10	0.10
m (lapped)	0.017	0.017	0.017
total flatness dev. [μm]	0.6	0.6	0.6
c_1 [GPa]	4.33	4.33	4.33
c_2	-0.079	-0.079	-0.079
z_{trunc}	4.2	4.2	3.9
k [W/m·K]	84.2 to 87.3	84.8 to 87.3	85.8 to 87.0
P [kPa]	16.2 to 1,970	16.2 to 1,780	16.2 to 2,080
H_c [GPa]	3.7 to 3.4	3.6 to 3.4	3.6 to 3.2
T_m [°C]	16 to 33	16 to 30	17.5 to 24
ΔT [°C]	9 to 21	9 to 19	9 to 19
q [W/m^2]	1,200 to 35,5000	1,200 to 41,200	280 to 7,980

Figure 5.8 shows the results of test N1, which employed the smoothest of all the Ni 200 pairs tested. In general, the results are similar to the SS 304 tests presented previously. The hysteresis loop is evident in the first-loading/unloading cycle, indicating the appearance of plastic deformation. The hysteresis effect is negligible during the first-unloading and second loading/unloading cycle, indicating the appearance of elastic deformation. The fully Gaussian first-loading model underpredicts the experimental data at low contact pressures. As the contact pressure increases, the model agrees with the data points. The TG model with

z_{trunc}=4.2 predicts the first-loading data well for the entire range of contact pressures. The unloading models predicted the unloading/re-loading data points very well for P > 500kPa. At lower contact pressures, the models overpredicted the experiments, especially the TG unloading model. Differently from the SS 304 tests, the fully Gaussian unloading model predicted the trend of the unloading/re-loading data better than the TG model for test N1. It is believed that some odd phenomena or experimental error, that could not be identified, took place in measuring the unloading/re-loading data points of test N1 at low contact pressures. The N1 was the only test that presented this atypical behavior. All the SS 304 tests, as presented before, and the N2 and N3 tests, as it will be seen later, had the trend of unloading/re-loading data points better predicted by the TG unloading model.

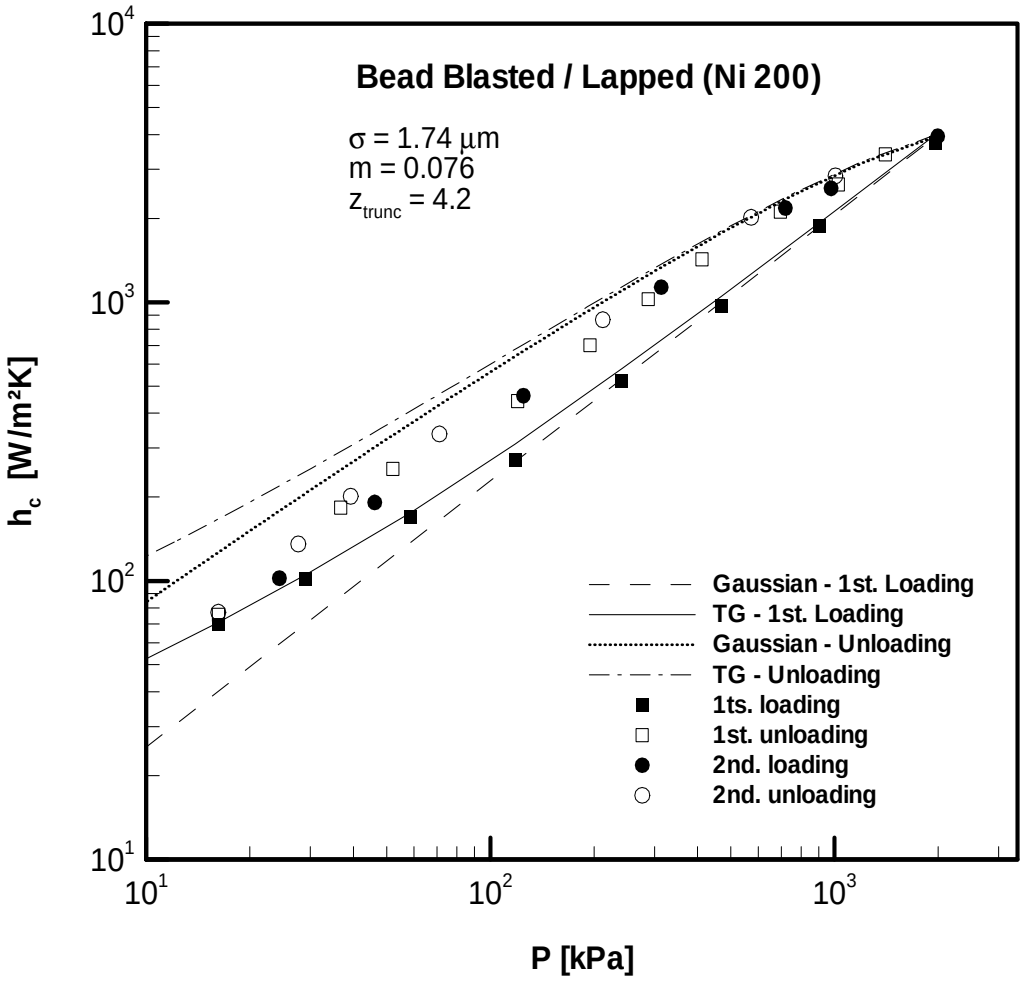

Figure 5.8 – Results from test N1

The results from test N2 are shown in Fig. 5.9. As observed in the previous tests, the first-unloading data points of test N2 lie above the first-loading data. The appearance of the hysteresis loop indicated the occurrence of plastic deformation during the first loading. The second-loading/unloading data points lie over the same line as the first-unloading data points, indicating that the deformation is completely elastic during this time. The fully Gaussian first-loading model under predicted the experiments at low contact pressures. As the contact pressure increases, the model predicts the experiments very well. The TG model with z_{trunc}=4.2 predicts the first-loading points over the entire range of contact pressure much better than the fully Gaussian model. Both the unloading models predicted the unloading/re-loading data points very well for contact pressures near the maximum contact pressure, as noticed in all other tests. At low loads, both the TG and the fully Gaussian models failed to predict the data accurately, although the TG model predicted the trend of data points better.

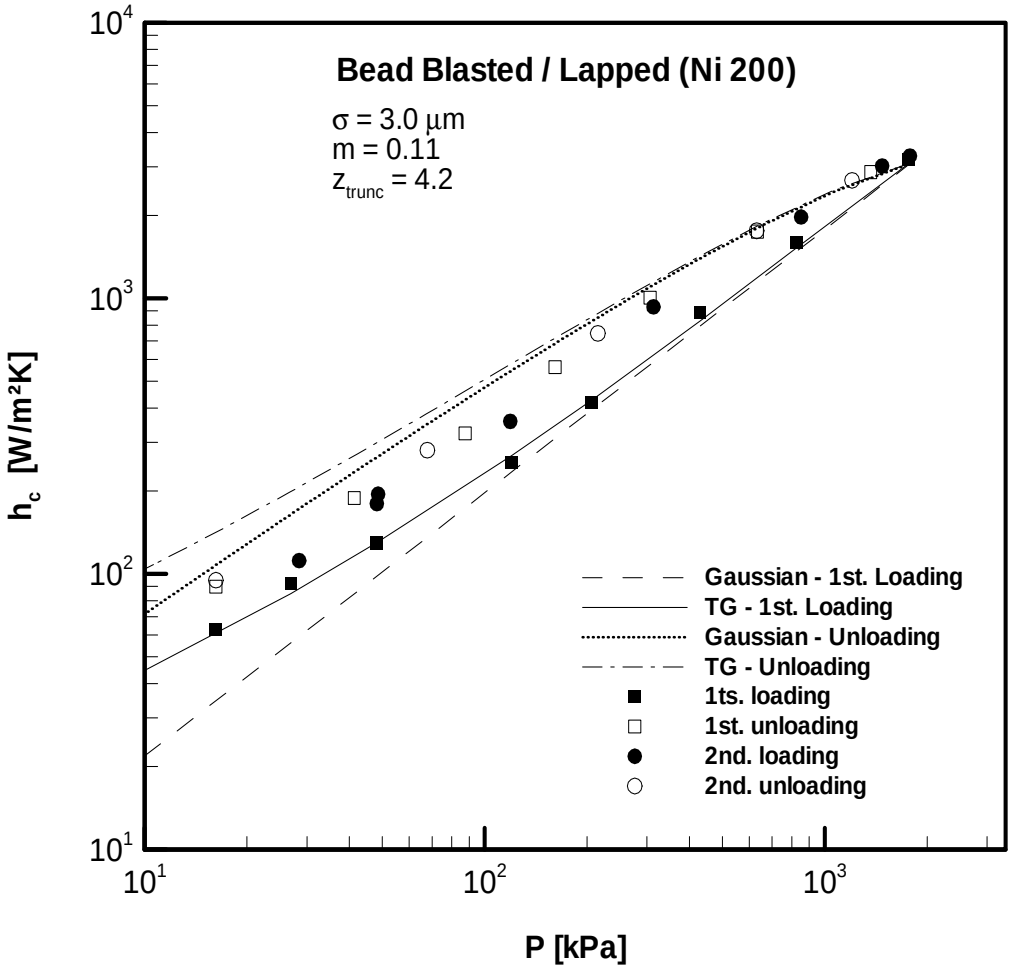

Figure 5.9 – Results from test N2

Figure 5.10 shows the results of test N3, the last test. The results were again similar to the other tests presented previously. The hysteresis loop is evident in the first-loading/unloading cycle, indicating the appearance of plastic deformation. The hysteresis effect is negligible during the first-unloading and second lading/unloading cycle, indicating the appearance of elastic deformation. The fully Gaussian first-loading model under predicted the experimental data at low contact pressures. As the contact pressure increases, the model agreed with the data points well. The TG model with z_{trunc}=3.9 predicted the first-loading experiments well for the entire range of contact pressures. The basic difference between test N3 and the other tests presented previously is that in test N3, the TG unloading model predicted the unloading/re-loading data fairly well, while the fully Gaussian model underpredicted the experimental data.

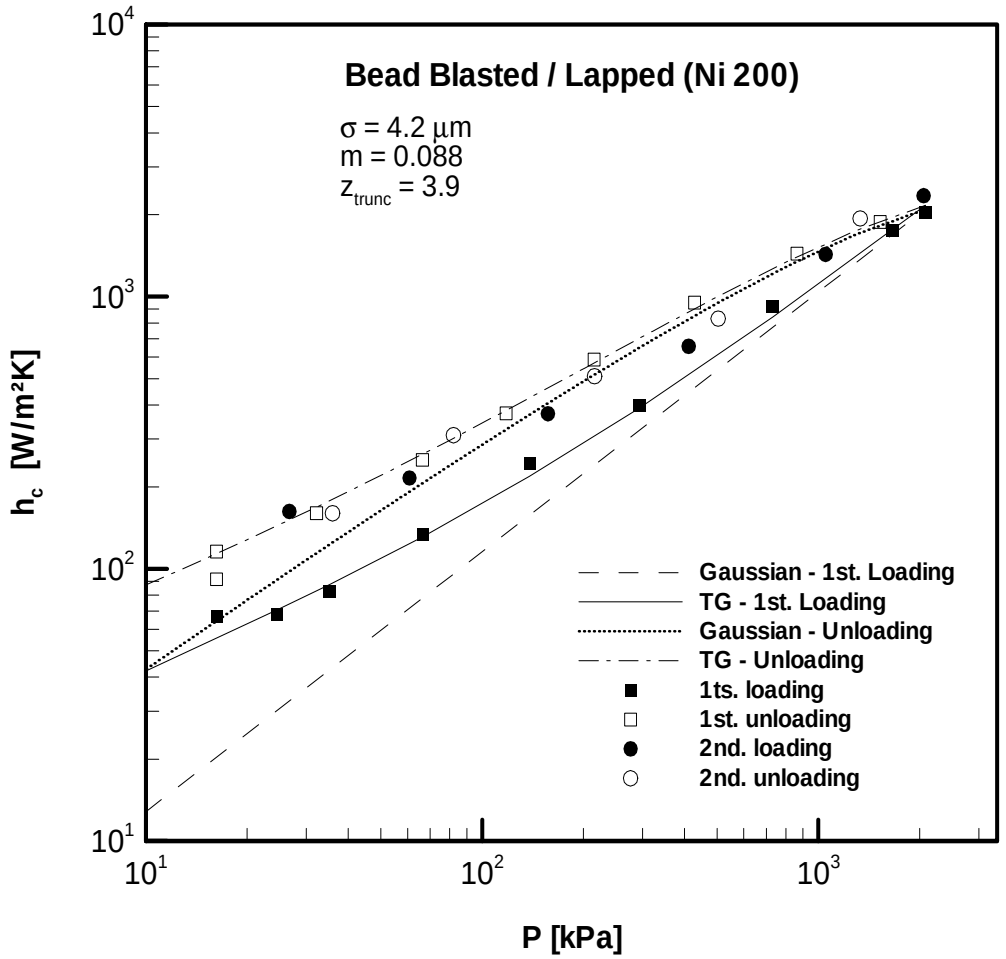

Figure 5.10 – Results from test N3

5.4. General conclusions from the SS 304 and Ni 200 tests

In general, the experimental results and comparison against the theoretical models showed the same behavior for all SS 304 and Ni 200 pairs tested. The hysteresis effect is evident during the first-loading/unloading cycle, indicating the appearance of plastic deformation of the contacting asperities during first loading. During the process first-unloading/re-loading/unloading, the hysteresis effect is negligible, indicating the appearance of elastic deformation.

The fully Gaussian first-loading model under predicted the data at low contact pressures, as already expected. The TG model with appropriate values of truncation level of the surface height distribution (z_{trunc}) predicted the first-loading data points very well. Table 5.3 shows the RMS differences between the measured and the predicted values of thermal contact conductance during first loading according to the fully Gaussian and the TG models. As one can see, the differences for the TG model are between 5.4 and 17.5 %, while the differences for the fully Gaussian model are between 21.1 and 48.4 %.

Table 5.3 – RMS differences between the first-loading data and the models

	RMS Difference [%]						
	Test	**S1**	**S2**	**S3**	**N1**	**N2**	**N3**
First-loading model	**Gaussian**	25.3	44.1	48.4	21.1	25.1	41.2
	TG	16.1	17.5	15.6	8.2	5.4	8.4

The values of z_{trunc} that promote the better fitting between the TG model and the first-loading data points decreases with the roughness level σ/m of the test pair. The values of z_{trunc} for Ni 200 are larger than the values for the SS 304 tests, indicating that the bead blasting process is able to generate high asperities more likely for Ni 200 than for SS 304, despite the latter has a slightly smaller bulk hardness (approximately 1500 MPa for SS 304 against 1700 MPa for Ni 200).

The unloading thermal contact conductance model proposed by Mikic (1972) was in good agreement only with test N3. In general, the model predicted the data well only for high contact pressures. The model may present a weakness in the fact that the Young's modulus, a very important mechanical parameter in elasticity problems, is not required as input

parameter. Mikic (1971) did include the Young's modulus in the analysis that leaded to the final expressions of the model. However, the Young's modulus turned out to be included into the dimensionless parameter Z (see Eqs. 2.35 and 2.39). According to the procedure described by the author, the parameter Z is computed using Eq. (2.29) in the fully Gaussian model or (Eq. 3.10) in the TG model, as already mentioned. It is not necessary to know the Young's modulus of the contacting bodies in advance in order to use the model. Since the deformation is purely elastic during unloading, it is reasonable to think that distinct metals possessing different Young's modulus would behave differently from each other during unloading. Since this is not the case of the unloading model proposed by Mikic (1971), it is believed the model has a weakness. Further studies are needed in this subject. Since the accuracy of this particular model is not the main objective of this work, this issue will now be put aside and attention will now be directed towards the truncation of surface height distribution problem.

5.5. Truncation levels of surface height distributions

The main problem is now to predict in advance the value of z_{trunc} without having to perform thermal contact conductance tests at various contact pressure levels and then find the z_{trunc} value that makes the theory best fit the data. Is it useful to know whether is possible to measure z_{trunc} using the commercially available surface roughness measurement systems (stylus profilometers). Milanez et al. (2002) presented a very detailed discussion about this issue and concluded that the stylus instruments with the actual roughness standards do not predict accurately z_{trunc}.

Figure 5.11 shows a graph of the values of z_{trunc} that best fit Hegazy's (1985) data as well as the data collected here, as a function of σ/m. The values of z_{trunc} were obtained by visual inspection of the curves that best fit the experimental data in Figs. 5.1 to 5.10 as already discussed. Different z_{trunc} are observed for distinct metals for the same σ/m, although in general z_{trunc} decreases with σ/m for SS 304, Ni 200 and Zr-4. Only the Zr-Nb alloy from Hegazy (1985) presented a constant value of z_{trunc}=3.5 for all roughness levels. The values of z_{trunc} are in general scattered between *3.5* and *4.5* for small σ/m. As σ/m increases, the scattering of z_{trunc} values tend to decrease.

The z_{trunc} values obtained from this experimental work are in general larger than the z_{trunc} values obtained from Hegazy's (1985) data for the same metal and same roughness level. Hegazy (1985) did not test contacts at pressures as low as those reached during this experimental program. The lowest contact pressures tested by Hegazy (1985) ranged from 400 to 500 kPa, while in this work, contact pressures as low as 15.8 kPa were tested. The

lower is the contact pressure, the easier is to detect the effect of truncation of surface height distributions on thermal contact conductance. Therefore, it is expected that the z_{trunc} values obtained from this experimental study are more accurate than the values obtained from Hegazy (1985).

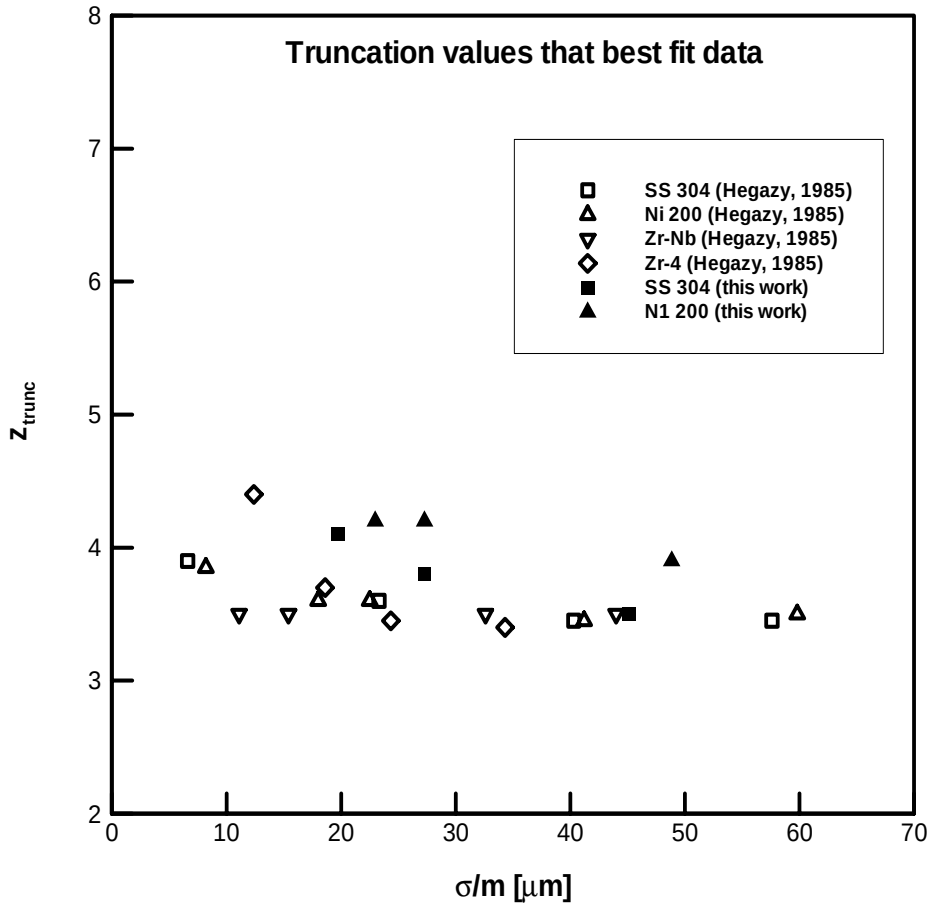

Figure 5.11 - z_{trunc} values that best fit the TG model to experimental data

It is necessary to know whether it is possible to predict z_{trunc} without having to conduct thermal contact conductance tests. Given the difficulty in modeling analytically the bead blasting process or any other machining process, it seems very difficult to predict z_{trunc} theoretically. Another option is to measure z_{trunc} using a profilometer, the same equipment used to measure σ and m. Most of the profilometers available commercially measure a roughness parameter that represents the height of the highest peak of the profile, generally known as R_p [μm]. Song (1988) used the R_p collected from a single profilometer trace as a measure for the truncation ($z_{trunc}=R_p/\sigma$). However, it looks very unlikely that a single trace is

able to pass through the peak of the highest asperity of the surface. On the other hand, if one decides to take several different profiles and one of the traces comes across an asperity much higher than the others, this single asperity could not represent the truncation level of the entire surface either, because one single asperity can not support the entire contact load alone, even a very light contact load.

5.6. Truncation levels of bead blasted surfaces

In an effort to better understand the truncation of real surface height distributions, it was decided to undertake a more detailed study of the surface generation process by bead blasting. Several bead blasting parameters, such as bead size, air pressure and exposure time can be adjusted in order to generate the desired roughness level.

The bead blasting study consisted of measuring the roughness parameters R_p (maximum profile height), σ (profile height RMS) and m (profile mean absolute slope) as well as the general trend of the asperity height distribution as a function of bead blasting exposure time between 1 and 16 minutes. Three different blasting pressures (10, 20 and 40 psi) and three different glass bead size ranges (125-180 μm, 279-420 μm and 590-840 μm) were used. Four profiles were assessed over each surface generated, resulting in a total of 136 profile measurements. Only flat lapped SS 304 (similar to the S1, S2 and S3 test samples) was used in the bead blasting study. The minimum and maximum σ/m ratios measured during the tests were 12 and 44 μm, respectively. The first important conclusion from this study was that the general trend of the surface height distribution was Gaussian independent of the blasting parameter combinations analyzed. The profile height RMS σ and the mean absolute slope m as well the ratio σ/m increase with increasing exposure time and blasting pressure, as expected, especially for the smaller glass beads. For the largest bead size range tested, the exposure time did not significantly affect σ and m. The blasting pressure was found to be the most important parameter in determining the roughness level.

The main goal of the bead blasting study was to analyze the truncation levels of the surface height distributions for every combination of blasting parameters. It was found that the measured R_p/σ (normalized maximum profile height) presented very different values for different profiles collected from the same surface. The largest measured R_p/σ difference between different profiles on the same surface was more than 100%. The variation between the R_p/σ values measured on a same surface was much larger than the variation between the mean values of R_p/σ collected from different surfaces. Also, the average of the four R_p/σ

readings on each surface varied randomly among different surfaces. In other words, the R_p/σ ratio seemed not to be controlled by any of the bead blasting parameters.

It was then decided to verify whether the measured R_p/σ values could be related only to the roughness level of the surface σ/m, as observed from the comparison between the TG model and the experimental data (Fig. 5.11), independently of the blasting parameters employed. Figure 5.12 shows a plot of all 136 measured R_p/σ values as a function of σ/m for all combinations of blasting parameters tested. The R_p/σ values lie in a large band, which seems to become narrower as σ/m increases. The mean value of R_p/σ also seems to experience a slight decrease with increasing σ/m. These observations are in accordance with the previous conclusion from Fig. 5.11. Rubert (1959) also conducted a similar work on surfaces prepared by turning, lapping and grinding and noticed that the ratio R_{max}/CLA (which is proportional to R_p/σ) decreases with CLA (which is proportional to σ). His work also shows a large scattering of data points, similarly to Fig. 5.12. At this point, it seems difficult to draw a conclusion of how to predict z_{trunc} from R_p/σ measurements. The scattering of R_p/σ values suggests that the point of truncation of the surface height distribution z_{trunc} is located in a region where the probability density function goes from the Gaussian model to zero. Figure 5.13 illustrates qualitatively this idea. The main task is to identify the exact location of z_{trunc} in the actual TG probability density function.

Due to the large scattering of points in Fig. 5.12, it is difficult to say which type of function (linear, logarithmic, power law, exponential, etc.) better predicts the decay of the mean R_p/σ with σ/m. Figure 5.14 shows curves obtained by fitting the data points of Fig. 5.12 using four different models and a comparison with the z_{trunc} values obtained from the SS 304 thermal tests. As one can see in Fig. 5.11, all the models used to fit the R_p/σ values of Fig. 5.12 as a function of σ/m lie bellow the z_{trunc} values obtained from thermal tests. This was expected, since a large number of asperities are higher than the mean value. Therefore, the mean R_p/σ is not in agreement with the z_{trunc} values collected from thermal tests. The largest R_p/σ values of Fig. 5.12 are larger than z_{trunc} values shown in Fig. 5.14, so the maximum measured R_p/σ values seem not to be an accurate estimation of z_{trunc} either. That was expected, since only one single asperity is not capable of supporting the entire contact load, even a very light one.

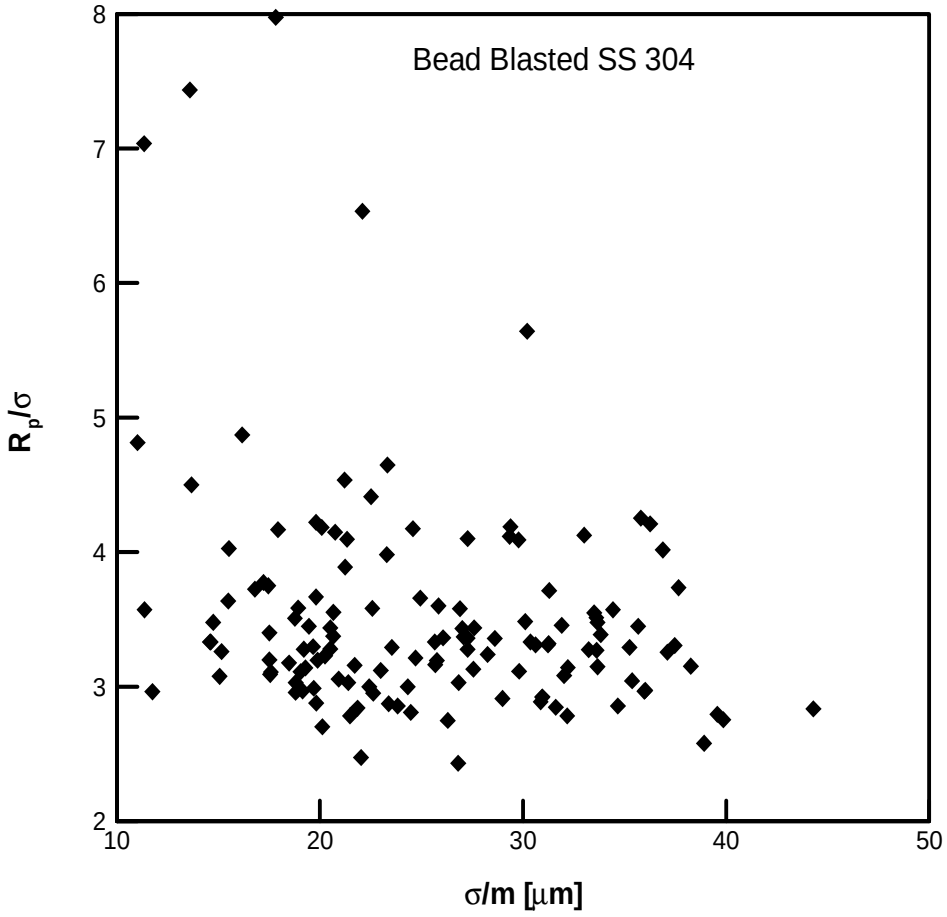

Figure 5.12 - R_p/σ versus σ/m for bead blasted SS 304 surfaces

The effective truncation level z_{trunc} seems to lie between the mean and the maximum R_p/σ values. In order to investigate where exactly z_{trunc} is located, Fig. 5.15 shows a comparison between z_{trunc} and a curve obtained by adding to the power law model (of Fig. 5.11) a vertical displacement of 0.6 times the standard deviation of the differences between all the 136 points of Fig. 5.12 and the power law model. In other words, the line shown in Fig. 5.15 represents the surface height level that contains all the asperities lower than the mean R_p/σ plus 0.6 times the standard deviation of R_p/σ. This curve is in very good agreement with the z_{trunc} values, which is an indication that the set formed by asperities higher than approximately 0.6 times the standard deviation above the mean of the highest peaks measured by the stylus profilometer seems to be capable of supporting the contact load.

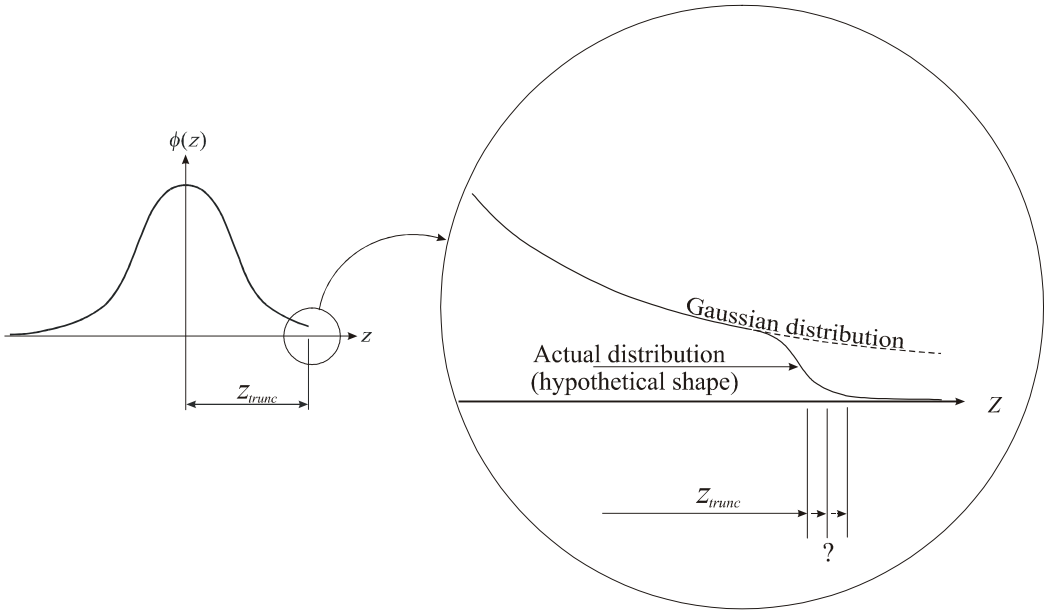

Figure 5.13 – Actual shape of the TG probability density function

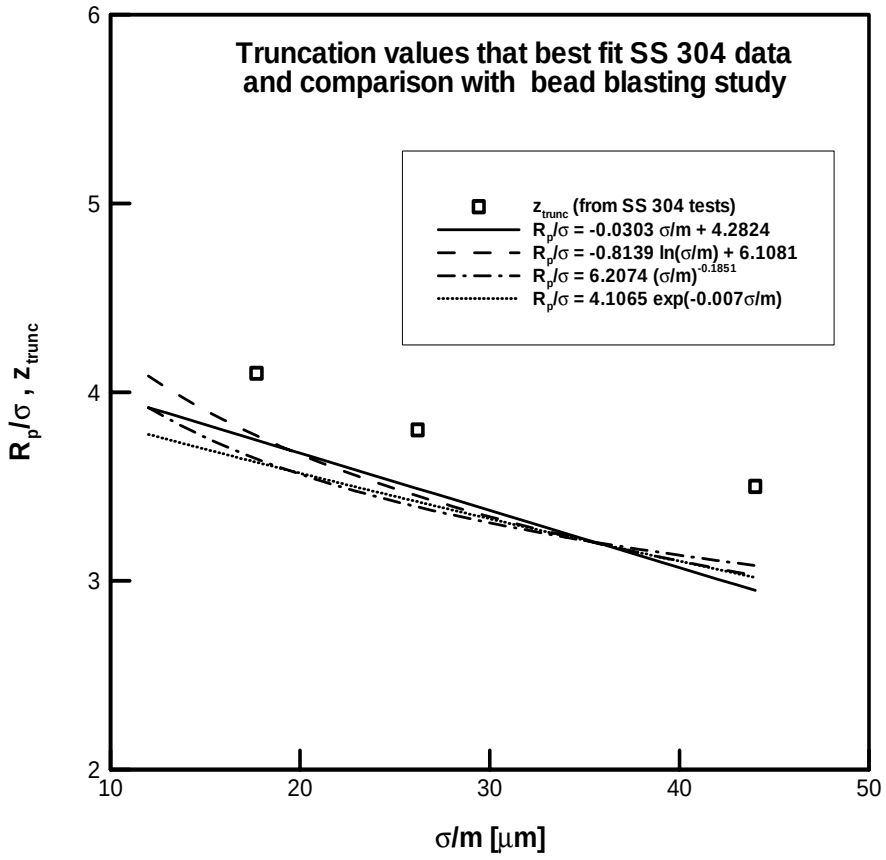

Figure 5.14 – Comparison between mean R_p/σ models and experimental z_{trunc} values versus σ/m for bead blasted SS 304 surfaces

It is also convenient to recall that the 136 points shown in Fig. 5.12 are not necessarily the 136 highest asperities measured in the bead blasting study. The highest asperity of one specific profile may not be as high as the second highest asperity of other profile. However, that second highest asperity is not taken into account by the stylus profilometer. The main reason for the inability of the stylus profilometer to detect relevant information on the truncation effect of surface asperity heights is because the standards used in surface profilometry were developed primarily for surface finish analysis. Similarly to the problem regarding to the cut off length discussed in the previous chapter, the actual standards lack surface roughness parameters relevant from a surface mechanics point of view. Furthermore, the truncation of surface heights distributions is a very recent finding and the actual roughness standards are not suitable to extract this type of information from surface profilometry.

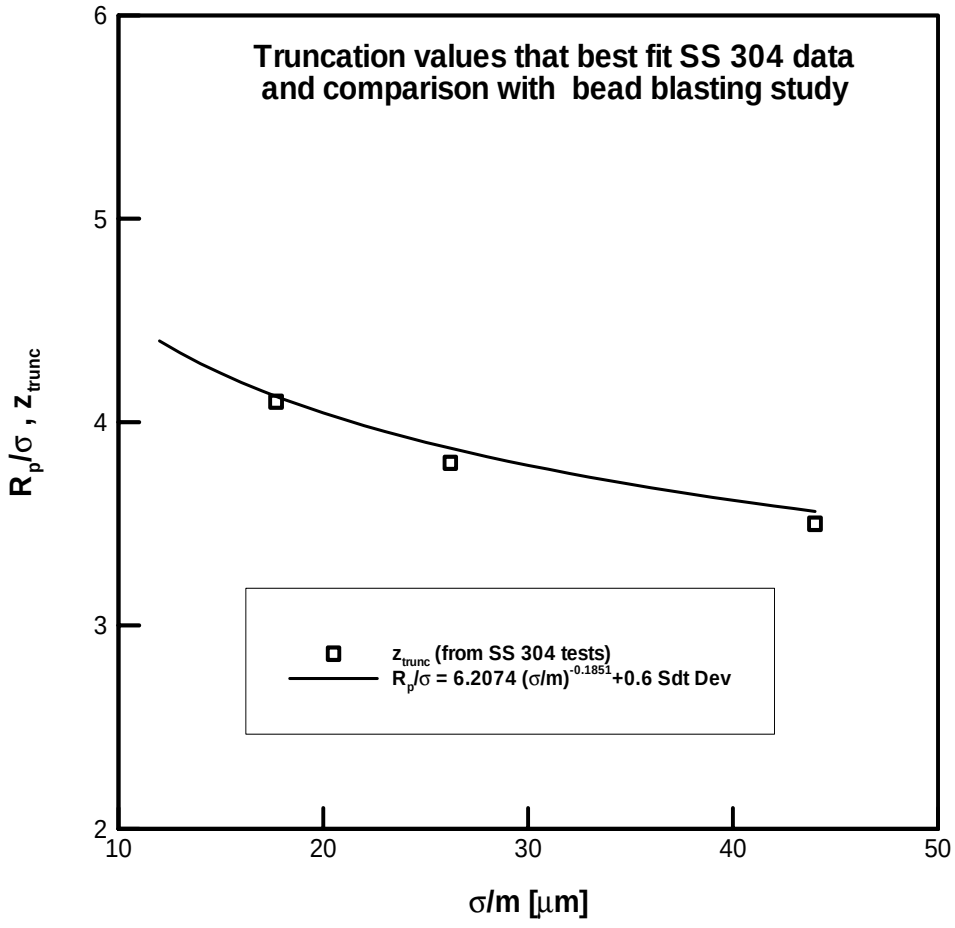

Figure 5.15 – Comparison between the power law model + 0.6 *StdDev* and experimental z_{trunc} values versus σ/m for bead blasted SS 304 surfaces

Given the complexity of the problem, a definite answer the question of how to predict z_{trunc} from ordinary roughness measurements still remains not completely given. As it can be seen from Figs. 5.1 through 5.10, the TG model is very sensitive to the value of z_{trunc}, and the measured R_p/σ present large variations over the same surface. The curve shown in Fig. 5.15 for R_p/m appears to be a reasonable estimate of z_{trunc} for the bead blasted SS 304 samples tested here. It is convenient to remember, although evident from the complexity of the problem described above, that the correlation shown in Fig. 5.15 is a priori not valid under conditions other than bead blasted SS 304. In order to validate this procedure as an accurate estimation of z_{trunc}, a much more extensive study must be undertaken in order to analyze other surface machining processes and other metals, which takes considerable time. For these reasons, carefully conducted thermal tests are believed to be a more straightforward way of extracting accurate information of z_{trunc}.

5.7. Difference between profile and surface statistics

Another cause that may contribute for the mean of the R_p/σ values (obtained by roughness measurements) to lie bellow the z_{trunc} values (obtained by fitting the TG model to the thermal contact conductance data sets S1, S2 and S3) is the inability of the stylus profilometer to pass through the peak of the asperities. Since the asperities are three-dimensional features and the dimensions of the stylus are very small (0.5 μm tip radius in the equipment used), the chances of the stylus trace to detect the asperity peak are very small. The profilometer trace is more likely to pass over the shoulder of the asperity rather than over the summit. Longuet-Higgins (1957), Nayak (1971) and McWaid (1990), among others, discuss extensively the differences between the statistics of a surface modeled as a random process and a profile taken from the surface. The theory defines “summits” as the highest points of the 3-D surface and “peaks” as the highest points of the 2-D profile taken from the surface. According to this theory, the probability density function of the peaks and the probability density function of the summits coincide only when the called surface bandwidth parameter α is infinity. The surface bandwidth parameter is defined as:

$$\alpha \equiv \frac{m_0 m_4}{m_2^2} \tag{5.1}$$

where m_0, m_2 and m_4 are defined according to Eqs. (2.11), (2.12) and (2.15), respectively. For a finite value of α, the probability density function of the summits is displaced to the right of the probability density function of the peaks, i. e., the surface summits are higher than the peaks of the profile. For α=1.5, the minimum possible value according to the theory, the

difference between the points of maxima of the peak and the summit probability density functions is approximately 0.74σ.

Roughly speaking, the summits of the surface are in general 0.74σ higher than the peaks of a profile arbitrarily collected on a surface with α=1.5, and the summits and the peaks have approximately the same height distribution for a surface with $\alpha \to \infty$. A typical value of the bandwidth parameter found in Mc Waid (1990) is α = 50. In this case, the points of maxima of the probability density functions of the summit and of the peaks are displaced by approximately 0.2σ. However, the precise quantification of α requires the knowledge of m_4 (see Eq. 5.1), which is not available in most stylus profilometers, including the equipment available for this experimental study. The most modern laser-based roughness measurement systems, as well as stylus profilometers adapted to modern data analysis software are able to measure m_4.

Further work is needed regarding to the surface characterization using commercially available roughness measurement systems. Both the inaccurate estimation of z_{trunc} from R_p/m measurements, and the difference between the profile and the surface statistics show that the commonly used profilometry is not sufficient to characterize the relevant features of the surface topography for applications in thermal contact conductance at low loads. The state of development of the theory on thermal contact conductance, especially now with the TG model, has pushed the envelope of the needs from surface profilometry. Surface features that were once considered negligible, such as the actual maximum level of surface heights, were found in this work to be very important at low contact pressures. This work opens a new branch of studies in the thermal contact conductance problem at low contact loads.

5.8. Summary

In this chapter, it was presented the experimental thermal contact conductance data for bead blasted/lapped SS 304 and Ni 200 at low contact loads and their comparisons with the new TG model and the existing fully Gaussian model. The TG model predicts the experimental data very well during first loading. The unloading data points lie generally above the existing theoretical models. The level of truncation of the bead blasted SS304 and Ni200 samples tested were found to be difficult to predict solely from ordinary profilometry. Further studies are needed in this regard. Thermal tests are believed to be the most accurate and straightforward method to obtain information regarding the actual truncation level of surface height distributions.

CHAPTER 6
SUMMARY AND CONCLUSIONS

6.1. Summary and conclusions

It has been extensively reported in the literature that thermal contact conductance present a strange behavior at low contact loads. The existing models systematically underpredict thermal contact conductance experimental data under these circumstances. This work presents new theoretical and experimental studies on thermal contact conductance at low contact pressures. An explanation for the odd behavior of thermal contact conductance at low contact pressures is proposed in the light of a new surface geometry model, the Truncated Gaussian-TG model. The higher asperities that constitute the surface topography are shorter than predicted by the existing theory and as a result, the theory overpredicts the mean separation gap at low contact pressures. As a consequence, thermal contact conductance experiments are underpredicted by the existing theory. The new geometry model is incorporated into the thermal contact conductance models based on the work of Cooper et al. (1969), available in the literature. Following a similar procedure as described by Song and Yovanovich (1988), a new plastic contact hardness model is also developed based on the new TG geometry model. Correlations are presented in order to facilitate the use of the new thermal contact conductance models.

The new thermal contact conductance models for conforming isotropic under plastic deformation are compared against experimental data collected by Hegazy (1985). The TG model predicts the trend of data points accurately over the entire range of contact pressures. At low contact pressures, the TG model predicts higher thermal contact conductances than the original fully Gaussian Model. The larger is the truncation of the Gaussian distribution (smaller z_{trunc}), the larger is the departure of the TG model from the fully Gaussian model. As the contact pressure increases, the TG model tends to the fully Gaussian model.

An experimental study was undertaken in order to measure thermal contact conductance between nominally flat bead blasted/lapped samples. Two metals, SS 304 and Ni 200 and three roughness levels for each metal were tested. Two consecutive loading/unloading cycles were performed in order to analyze also the hysteresis effect of thermal contact conductance on SS 304 and Ni 200. The experimental work included also thermal conductivity measurements, surface topography and surface micro-hardness

characterization of the test specimens in order to compare the thermal contact conductance data with the new TG model as well as with the fully Gaussian model.

In general, the experimental results from all the six tests were similar. The hysteresis effect appeared during the first loading/unloading cycle, indicating that the deformation of the asperities during the first loading of contact pressure was plastic. The data points from the second loading/unloading cycle lie approximately over the same curve as the first unloading data points, indicating that after the first loading, the deformation of the contacting asperities was predominantly elastic. The analysis of the hysteresis effect showed to be a very effective way of verifying the deformation mode experienced by the contacting asperities.

Similar to reported in other works of the literature, the existing thermal contact conductance model (fully Gaussian) underpredicted the first loading data points at low contact pressures. As the contact pressure was increased, the fully Gaussian model predicted the data well. The TG model, on the other hand, predicted the first loading experiments very well over the entire range of contact pressures provided an appropriate value of z_{trunc}, the truncation level of the surface height distribution, was input into the model. The unloading thermal contact conductance model proposed by Mikic (1972) predicted the unloading/re-loading data points well only for high contact pressures. At low contact pressures, the fully Gaussian unloading model predicted the experiments better than the TG unloading. However, the TG unloading model predicted the trend of data points better than the fully Gaussian model at low loads. Only the test that employed the roughest of the Ni 200 pairs was accurately predicted by the Mikic (1971) unloading model.

The comparisons between existing and new experimental data and the TG thermal contact conductance model showed that the cause for the strange behavior of thermal contact conductance at low contact pressures, extensively reported in other works in the literature, is the truncation of the highest asperities. Apart from the usual surface roughness parameters required by the theory, the RMS roughness σ and the mean absolute slope m, a third roughness parameter is required, which is the level of truncation of the surface height distribution z_{trunc}. This surface parameter was accurately obtained in this work from thermal contact conductance tests at various contact pressures (specially at contact pressure less than 500 kPa). The value of z_{trunc} that promoted the best comparison between theory and experiments was considered to be an estimation of the truncation level of the surface asperity height distribution. The universally used stylus profilometer proved not to be sufficiently accurate to detect the truncation level of the surface height distribution because very large

variations were found between the normalized heights of the highest asperities R_p/σ of different profiles measured in a same surface.

The most straightforward and accurate way of extracting information on z_{trunc} is from thermal tests. First-loading thermal contact conductance is measured at several contact pressures levels. Then, the z_{trunc} value that makes the TG model better fit to the thermal data is chosen. In this work, three roughness levels and two distinct metals and one surface preparation method was tested. Truncation levels for surfaces possessing these features are assessed and presented here. In order to obtain a more complete z_{trunc} data bank, more thermal contact conductance experiments are needed, employing other metals, other surface machining processes as well as a broader range of surface roughness.

6.2. Contributions of this work

The present work presented a new relevant aspect of surface topography and its consequence in thermal contact conductance, which is the truncation of surface height distribution. The truncation makes the existing theory underpredict thermal contact conductance at low contact pressures. This observation had been reported but not explained by several researchers in the literature and the new theory fills this gap. A new analytical thermal contact conductance model was derived, and the new model showed to be accurate in predicting existing and new experimental data.

Apart from the finding of the truncation effect on thermal contact conductance, other contributions to the field were made in this work. Through the study of the hysteresis effect of thermal contact conductance, it was shown that the contact between bead blasted/lapped Ni 200 and SS 304 is plastic during the first loading and predominantly elastic during the subsequent unloading/re-loading. This work also presented the more extensive comparative study already done between unloading thermal contact conductance data and the only analytical model available in the literature, which is the Mikic (1971) model.

6.3. Suggestions for future works

A broad range of studies in thermal contact conductance was opened with the findings that real surfaces present truncated height distributions. As already mentioned in the last section and in the discussion of the results in the previous chapter, there are many possibilities of improvement of the study initiated here. The suggestions for future works in this subject are:

- Collect more thermal contact conductance data using other materials, other surface machining processes and a broader range of surface roughness in order to gather more information on the truncation level of height distributions z_{trunc} of real surfaces.
- Perform a more detailed study regarding the maximum profile height R_p/σ involving different metals, machining processes and roughness levels in order to establish a connection between z_{trunc} and R_p/σ obtained from stylus profilometry or other type of roughness measurement.
- Analyze the reasons why the Mikic (1971) unloading model did not predict experiments accurately and propose modifications to the model as well as develop correlations to facilitate the use of the model. The modeling of thermal contact conductance during unloading is a very complex problem and the Mikic (1971) model was the only analytical model found in the literature.

A few considerations can also be made now regarding to the application of this study to the bi-metallic heat switch under development at the NCTS/LABSOLAR, which was the motivation for this work. Milanez and Mantelli (2000 and 2001) used the first-loading model assuming fully Gaussian distribution of surface heights to predict the thermal resistance of the heat switch. These authors showed that this model underpredicts the conductance of the heat switch in part of the range of contact pressures tested. As clearly shown in the present study, the fully Gaussian first-loading model is not adequate to predict thermal contact conductance during unloading; the model underpredicts the experiments. The Mikic (1971) unloading model was shown here to predict better the experiments. Although at very low contact pressures the Mikic (1971) model is not accurate either, this unloading model would be better than the first-loading fully Gaussian model to predict the thermal resistance of the heat switch. However, the main problem detected in this study regarding to the measurements presented by Milanez and Mantelli (2001) is the time spent to achieve steady state. According to these authors, the heat switch achieved steady state after 2 hours each new pressure level was set. In the present study, a much more accurate experimental set-up was employed to measure thermal contact conductance than the one used by Milanez and Mantelli (2001) and it was noticed that steady state could take up to 10 hours to be achieved under the lightest load tested. Therefore, new measurements with larger periods of time are needed to achieve steady state in order to measure more accurately the thermal resistance of the heat switch. The experience gained during the experimental study described here would be very useful in the manufacturing and testing of a new prototype of the heat switch.

REFERENCES

Abbot, E. J. and Firestone, F. A., "Specifying Surface Quality," *Mechanical Engineering*, Vol. 55, pp. 596-572, September, 1933.

Antonetti, V. W, "On the Use of Metallic Coatings to Enhance Thermal Contact Conductance," Ph. D. Thesis, Department of Mechanical Engineering, University of Waterloo, Waterloo, Ontario, Canada, 1983.

Antonetti, V. W. and Yovanovich, M. M., "Using Metallic Coatings to Enhance Thermal Contact Conductance of Electronic Packages," *Heat Transfer Engineering*, Vol. 9, No. 3, pp. 85-92, 1988.

Arpaci, V. S., *Conduction Heat Transfer*, Addison-Wesley Publishing Company, 1966.

Bowden, F. P. and Tabor, D., *The Friction and Lubrication of Solids*, Oxford, Vol. 1, 1964.

Clausing, A. M. and Chao, B. T., "Thermal Contact Resistance in a Vacuum Environment," *Journal of Heat Transfer*, pp. 243-251, May 1965.

Cooper, M. G., Mikic, B. B. and Yovanovich, M. M., "Thermal Contact Conductance," *Journal of Heat Mass Transfer*, Vol.12, pp. 279-300, 1969.

De Vaal, J. W., "Thermal Joint Conductance of Surfaces Prepared by Grinding," Ph. D. Thesis, Department of Mechanical Engineering, University of Waterloo, Waterloo, Ontario, Canada, 1988.

Fletcher, L. S., Lambert, M. A., and Marotta, E. E., "Thermal Enhancement Coatings for Microelectronic Systems," *Journal of Electronic Packaging*, Vol. 120, pp. 229-237, September 1998.

Frank, D. J. and Nast, T. C., "Getter-Activated Cryogenic Thermal Switch", *Proceedings on Cryogenic Engineering Conference Cambridge*, pp. 933-940, 1985.

Greenwood, J. A., and Williamson, J. B. P., "Contact of Nominally Flat Surfaces," *Proceedings of the Royal Society of London*, 1966.

Hegazy. A. A., "Thermal Joint Conductance of Conforming Rough Surfaces: Effect of Surface Micro-hardness Variation," Ph. D. Thesis, Department of Mechanical Engineering, University of Waterloo, Ontario, Canada, 1985.

Holman, J. P., *Experimental Methods for Engineers*, 6th Edition, McGraw-Hill, Singapore, pp. 49-103, 1994.

Johnson, K. L., *Contact Mechanics*, Cambridge University Press, Cambridge, 1985.

Kimura, Y., "Estimation of the Number and the Mean Area of Real Contact Points on the Basis of Surface Profiles," *Wear*, Vol. 15, pp. 47-55, 1970.

Lambert, M. A. and Fletcher, L. S., "Design Graphs for Contact Conductance of Metals," *32nd Thermohphysics Conference, AIAA 97-2462*, 1997a.

Lambert, M. A. and Fletcher, L. S., "Review of Models for Thermal Contact Conductance of Metals," *Journal of Thermophysics and Heat Transfer*, Vol. 11, No. 2, pp. 129-140, April-June 1997b.

Lambert, M. A. and Fletcher, L. S., "Thermal Contact Conductance of Spherical Rough Metals," *Journal of Heat Transfer*, Vol. 119, pp. 684-690, November 1997c.

Lankford, K. "Heat Switches," *Spacecraft Thermal Control Handbook, Vol. I: Fundamental Technologies*, Chapter 10, Second Edition, the Aerospace Press, El Segundo, CA, pp. 353-371, 2002.

Longuet-Higgins, M. S., "The Statistical Analysis of a Random, Moving Surface," *Philosophical Transactions of the Royal Society*, Series A, Vol. 249, pp.321-387, 1957.

Mantelli, M. B. H., and Yovanovich, M. M., "Thermal Contact Resistance," *Spacecraft Thermal Control Handbook, Vol. I: Fundamental Technologies*, Chapter 16, Second Edition, the Aerospace Press, El Segundo, CA, pp. 599-638, 2002.

Marotta, E. E. and Fletcher, L. S., "Thermal Contact Conductance for Aluminum and Stainless Steel Contacts", *7th AIAA/ASME Joint Thermophysics and Heat Transfer Conference-Albuquerque NM*, AIAA 98-2758, 1998.

Marotta, E. E. and Fletcher, L. S., "Thermal Contact Conductance of Refractory Ceramic Coatings," *Journal of Thermophysics and Heat Transfer*, Vol. 10, No. 1, January-March 1996.

Maddren, J. and Marschall, E., "Predicting Thermal Contact Resistance at Cryogenic Temperatures for Spacecraft Applications", *AIAA 28th Thermophysics Conference*, Orlando, Florida, 1993.

McGee, G. R., Schankula, M. H. and Yovanovich, M. M., "Thermal Resistance of Cylinder-Flat Contacts: Theoretical Analysis and Experimental Verification of a Line-Contact Model," *Nuclear Engineering and Design*, Vol. 86, pp. 369-381, 1985.

Mc Waid, T. H., "Thermal Contact Resistance Across Pressed Metal Contact in a Vacuum Environment", Ph. D. Thesis, University of California, Santa Barbara, United States, 1990.

Mikic, B. B., "Analytical Studies of Contact of Nominally Flat Surfaces: Effect of Previous Loading," *Journal of Lubrication Technology*, pp. 451-456, October 1971.

Mikic, B. B., "Thermal Contact Conductance; Theoretical Considerations," *Journal of Heat Mass Transfer*, Vol. 17, pp. 205-214, Pergamon Press, 1974.

Milanez, F. H., Yovanovich, M. M. and Culham, J. R., "Effect of Surface Asperity Truncation on Thermal Contact Conductance," *VIII Itherm*, May 29 - June 1, San Diego, CA, 2002.

Milanez, F. H. and Mantelli, M. B. H., "A New Passive Heat Switch Conception For Space Applications", *33TH National Heat Transfer Conference*, Albuquerque, NM, 1999.

Milanez, F. H. and Mantelli, M. B. H., "Thermal Modeling of a Heat Switch Considering Threaded Contact Conductances ", *34th Thermophysics Conference*, Denver, CO, June, 2000.

Milanez, F. H. and Mantelli, M. B. H., " Recent Studies of a Bi-Metallic Heat Switch for Space Applications ", *35th Thermophysics Conference*, Anaheim, CA, June, 2001.

Naes, L. and Nast, T., "A Self Actuated Thermal Switch for Operation with Redundant Mechanical Refrigerators", *Proceedings on Cryogenic Engineering Conference Cambridge*, pp. 925-932, 1985.

Nast, T., Bell, G. and Barnes, C., "Development of Gas Gap Cryogenic Thermal Switch", *Advances in Cryogenic Engineering* Vol. 27, Plenum Press, New York, pp. 1117-1124, 1982.

Nayak, P. R., "Random Process Model of Rough Surfaces," Journal of Lubrication Technology, Transactions of the ASME, pp. 398-407, July, 1971.

Nho, K. M., "Experimental Investigation of Heat Flow Rate and Directional Effect on Contact Conductance of Anisotropic Ground/Lapped Interfaces," Ph. D. Thesis, Department of Mechanical Engineering, University of Waterloo, Waterloo, Ontario, Canada, 1990.

O'Callaghan, P. W. and Probert, S. D., "Real Area of Contact Between a Rough Surface and a Softer Optically Flat Surface," *Journal of Mechanical Engineering Science*, Vol. 12, No. 4, pp. 259-267, 1970.

Powell, "Thermal Conductivity of Elements," *Journal of Physical and Chemical Reference Data*, Vol. 1, No.2, pp. 355, 1972.

Rubert, M. P. "Confusion in measuring Surface Roughness," *Engineering*, October 23, pp. 393-395, 1959.

Sayles, R. S and Thomas, T. R., "A Stochastic Explanation of Some Structural Properties of a Ground Surface," *International Journal of Production Research*, Vol. 14, pp. 641-655, 1976.

Savija, I., Culham, J. R., Yovanovich, M. M. and Marotta, E. E., "Review of Thermal Conductance Models of Joints Incorporating Enhancement Materials," *40th AIAA Aerospace Sciences Meeting and Exhibit*, Reno, Nevada, USA, paper No. AIAA 2002-0494, 2002a.

Savija, I., Yovanovich, M. M., Culham, J. R. and Marotta, E. E., "Thermal Joint Resistance Models for Conforming Rough Surfaces with Grease Filled Interstitial Gaps," *40th AIAA Aerospace Sciences Meeting and Exhibit*, Reno, Nevada, USA, paper No. AIAA 2002-0495, 2002b.

Song, S. "Analytical and Experimental Study of Heat Transfer through Gas Layers of Contact Interfaces," Ph. D. Thesis, Department of Mechanical Engineering, University of Waterloo, Waterloo, Ontario, Canada, 1988.

Song, S. and Yovanovich, M. M., "Relative Contact Pressure: Dependence on Surface Roughness and Vickers Microhardness," *Journal of Thermophysics and Heat Transfer*, Vol.2, No. 4, pp. 633-640, 1988.

Song, S., Yovanovich, M. M. and Goodman, F. O., "Thermal Gap Conductance of Conforming Surfaces in Contact," *Journal of Heat Transfer*, Vol. 115, pp. 533-540, August 1993.

Song, S., Yovanovich, M. M. and Nho, K. M., "Thermal Gap Conductance: Effects of Gas Pressure and Mechanical Load," *Journal of Thermophysics and Heat Transfer*, pp. 62-68, January-March 1992.

Sridhar, M. R., 1994, "Elastoplastic Contact Models for Sphere-Flat and Conforming Rough Surface Applications", Ph. D. Thesis, University of Waterloo, Ontario, Canada, 1994.

Sridhar, M. R. and Yovanovich, M. M., "Review of Elastic and Plastic Contact Conductance Models: Comparison with Experiment," *Journal of Thermophysics and Heat Transfer*, Vol. 8, No. 4, pp. 633-640, 1994.

Sridhar, M. R. and Yovanovich, M. M., "Thermal Contact Conductance of Tool Steel and Comparison with Model," *International Journal of Heat and Mass Transfer*, Vol. 39, No. 4, pp. 831-839, 1996.

Thomas, T. R., *Rough Surfaces*, Longman Ltd., London and New York, 1982.

Van Oost, S., Bekaert, G., Bhatti, R. S., Scull, S. and Jewell, C., "A Heat Switch for Space Cryocooler Aplications", *Proceedings of the 4th European Symposium on Space Enviromental and Control Systems*, pp. 209-216, 1991.

Yovanovich, M. M., "Thermal Contact Correlations", *Spacecraft Radiative Heat Transfer and Temperature Control*, Edited by T. E. Horton, Progress in Astronautics and Aeronautics, Vol.83, NY, 1981.

Yovanovich, M. M. *Thermal Contact Conductance: Theory and Applications*, Thermal Contact Conductance course notes, Department of Mechanical Engineering, University of Waterloo, Waterloo, Ontario, Canada, 1984.

Yovanovich, M. M., De Vaal, J. W., Hegazy, A. H., "A Statistical Model to Predict Thermal Gap Conductance Between Conforming Rough Surfaces" AIAA Paper No. 82-0888, June 1982.

Yovanovich, M. M., *Advanced Differential Equations and Special Functions*, Course Notes, Department of Mechanical Engineering, University of Waterloo, Waterloo, Ontario, Canada, Spring 2001.

Williamson, J. B. P., Pullen, J. and Hunt, R. T., "The Shape of Solid Surfaces," *Surface Mechanics*, Ed. By F. F. Ling, ASME, New York, pp.24-35, 1969.

APPENDIX 1

MICRO-HARDNESS AND SURFACE ROUGHNESS DATA

Micro-hardness data

Table A1.1 – SS 304 micro-hardness test diagonal lengths

	Diagonal length [μm]									
Load [g]	indentation 1		indentation 2		indentation 3		indentation 4		indentation 5	
300	47.1	47.3	48.8	49.2	48.3	47.1	47.6	47.6	49.5	50.0
200	36.5	39.1	38.1	39.1	35.7	36.7	36.7	38.6	38.4	38.9
100	25.3	24.9	24.4	24.1	24.4	24.4	24.9	24.4	24.6	24.9
50	15.4	16.4	16.2	15.2	15.0	15.9	15.0	15.4	16.2	15.7
25	10.1	10.4	10.9	10.6	10.1	10.9	10.9	9.9	10.9	10.4
10	6.3	6.3	5.8	6.3	5.8	6.0	6.3	6.0	5.8	6.0

Table A1.2 – SS 304 micro-hardness data

Load [g]	Mean diagonal [μm]	Mean hardness [MPa]
300	48.2	2532.8
200	37.8	2754.4
100	24.6	3238.8
50	15.6	4025.5
25	10.5	4452.4
10	6.0	5400.6

Table A1.3 – Ni 200 micro-hardness test diagonal lengths

	Diagonal length [μm]									
Load [g]	indentation 1		indentation 2		indentation 3		indentation 4		indentation 5	
300	42.7	43.7	42.5	43.0	42.5	42.0	42.7	42.7	43.5	42.0
200	34.3	34.8	34.3	34.8	35.7	35.5	35.2	35.2	34.3	34.0
100	24.4	24.4	24.6	24.1	23.4	23.4	24.1	23.7	24.1	23.7
50	16.9	17.1	17.4	16.4	17.4	17.6	16.9	17.4	16.4	16.7
25	11.3	10.9	11.6	11.6	11.8	11.3	11.8	11.3	11.3	11.8
10	7.2	7.0	7.2	7.0	7.7	7.7	7.5	7.2	7.2	7.7

Table A1.4 – Ni 200 micro-hardness data

Load [g]	**Mean diagonal [μm]**	**Mean hardness [MPa]**
300	42.7	3229.5
200	34.8	3243.6
100	24.0	3409.5
50	17.0	3395.7
25	11.5	3713.2
10	7.4	3629.3

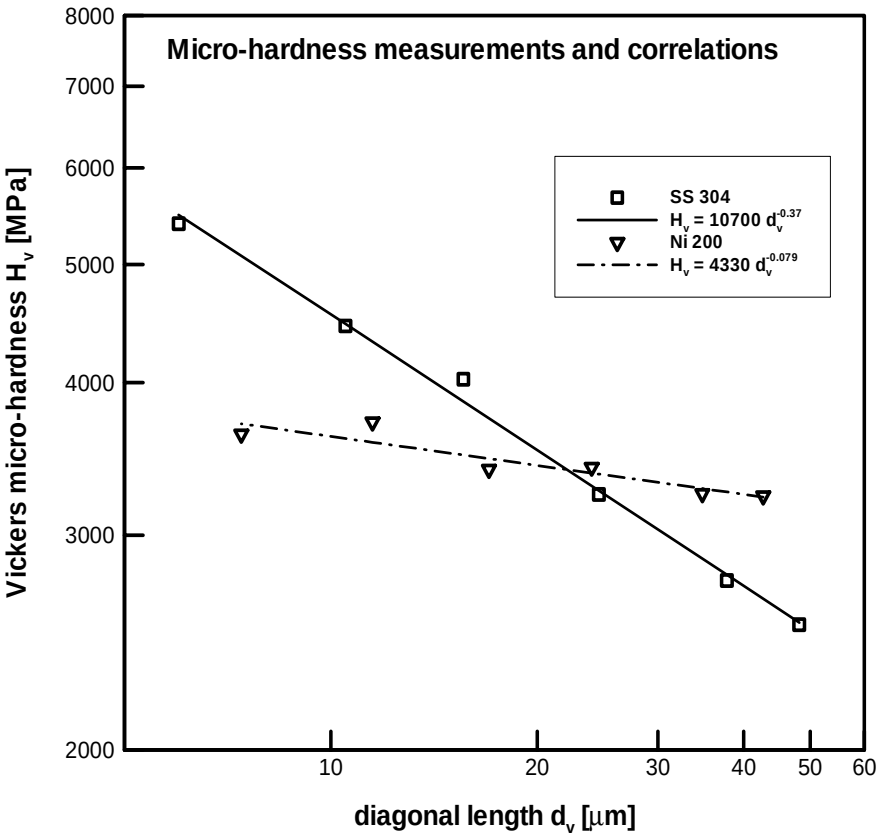

Figure A1.1 – Measured Vickers micro-hardness versus diagonal length

Roughness data

Table A1.5 – SS 304 and Ni 200 roughness data

	test	S1	S2	S3	N1	N2	N3
Bead blasted	σ [μm]	0.74	1.49	3.91	1.84	2.99	4.01
		0.66	1.23	3.91	2.01	2.97	4.49
		0.67	1.13	3.86	1.62	3.05	4.41
		0.76	1.35	4.09	1.66	2.96	3.93
		0.66	1.25	3.79	1.59	2.99	4.22
	Average σ [μm]	0.70	1.29	3.91	1.74	3.0	4.21
	m	0.037	0.051	0.096	0.067	0.116	0.083
		0.035	0.044	0.101	0.076	0.106	0.088
		0.030	0.045	0.096	0.069	0.112	0.091
		0.037	0.045	0.097	0.077	0.105	0.082
		0.035	0.051	0.099	0.080	0.108	0.085
	Average *m*	0.035	0.047	0.098	0.074	0.110	0.086
Lapped	σ [μm]	0.13 / 0.12 / 0.12 / 0.11 / 0.10 / 0.12			0.09 / 0.11 / 0.09 / 0.09 / 0.11 / 0.09		
	Average σ [μm]	0.12			0.10		
	m	0.021 / 0.020 / 0.020 / 0.022 / 0.021 / 0.026			0.016 / 0.016 / 0.017 / 0.017 / 0.018 / 0.016		
	Average *m*	0.022			0.017		
Average combined σ/m [μm]		17.7	26.2	40.0	23.0	27.0	48.0

APPENDIX 2
EXPERIMENTAL UNCERTAINTY ANALYSIS

The uncertainty in the final result which is the combination of several independent measurements is computed through the methodology described by Holman (1994). Let M be the measurement result that is a function of n measured variables x_1, x_2, x_3,.., x_n, i. e.:

$$M = M(x_1, x_2, x_3, ..., x_n) \tag{A2.1}$$

Now let w_R be the uncertainty in the result and w_1, w_2, w_3,…, w_n be the uncertainties in x_1, x_2, x_3,.., x_n, respectively. The uncertainty in the result is given as:

$$w_M = \left[\left(\frac{\partial M}{\partial x_1} w_1 \right)^2 + \left(\frac{\partial M}{\partial x_2} w_2 \right)^2 + ... + \left(\frac{\partial M}{\partial x_n} w_n \right)^2 \right]^{1/2} \tag{A2.2}$$

Thermocouple calibration. According to the manufacturer, the uncertainty of thermocouples in the range of temperatures of interest is ±0.6°C. However, for thermal contact conductance measurement purposes, the exact temperature level is not as important as the temperature gradients. Both for heat flux and temperature drop measurements (Eq. 4.4), accurate measurements of temperature differences are the most important. The temperature level is required only to estimate the thermal conductivity (Eqs. 4.1 to 4.3). Therefore it is convenient to calibrate only the temperature differences measured by the thermocouples. In order to do that, the thermocouples were submerged into a thermal bath, which was constantly agitated to homogenize its temperature. The maximum difference between the temperature readings of all the 18 thermocouples was found to be less than 0.1°C. Therefore, the uncertainty of temperature difference readings was assumed to be ±0.1°C in this work.

Temperature drop measurement uncertainty. Based on the discussion above, the uncertainty in temperature drop measurement, which is the difference of the two extrapolated temperatures is expected to be ±0.1°C. Since the temperature drop at the interface varied from 40°C (lightest load) to 8°C (highest load), the uncertainty of temperature drop measurement varied from ±0.25% (lightest load) to ±1.25% (highest load).

Thermal conductivity estimation uncertainty. Sample thermal conductivity is measured as:

$$k_{sample} = \frac{q_{sample}}{-(dT/dx)_{sample}} \tag{A2.3}$$

The heat flux crossing the sample is the average of the heat fluxes crossing the two ARMCO Iron flux-meters, i. e.:

$$q_{sample} = \frac{q_{ARMCO,1} + q_{ARMCO,2}}{2} \tag{A2.4}$$

The heat flux crossing the ARMCO Iron flux-meter is compute as:

$$q_{ARMCO} = -k_{ARMCO} \cdot \left(\frac{dT}{dx} \right)_{ARMCO} \tag{A2.5}$$

The uncertainty of the tabulated values of conductivity of ARMCO Iron is ±2%, according to the reference consulted (Powell, 1972). The maximum difference between the correlation for the conductivity of ARMCO Iron (Eq. 4.1) and the tabulated values is ±1%. The total uncertainty of the ARMCO Iron conductivity is estimated here as the sum of these two uncertainties, that is, $\pm 3\,\%$.

The uncertainty in the temperature profile slope measurements is estimated as the ratio between the uncertainty of temperature difference (±0.1°C) and the distance between the first and the last thermocouple (25mm), i. e., ±0.004°C/mm. The minimum flux-meter slope measurement was 0.08°C/mm and the uncertainty in slope measurement is the ratio between these two values, that is, ±5%. Combining the uncertainty of slope measurement with the uncertainty of the ARMCO conductivity, by means of Eqs. (A2.2) and (A2.5), one obtains the total uncertainty of heat flux measurement of each ARMCO Iron as ±5.8%. The uncertainty of measurement of the heat flux crossing the sample is obtained by means of Eqs. (A2.2) and (A2.4) and the result is ±4.1%. The uncertainty of temperature slope measurement of the SS 304 sample is ±1.25% and of the Ni 200 sample is ±5.5%. With these values and Eqs. (A2.2) and (A2.3), the total uncertainty of conductivity measurement is ±4.3% for SS 304 and ±6.9% for Ni 200. The conductivity values were then correlated (Eqs. 4.2 and 4.3) and the maximum difference between the correlation of SS 304 and the measured values is ±1.5%, and the maximum difference between the correlation of Ni 200 and the measured values is ±1.2%. The total uncertainty of conductivity estimation using the correlations is then ±5.8% for SS 304 and ±8.1 % for Ni 200.

The uncertainty of the thermal conductivity estimation due to uncertainty in the specimen mean temperature (±0.6°C, according to the thermocouple manufacturer) is obtained by means of Eqs. (4.1) to (4.3) and (A2.2) and the results are 0.06%, 0.1% and 0.09% for the ARMCO, Ni 200 and SS 304, respectively. These uncertainties are so small in comparison to the total uncertainties that they are neglected here. Therefore, the final

uncertainties of the conductivities estimated from Eqs. (4.2) and (4.3) are ±5.8% for SS 304 and ±8.1% for Ni 200, respectively.

Thermal contact conductance measurement uncertainty. Thermal contact conductance is computed as:

$$h_c = \frac{q}{\Delta T} \tag{A2.6}$$

The heat flux crossing the interface q is the average of the heat fluxes crossing the two test specimens q_{upper} and q_{lower}, that is:

$$q = \frac{q_{upper} + q_{lower}}{2} \tag{A2.7}$$

The heat fluxes crossing the upper and lower contacting specimens are computed as:

$$q_{specimen} = -k_{specimen} \cdot \left(\frac{dT}{dx} \right)_{specimen} \tag{A2.8}$$

The uncertainty of specimen temperature slope measurement dT/dx is ±20% for the lowest load and ±0.4% for the highest load. Combining these uncertainties with the uncertainty of thermal conductivity according to Eqs. (A2.2), (A2.7) and (A2.8), the uncertainty of heat flux measurement is ±14.7% for the lowest load and ±4.1% for the highest load for SS 304. For Ni 200, the uncertainty of heat flux measurement is ±15.3% for the lowest load and ±5.7% for the highest load. As already mentioned, the uncertainty of the temperature drop across the interface is expected to be ±0.25% at the lowest load and ±1.25% at the highest load. With these results and by means of Eqs. (A2.2), (A2.6) and (A2.7), one gets the total uncertainty of thermal contact conductance measurement for SS 304 as approximately ±15% at the lowest load and ±4% at the highest load. For the Ni 200, the uncertainty is approximately 15% at the lowest load and 6% at the highest load.

Contact load measurement uncertainty. The load cell was calibrated in the range of interest by means of dead weights in the light load range (0 to 175 N) and a calibrated compression test machine in the high load range (340 to 1350 N). A total of 80 compression load values were taken during both loading and unloading. The hysteresis effect was not detected in the load cell. The 80 load readings were then correlated to the respective load cell out put signal. The maximum difference between the correlation and the actual load readings was only 1%. This value is adopted here as the uncertainty of contact load measurement.

APPENDIX 3
THERMAL CONTACT CONDUCNTACE EXPERIMENTAL DATA

SS 304 thermal contact conductance experimental data

Table A3.1 – S1 test data

	P [kPa]	h_c [W/m^2·K]	T_m [°C]	k [W/m·K]	ΔT [°C]	q [W/m^2]
first loading	15.8	17.5	52.1	19.1	72.3	1267.8
	15.8	14.0	23.4	18.4	20.7	289.4
	46.6	33.8	40.5	18.8	47.8	1613.8
	87.1	68.0	35.6	18.7	34.2	2324.6
	183.5	122.9	32.0	18.6	23.9	2935.7
	368.0	218.3	29.0	18.5	15.7	3418.7
	743.7	382.3	31.2	18.6	12.7	4865.0
	1211.2	580.6	29.7	18.5	8.7	5063.7
	1991.6	1144.3	31.3	18.6	5.5	6340.7
	2092.4	1398.1	49.3	19.1	9.1	12771.2
	2456.4	1608.1	48.7	19.1	7.9	12781.5
	2767.8	1962.2	64.9	19.5	9.7	19013.0
first unloading	2300.8	1898.6	64.7	19.5	10.0	18924.7
	1954.1	1581.4	48.8	19.1	8.1	12809.3
	1083.6	852.1	44.2	18.9	12.0	10193.2
	557.5	489.4	30.5	18.5	10.4	5083.8
	294.2	320.5	24.4	18.4	9.1	2921.8
	145.1	172.6	22.9	18.3	11.2	1938.3
	60.6	79.9	25.1	18.4	18.1	1443.8
	35.0	48.2	28.1	18.5	25.2	1212.7
	15.8	31.6	30.5	18.5	31.3	987.6
	15.8	36.5	36.0	18.7	39.8	1454.4
	15.8	44.4	44.4	18.9	52.1	2312.2

Table A3.1 – S1 test data (cont.)

	P [kPa]	h_c [W/m^2·K]	T_m [°C]	k [W/m·K]	ΔT [°C]	q [W/m^2]
second loading	31.9	65.7	39.3	18.8	40.1	2631.8
	100.0	120.8	34.6	18.7	27.3	3292.4
	318.2	266.0	31.1	18.6	15.8	4206.8
	981.0	604.2	27.6	18.5	7.5	4501.3
	1954.6	1380.7	25.7	18.4	3.3	4602.1
	2811.9	1981.5	53.7	19.2	6.5	12840.3
second unloading	1109.4	897.1	46.9	19.0	12.5	11213.1
	368.8	422.4	30.4	18.5	11.5	4837.9
	75.6	145.4	28.6	18.5	18.5	2691.9
	15.8	74.6	34.0	18.6	31.1	2321.1

Table A3.2 – S2 test data

	P [kPa]	h_c [W/m^2·K]	T_m [°C]	k [W/m·K]	ΔT [°C]	q [W/m^2]
first loading	15.8	26.4	59.5	19.4	79.7	2099.7
	15.8	26.5	62.4	19.4	84.8	2249.4
	15.8	23.8	22.6	18.3	17.3	411.9
	37.7	32.4	56.6	19.3	67.7	2192.1
	61.1	41.0	54.5	19.2	58.6	2403.2
	116.8	62.0	51.0	19.1	48.9	3030.2
	232.6	110.7	44.2	18.9	36.9	4079.9
	458.4	213.1	38.8	18.8	23.0	4894.2
	934.2	398.8	49.6	19.1	22.4	8936.4
	1851.4	734.8	54.0	19.2	16.3	11978.7
	2719.7	999.4	57.8	19.3	14.2	14215.2
first unloading	2064.2	899.4	59.3	19.3	15.7	14110.8
	999.0	614.8	57.2	19.3	19.4	11909.3
	490.4	401.8	47.7	19.0	20.6	8272.0
	467.8	372.7	34.9	18.7	13.6	5052.5
	257.3	209.3	31.2	18.6	15.7	3293.7
	115.8	105.6	29.3	18.5	17.6	1856.0
	58.5	62.2	25.4	18.4	16.2	1010.2
	36.9	48.4	26.1	18.4	18.9	915.4
	15.8	33.5	27.5	18.5	23.8	796.4
	15.8	26.3	61.4	19.4	81.8	2148.2
	15.8	30.8	28.8	18.5	25.8	795.5

Table A3.2 – S2 test data (cont.)

	P [kPa]	h_c [W/m^2·K]	T_m [°C]	k [W/m·K]	ΔT [°C]	q [W/m^2]
second loading	60.8	63.9	34.8	18.7	29.0	1855.7
	172.4	125.2	34.1	18.6	22.5	2823.0
	180.6	135.9	40.0	18.8	28.2	3827.6
	472.0	356.4	34.9	18.7	13.9	4963.7
	1250.0	670.7	34.1	18.6	8.6	5785.5
	2727.9	1032.7	35.7	18.7	6.8	7000.2
second unloading	1002.8	630.8	32.5	18.6	8.1	5114.2
	329.4	290.9	27.1	18.5	9.7	2813.2
	84.8	93.9	28.2	18.5	16.8	1573.3
	15.8	39.7	32.9	18.6	30.6	1217.4
	15.8	31.6	20.6	18.3	11.6	365.4

Table A3.3 – S3 test data

	P [kPa]	h_c [W/m^2·K]	T_m [°C]	k [W/m·K]	ΔT [°C]	q [W/m^2]
first loading	15.8	14.9	38.8	18.8	18.6	277.7
	15.8	19.7	54.2	19.2	76.6	1509.5
	15.8	18.6	35.6	18.7	43.5	810.7
	43.8	29.8	34.4	18.7	39.4	1173.6
	99.5	52.3	31.2	18.6	30.9	1615.3
	211.7	86.6	29.2	18.5	24.3	2103.6
	399.1	137.3	27.1	18.5	18.2	2498.6
	826.0	266.7	23.9	18.4	10.5	2787.2
	1781.2	489.6	28.8	18.5	9.8	4801.8
	3454.3	826.0	34.4	18.7	8.8	7231.2
first unloading	1555.4	570.8	30.4	18.5	9.6	5481.5
	823.8	390.7	23.3	18.3	7.9	3084.0
	355.1	208.5	21.8	18.3	9.9	2062.0
	216.3	143.5	21.3	18.3	11.2	1607.6
	140.8	106.4	20.7	18.3	11.8	1250.6
	49.4	59.4	19.9	18.3	12.8	762.1
	15.8	29.5	19.0	18.2	12.9	380.1
	15.8	31.4	31.5	18.6	34.0	1066.4

Table A3.3 – S3 test data (cont.)

	P [kPa]	h_c [W/m^2·K]	T_m [°C]	k [W/m·K]	ΔT [°C]	q [W/m^2]
second loading	60.8	63.9	34.8	18.7	29.0	1855.7
	172.4	125.2	34.1	18.6	22.5	2823.0
	180.6	135.9	40.0	18.8	28.2	3827.6
	472.0	356.4	34.9	18.7	13.9	4963.7
	1250.0	670.7	34.1	18.6	8.6	5785.5
	2727.9	1032.7	35.7	18.7	6.8	7000.2
second unloading	1002.8	630.8	32.5	18.6	8.1	5114.2
	329.4	290.9	27.1	18.5	9.7	2813.2
	84.8	93.9	28.2	18.5	16.8	1573.3
	15.8	39.7	32.9	18.6	30.6	1217.4
	15.8	31.6	20.6	18.3	11.6	365.4

Ni 200 thermal contact conductance experimental data

Table A3.4 – N1 test data

	P [kPa]	h_c [W/m^2·K]	T_m [°C]	k [W/m·K]	ΔT [°C]	q [W/m^2]
first loading	16.2	69.7	21.4	86.3	17.6	1230.1
	29.1	101.8	19.0	86.7	16.8	1706.8
	58.7	169.8	20.7	86.4	15.2	2575.7
	118.0	270.9	19.3	86.7	14.9	4027.3
	241.2	523.6	15.9	87.3	12.8	6702.1
	469.7	971.8	18.1	86.9	12.5	12125.8
	903.3	1883.6	19.4	86.6	11.4	21406.8
	1968.6	3713.6	20.5	86.4	9.6	35500.1
first unloading	1404.9	3398.2	19.6	86.6	8.1	27682.4
	1025.3	2649.1	20.6	86.4	9.1	24204.3
	695.6	2115.5	19.4	86.7	8.7	18360.1
	411.9	1426.2	17.8	86.9	10.4	14831.3
	287.6	1026.7	19.8	86.6	10.9	11241.6
	194.7	701.2	20.9	86.4	10.7	7525.0
	120.0	442.1	20.9	86.4	11.5	5079.1
	52.1	252.3	22.7	86.0	15.4	3884.2
	36.8	183.1	21.9	86.2	15.1	2757.4
	16.2	75.5	23.7	85.8	20.4	1540.0
	16.2	79.3	30.6	84.6	17.7	1403.6
	16.2	76.1	22.7	86.0	20.8	1586.7

Table A3.4 – N1 test data (cont.)

	P [kPa]	h_c [W/m^2·K]	T_m [°C]	k [W/m·K]	ΔT [°C]	q [W/m^2]
second loading	24.4	102.2	21.4	86.3	17.4	1775.9
	46.1	191.3	19.8	86.6	13.1	2501.1
	124.8	462.1	20.4	86.5	11.0	5091.3
	313.7	1133.2	23.9	85.8	10.0	11282.1
	720.4	2179.2	31.6	84.4	12.0	26047.8
	977.7	2565.8	32.5	84.2	11.7	30054.8
	1995.3	3943.1	33.1	84.1	9.0	35376.8
second unloading	1006.5	2842.4	28.6	85.0	9.7	27494.8
	572.5	2017.8	24.2	85.8	10.2	20655.9
	212.2	865.9	20.1	86.5	13.8	11929.0
	71.1	336.8	15.8	87.3	14.5	4891.7
	16.2	77.2	19.8	86.6	17.2	1324.5

Table A3.5 – N2 test data

	P [kPa]	h_c [W/m^2·K]	T_m [°C]	k [W/m·K]	ΔT [°C]	q [W/m^2]
first loading	16.2	62.7	24.9	85.6	19.4	1213.9
	26.9	92.6	24.3	85.7	17.9	1659.3
	48.1	129.2	21.0	86.3	13.7	1770.9
	120.2	253.9	20.8	86.4	16.2	4122.2
	206.6	418.1	23.0	86.0	17.0	7106.3
	429.2	888.3	21.4	86.3	13.2	11692.0
	826.8	1588.7	19.5	86.6	10.5	16614.7
	1762.6	3201.4	23.7	85.9	9.7	30913.7
first unloading	1363.8	2871.5	22.9	86.0	9.5	27271.1
	633.9	1746.3	19.8	86.6	11.7	20517.8
	306.3	1004.7	19.4	86.6	13.7	13735.8
	160.9	563.3	20.3	86.5	15.0	8446.3
	87.7	323.3	21.6	86.2	17.1	5534.3
	41.4	188.6	21.4	86.3	17.1	3228.7
	16.2	89.9	21.9	86.2	17.1	1534.8

Table A3.5 – N2 test data (cont.)

	P [kPa]	h_c [W/m^2·K]	T_m [°C]	k [W/m·K]	ΔT [°C]	q [W/m^2]
second loading	28.5	111.8	20.7	86.4	18.7	2084.6
	48.6	194.7	19.0	86.7	16.0	3110.1
	48.2	180.0	19.0	86.7	14.6	2634.7
	118.9	358.0	18.9	86.7	14.7	5253.2
	313.5	931.1	19.5	86.6	12.4	11532.0
	851.8	1972.0	21.9	86.2	10.2	20156.3
	1474.2	3023.4	29.5	84.8	9.6	28942.6
	1778.9	3284.2	28.9	84.9	12.6	41217.1
second unloading	1203.0	2680.7	22.9	86.0	11.6	31197.0
	630.7	1758.2	18.2	86.9	11.1	19493.4
	215.0	746.2	17.4	87.0	11.0	8210.1
	67.8	281.0	16.2	87.2	12.2	3428.9
	16.2	94.9	22.0	86.2	15.6	1476.5

Table A3.6 – N3 test data

	P [kPa]	h_c [W/m^2·K]	T_m [°C]	k [W/m·K]	ΔT [°C]	q [W/m^2]
first loading	16.2	66.6	17.4	87.0	12.7	843.3
	24.5	67.8	17.9	86.9	15.6	1060.1
	35.2	82.6	18.9	86.7	17.1	1415.0
	66.6	133.7	19.1	86.7	16.5	2205.8
	138.2	243.4	17.8	86.9	12.7	3093.8
	294.3	400.1	18.3	86.8	11.8	4721.1
	731.7	919.9	21.0	86.3	10.7	9885.6
	1657.8	1744.8	20.8	86.4	10.4	18201.0
	2080.9	2036.1	22.2	86.1	10.1	20572.1
first unloading	1527.9	1882.3	20.3	86.5	9.0	16894.5
	863.2	1439.1	19.7	86.6	9.5	13729.0
	428.0	950.6	21.9	86.2	11.1	10539.7
	215.2	587.7	21.1	86.3	13.0	7628.1
	117.8	372.4	20.8	86.4	15.0	5596.4
	66.5	251.3	19.9	86.6	15.4	3882.3
	32.2	160.0	21.2	86.3	18.5	2959.0
	16.2	115.8	19.2	86.7	15.4	1784.0
	16.2	91.6	19.0	86.7	12.2	1120.5

Table A3.6 – N3 test data (cont.)

	P [kPa]	h_c [W/m^2·K]	T_m [°C]	k [W/m·K]	ΔT [°C]	q [W/m^2]
second loading	26.7	162.6	19.8	86.6	9.5	1545.1
	60.8	215.8	21.2	86.3	11.0	2370.8
	156.8	371.4	20.1	86.5	14.7	5449.9
	411.1	657.1	23.9	85.8	12.4	8139.3
	1049.9	1429.9	23.7	85.8	10.2	14615.9
	2054.4	2349.4	21.8	86.2	9.6	22490.3
second unloading	1331.3	1937.8	20.9	86.4	11.6	22550.7
	503.3	830.4	17.4	87.0	11.1	9206.8
	215.8	510.2	19.3	86.7	11.0	5613.9
	82.2	309.6	20.6	86.4	12.2	3778.5
	35.9	160.0	20.3	86.5	15.6	2489.6